

ABSTRACT

Title of dissertation: ADVANTAGEOUS UTILIZATION
 OF NONLINEAR PHENOMENA IN
 MICRO-STRUCTURES AND
 MACRO-STRUCTURES

Andrew James Dick, Doctor of Philosophy, 2007

Dissertation directed by: Professor Balakumar Balachandran
 and Professor C. Daniel Mote, Jr.
 Department of Mechanical Engineering

Within this work, the nonlinear oscillations of various beam-like structures are studied. Methods are developed to analyze systems of this type to better understand their behavior in order to utilize the nonlinear phenomena associated with them and to provide insights for device development. The specific applications explored within this study are piezoelectric micro-scale resonators, micro-resonator arrays, the cantilever probes of atomic force microscopes, and a macro-scale test apparatus for the AFM probe. In order to analytically, numerically, and experimentally study these systems, various methods are employed. Analytical models are developed, utilizing bending stiffness and axial stretching terms to explain nonlinear behavior.

Reduced-order-modeling techniques are applied to develop single-mode and multi-mode approximations and study the dynamic behavior of these structures. Nonlinear analysis methods are used to study these systems and to determine approximate solutions. Discrete models are developed and utilized to conduct numerical simulations. Data collected through experimental observations are utilized to determine system parameters and verify simulation results.

Through this work, a multi-variable, parametric identification scheme is developed for characterizing nonlinear oscillators from frequency-response data with jumps in the amplitude values. Parameter values are identified for piezoelectric micro-scale resonators and good agreement is seen with the corresponding model predictions. By using multiple data sets, parameter trends are studied for changes in the input signal. In another nonlinear analysis, a relationship is identified between a nonlinear localization phenomena called Intrinsic Localized Modes (ILMs) and nonlinear vibration modes. A method is developed to derive equations for determining the spatial characteristics of the localizations and the profiles are used to conduct further studies. For a cantilever beam impactor system, a period doubling phenomenon is identified for off-resonance excitation conditions. Changes in this system's response are studied and a method is proposed to utilize this phenomenon to determine conditions for grazing. This work shows how important nonlinearities are in beam structures when oscillations exceed the linear range. More importantly, these studies show how an understanding of the nonlinearities can be used to the advantage of the system.

ADVANTAGEOUS UTILIZATION OF
NONLINEAR PHENOMENA IN
MICRO-STRUCTURES AND MACRO-STRUCTURES:
APPLICATIONS TO MICRO-RESONATORS
AND ATOMIC FORCE MICROSCOPY

by

Andrew James Dick

Dissertation submitted to the Faculty of the Graduate School of the
University of Maryland, College Park in partial fulfillment
of the requirements for the degree of
Doctor of Philosophy
2007

Advisory Committee:

Professor Balakumar Balachandran, Chair/Advisor
Professor Inderjit Chopra, Dean's Representative
Professor Donald L. DeVoe
Professor C. Daniel Mote, Jr., Co-Advisor
Professor Santiago Solares

© Copyright by
Andrew James Dick
2007

ACKNOWLEDGEMENTS

I would like to thank everyone who has helped to make this research and dissertation possible. I would especially like to thank my parents and family for their constant support of my education. I would also like to thank Professor Balachandran and Professor Mote for all of their guidance throughout my graduate education and for helping me get to where I am today. I would like to thank the members of the research group, those of both the immediate group and the extended group, for all of their help and for helping to providing such an ideal environment for learning.

Support for the research discussed in this dissertation through NSF EAPSI Grant No. 0611611, AFOSR Grant No. F49620-03-10181, DARPA Grant No. F3060202C0016, and ARO Grant No. W911NF0510076 is gratefully acknowledged. I am also grateful for the support provided by a Litton Industries Fellowship from Fall 2004 to Spring 2005 and the support of an Ann G. Wylie Dissertation Fellowship from the Graduate School during the Fall of 2006.

TABLE OF CONTENTS

List of Tables	vii
List of Figures	viii
1 Introduction	1
1.1 Parametric Identification	2
1.2 Intrinsic Localized Modes	14
1.3 Cantilever Beam Impactor System	22
1.4 Scope and Organization of Dissertation	26
2 Parametric Identification	28
2.1 Resonator Model	29
2.2 Identification Scheme	35
2.2.1 Stages of identification	37
2.2.2 Parameters for PZT and AlGaAs micro-resonators	40

2.3	Trends of Identified Parameters	45
2.3.1	Modal force and piezoelectric coefficient	46
2.3.2	Axial force, linear stiffness, and nonlinear stiffness	48
2.4	Summary	51
3	Intrinsic Localized Modes	53
3.1	Analysis of Oscillator Array	54
3.1.1	Intrinsic Localized Mode Profiles	54
3.1.2	Nonlinear Vibration Mode Analyses	59
3.1.3	Floquet Theory	71
3.2	Analysis Results	71
3.2.1	Method of Multiple Scales Approach	72
3.2.2	Restricted Normal Mode Approach	73
3.2.3	Invariant-Manifold Approaches	74
3.3	Effects of Internal Resonance	79
3.3.1	One-to-One Internal Resonance	79
3.3.2	Three-to-One Internal Resonance	81
3.3.3	Results	91
3.4	Summary	95
4	Cantilever Beam Impactor System	97
4.1	System Modeling	98
4.1.1	Macro-Scale Experimental Setup	98

4.1.2	Model Development	99
4.1.3	Numerical Simulations	103
4.1.4	Micro-Scale System	110
4.2	Analysis	111
4.2.1	Excitation Near ω_1	112
4.2.2	Excitation Near $2.5 \times \omega_1$	114
4.2.3	Floquet Theory	117
4.2.4	Grazing Bifurcation	117
4.3	Micro-Scale System	119
4.4	Summary	124
5	Conclusions and Future Work	126
5.1	Parametric Identification	127
5.2	Intrinsic Localized Modes	128
5.2.1	Internal Resonance	130
5.3	Cantilever Beam Impactor System	131
A	Analytical Methods	134
A.1	Method of Multiple Scales Approach	134
A.2	Restricted Normal Mode Approach	138
A.3	Real-Variable Invariant-Manifold Approach	139
A.4	Modified Invariant-Manifold Approach	141

B Galerkin Method Equations	143
Bibliography	145

LIST OF TABLES

1.1	Representative PZT resonator dimensions.	10
1.2	Representative AlGaAs resonator dimensions.	12
1.3	Microcantilever array parameters.	17
1.4	Important dimensions of experimental test apparatus.	24
2.1	Comparison of parameter values for PZT resonator.	43
2.2	Comparison of parameter values for AlGaAs resonator.	44
3.1	Amplitude ratio r_1 from simulation and analyses.	72
3.2	Amplitude ratio r_2 from simulation and analyses.	73
3.3	Parameter values for three-to-one internal resonance condition.	82
3.4	Amplitude ratios.	87
3.5	Amplitude ratios for three-to-one internal resonance conditions.	93
4.1	Linear and nonlinear damping factors.	106

LIST OF FIGURES

1.1	Parameters from the method developed by Ayela and Fournier.	6
1.2	Structure of piezoelectric, micro-scale clamped-clamped resonator. . .	9
1.3	PZT resonator and geometry.	10
1.4	Structure of AlGaAs micro-resonator.	11
1.5	Experimental arrangement showing how a laser vibrometer is positioned to examine transverse vibrations of the resonator. The resonator is excited by signals input to the drive electrode.	13
1.6	Experimental frequency-response data obtained for a 200 μm PZT resonator. The asterisks ‘*’ correspond to forward sweep data and the ‘o’ correspond to backward sweep data.	13
1.7	Studying ILMs in MEMS arrays: (a) unit cell of micro-cantilever array and (b) representative simulation results of localization in a micro-scale cantilever array. Time is shown on the horizontal axis and the oscillator position is shown on the vertical axis.	16
1.8	Excitation frequency profile for uniform excitation within numerical simulation.	18

1.9	Diagram of experimental test apparatus.	23
1.10	Diagram of different behavior within an impact system. Curves <i>A</i> , <i>B</i> , and <i>C</i> represent unconstrained, grazing, and constrained conditions, respectively.	24
2.1	Diagram of PZT resonator identifying spatial coordinate and three sections.	29
2.2	Thick lines are used to show the analytically predicted frequency-response curve, and the stable and unstable response segments are shown by solid lines and dashed lines, respectively. The thin lines are the critical-point curves, which are independent of the excitation level. The encircled intersections of these lines represent the critical points of the frequency-response curves.	34
2.3	The effects of increasing parameter values on the analytical response curve. The curve depicted by using solid lines corresponds to the nominal case, and the curve illustrated by using dashed lines corresponds to the effect of increasing the following: (a) equivalent viscous damping coefficient, (b) nonlinear stiffness coefficient, (c) linear stiffness coefficient, and (d) modal force parameter.	36
2.4	Flow chart depicting an overview of the parametric identification scheme that is used to study piezoelectric micro-scale resonators. . . .	38
2.5	Nonlinear model fit to micro-resonator data: (a) 200 micrometer PZT resonator and (b) 200 micrometer AlGaAs resonator.	42

2.6	Approximating a linear force-voltage relation. The circles ‘o’ represent modal force values for different data sets and the solid line is a linear curve fit to these data points.	47
2.7	Trends of the first, linear natural frequency for different PZT micro-resonators. Diamonds correspond to 100 μm resonators, squares correspond to 200 μm resonators, and circles correspond to 400 μm resonators. Identified parameter values are presented in (a) and model prediction values are presented in (b) showing how the model is capable of explaining the parameter trends.	50
2.8	Trends of the nonlinear stiffness coefficient for different PZT micro-resonators. Identified parameter values are presented in (a) and model parameter values are presented in (b) showing qualitative agreement.	51
3.1	Spatial characteristics of an ILM: (a) example of a displacement profile and (b) the averaged normalized amplitude profile around localization. The horizontal axis lists the position of the oscillators relative to the center of the localization. The average normalized profile is represented by filled circles. The average plus and minus one standard deviation is represented by empty circles and empty diamonds, respectively.	55

3.2	Results of analytical studies: (a) a comparison of simulation profile (solid line) and the profile obtained by using the method of multiple scales (dashed line) and (b) the four roots of the polynomial from restricted normal mode approach.	65
3.3	Results of analytical studies: (a) a comparison of simulated profile (solid line) and analytical profile from restricted normal mode approach (dashed line) and (b) a comparison of simulated profile (solid line) and analytical profile from modified real-variable invariant-manifold approach (dashed line).	67
3.4	Localization simulations: (a) failure to create an ILM with amplitude ratios from the restricted normal mode approach and (b) the successful creation of an ILM with amplitude ratios from the modified real-variable invariant-manifold approach.	75
3.5	Nonlinear vibration modes: (a) the nonlinear vibration modes relating motion of x_0 and $x_{\pm 1}$ for the range of motion experienced during an ILM and (b) the nonlinear vibration modes relating motion of $x_{\pm 1}$ and $x_{\pm 2}$ for the range of motion experienced during an ILM. The nonlinear vibration modes are represented by the solid curves and the dashed line corresponds to only the linear term. The units are in micrometers.	78
3.6	Dispersion curves for mono-element (dashed) and di-element (solid) arrays. The horizontal axis corresponds to the wave number and the vertical axis corresponds to the frequency.	81

3.7	Dispersion curve for di-element array with three-to-one internal resonance.	83
3.8	ILM simulation results for a di-element array with three-to-one internal resonance.	84
3.9	Comparison of the ILM profile for the original parameter values (solid) with the profile for three-to-one internal resonance conditions (dashed).	86
3.10	Four roots of the polynomial of the Restricted Normal Mode Approach. The roots are plotted as a function of the parameter R with the different styles: dash, dot-dash, and dot-dot-dash. The fourth root to the polynomial, which is represented by the solid curve, is shown in the insert.	89
3.11	Comparison of results from the Restricted Normal Mode Approach (dashed) with simulation results (solid).	90
3.12	Comparison of results from linearized Invariant-Manifold Approach (dashed) with simulation results (solid).	91
4.1	Phase portraits of the system's response to harmonic excitation near the fundamental frequency: (a) the response measured experimentally and (b) the simulated response.	108
4.2	Phase portraits of the system's response to harmonic excitation near two and a half times the fundamental frequency: (a) the response measured experimentally and (b) the simulated response.	109

4.3	(a) Diagram of atomic force microscope system and (b) SEM image of AFM cantilever probe.	111
4.4	Plots of the system response for excitation near the fundamental frequency: (a) the system's response for unconstrained conditions and (b) the system's response for constrained conditions.	113
4.5	Frequency spectrum plots of the system response for excitation near the fundamental frequency: (a) the system's response for unconstrained conditions and (b) the system's response for constrained conditions.	114
4.6	Plots of the system response for excitation near two and a half times the fundamental frequency: (a) the system's response for unconstrained conditions and (b) the system's response for constrained conditions.	115
4.7	Frequency spectrum plots of the system response for excitation near two and a half times the fundamental frequency: (a) the system's response for unconstrained conditions and (b) the system's response for constrained conditions.	116
4.8	A bifurcation diagram for harmonic excitation near the fundamental frequency. The separation distance between the beam's center of oscillation and the surface of the contact material is used as the control parameter.	118

4.9	A phase portrait of the system's unconstrained response to harmonic excitation near the fundamental frequency. The enlarged section of the plot shows the Poincaré section which reveals the quasi-periodic nature of the response.	119
4.10	A bifurcation diagram for harmonic excitation near two and a half times the fundamental frequency. The separation distance between the beam's center of oscillation and the surface of the contact material is used as the control parameter.	120
4.11	A phase portrait of the system's unconstrained response to harmonic excitation near two and a half times the fundamental frequency. The Poincaré section reveals the quasi-periodic nature of the response. . .	120
4.12	Phase portraits of data collected from commercial AFM system for an excitation frequency of two and a half times the fundamental frequency: (a) the unconstrained response and (b) - (d) the response of system under constrained conditions as the separation distance is incrementally decreased.	121
4.13	Frequency spectrum plots of data collected from commercial AFM system for an excitation frequency of two and a half times the fundamental frequency: (a) the system's unconstrained response and (b) - (d) the response of system under constrained conditions as the separation distance is incrementally decreased.	122

4.14	A bifurcation diagram of the data collected from the commercial AFM system for an excitation frequency of two and a half times the fundamental frequency. Period-doubling is shown to occur at the grazing bifurcation.	124
A.1	System of Interest: Amplitude Relations Determined By Numerically Solving for p	140

Chapter 1

Introduction

Nonlinear oscillations of beam and beam-like structures are considered in this work. The nonlinear behavior results from relatively large oscillations that exceed the range within which linear models are sufficient. This type of behavior can occur in both macro-scale and micro-scale structures. In order to study the systems examined within this work, nonlinear beam models are developed to explain the nonlinear behavior with nonlinear bending stiffness terms, nonlinear axial stretching terms, and nonlinear inertia terms. To study these spatially continuous systems, it is necessary to utilize reduced-order-models such as those with a finite number of vibration modes. After model development, an assortment of nonlinear analyses is employed to study the system behavior and stability as well as to derive approximate solutions. The discretized models are then used to numerically simulate the behavior

of the system so that additional studies can be conducted. Data from experimental observations are used to obtain values for the system parameters and to verify the results of the simulations.

1.1 Parametric Identification

Piezoelectric micro-scale resonators and resonator arrays are currently being developed through a number of different efforts. These devices are manufactured by using microelectromechanical system (MEMS) fabrication techniques with the goal of replacing the bulky macro-scale resonators currently in use. With micro-scale dimensions, they require only a fraction of the space, and in addition, the power requirements are low compared to those of their macro-scale counterparts. A number of different resonator devices of various geometries are currently being developed. A few of these include clamped-clamped resonators [1, 2], Film Bulk Acoustic Wave Resonators (FBARs) [3], Silicon Bulk Acoustic Resonators (SiBAR) [4], ring-shaped contour-mode resonators [5], Lamé-mode resonators [6], I^2 resonators [7], paddle oscillators [8], and various disk resonators [9, 10, 11]. These devices have a number of different applications including accelerometers [12], detection of minuscule quantities of materials including biological substances [13, 14, 15, 16], and communications and signal processing [17, 18, 19].

During their development, the presence of nonlinear behavior has been observed in many of these devices [20, 21, 22, 23, 24]. As seen with many micro-scale devices, the dissipative forces are very small. Due to this diminished level of damp-

ing, micro-scale devices can exhibit nonlinear behavior that equivalent macro-scale systems would not. As a result of nonlinearities, characterizing the behavior of these devices becomes more difficult. The work covered in the second chapter recognizes the nonlinearity and develops means to better understand the behavior of the devices and how it corresponds to the input signal and other operation conditions. Modeling and identification of the nonlinear behavior of dynamic systems has been the focus of a large number of studies. These efforts include both non-parametric identification methods [25] and parametric identification methods [26, 27, 28]. Here, a parametric identification scheme is developed and applied to study the nonlinear dynamic behavior of clamped-clamped micro-resonators.

In addition to system parameters such as the modal mass, equivalent viscous damping, linear and nonlinear stiffnesses and the modal force, a parameter of interest is the axial force that exists within the clamped-clamped beam resonators. The axial force, and subsequently the average stress level within these devices are especially of interest in composite MEMS devices [29, 30]. These residual stresses can be produced during the fabrication process and they can significantly affect the performance of the device by shifting the resonance frequencies or by producing a non-flat equilibrium position. It is assumed that residual stress within the resonators only affects the resonance frequencies. Through a synchronization process between the identified linear natural frequencies and those of a linearized model, the axial force and residual stress values are identified in this dissertation.

Ayela and Fournier [31] developed a parametric identification method for a weakly anharmonic system. In their paper, the nonlinear behavior of electrostatic

cally excited micro-machined silicon resonators is examined. A first-order approximation is used to describe the behavior of a single-degree-of-freedom system with a cubic nonlinearity and the excitation, damping, and nonlinearity are assumed to be weak. The system is modeled by using equation (1.1) and the approximation is presented as equation (1.2).

$$\frac{d^2x}{dt^2} + \frac{\lambda}{a} \frac{dx}{dt} + \omega_0^2 x = -\beta x^3 + \frac{F_{\approx}}{a} \cos(\omega t) \quad (1.1)$$

$$x(t) \approx A \cos\left(\left(\omega_0 + \frac{3\beta}{8\omega_0} A^2\right)t\right) \quad (1.2)$$

Within these equations, x is the transverse displacement and a function of time t , a is the mass coefficient, λ is the damping coefficient, ω_0 is the natural frequency, β is the nonlinear stiffness coefficient, F_{\approx} is the amplitude of the external applied force, ω is the excitation frequency, and A is the amplitude of the response. From the first-order approximation, an equation is determined to describe the relationship between the response amplitude and the excitation frequency. This relationship is given as equation (1.4) with the new variables defined in equation (1.3). Derivatives of this equation are used to obtain an equation for the change in the amplitude with respect to changes in frequency. The equation for the change in the response amplitude as a function of the frequency difference is given as equation (1.5).

$$\Gamma = \frac{F_{\approx}}{2a\omega_0}, \quad X = \frac{3\beta}{8\omega_0}, \quad \epsilon = \omega - \omega_0 \quad (1.3)$$

$$\left[(\epsilon - X A^2)^2 + \lambda^2 \right] A^2 = \Gamma \quad (1.4)$$

$$\frac{dA}{d\epsilon} = \frac{A(X A^2 - \epsilon)}{\epsilon^2 + \lambda^2 + X A^2(3 X A^2 - 4 \epsilon)} \quad (1.5)$$

This derivative is then used to derive equations for the amplitudes and frequencies corresponding to maximum amplitude values for frequency values corresponding to the forward sweep and the backward sweep. An equation for the frequency difference between the maximum amplitude for an upward sweeping frequency and the location where the amplitude jump occurred is also determined. They also determined an equation for the critical forcing value required for this amplitude jump to occur. Along with this, they derived an equation for the critical amplitude, which is the minimum amplitude necessary for jumps to occur in the frequency-response curve. By using the equations for these seven parameters, they are able to determine the parameters for the weakly nonlinear system with a cubic nonlinearity from two nonlinear frequency-response curves; that is, the response curve obtained for an upward sweep and the response curve obtained for a downward sweep. In figure 1.1, the different parameters are shown in the frequency-response curve.

Slight modifications of the method also allowed the formula to be applied to a system exhibiting softening nonlinear behavior, where the nonlinear stiffness coefficient, β , has a negative value. This method requires that static measurements are made to obtain linear parameters and that the remaining coefficients be calculated from the dynamic measurements. By using this identification scheme, Ayela and

the excitation, and EI is the product of the Young's modulus and the moment of inertia of the beam. An over-dot ' ' is used to represent a derivative with respect to time and a prime ' ' is used to indicate a derivative with respect to position. With the assumption that the beam is weakly damped and weakly nonlinear and that there are no cases of internal resonance, the authors approximated the spatial response of the beam by the undamped linear mode whose natural frequency is closest to the excitation frequency. The method of multiple scales is used with this model to obtain a first-order approximation of the beam's response. The modulation equations are also obtained to describe the time variations of the amplitude a and phase γ . The first-order approximation and modulation equation used are shown in equations (1.8) through (1.9).

$$v(s, t) = a \cos(\Omega t - \gamma) \Phi_n(s) + H.O.T. \quad (1.7)$$

$$a' = -\mu a - \frac{1}{2} \alpha_d c a^2 + \frac{f}{2\omega_n} \sin(\gamma) \quad (1.8)$$

$$a \gamma' = \sigma a - \frac{\alpha}{4\omega_n} a^3 + \frac{f}{2\omega_n} \cos(\gamma) \quad (1.9)$$

Within these equations, the undamped linear mode shape is represented by $\Phi_n(s)$ and $H.O.T.$ represents higher order terms. The modal damping coefficient μ , the nonlinear modal stiffness coefficients α and α_d , and the modal excitation amplitude f are obtained through reduced order modeling. The detuning parameter σ corresponds to the difference between the excitation frequency and the systems natural frequency. The modulation equations are then used to relate the excitation frequency and excitation level to the response amplitude. The frequency-

response equation and force-response equation are shown as equation (1.10) and equation (1.11), respectively.

$$\sigma_{1,2} = \frac{\alpha}{4\omega_n} a^2 \mp \sqrt{\frac{f^2}{4\omega_n^2 a^2} - \left(\mu + \frac{1}{2} \alpha_d c a\right)^2} \quad (1.10)$$

$$f = 2\omega_n a \sqrt{\left(\mu + \frac{1}{2} \alpha_d c a\right)^2 + \left(\sigma - \frac{\alpha}{4\omega_n} a^2\right)^2} \quad (1.11)$$

As with the previous method, the linear natural frequency of the beam was determined independently of the nonlinear parameters. In this case, the linear natural frequency is obtained by applying very low amplitude excitations to minimize the nonlinearity of the response. Within this work, the authors developed means to calculate parameter values for the model both with and without the presence of the quadratic damping used to model air drag. For a model including only linear damping, the damping was calculated by using the excitation level, linear natural frequency, and the peak amplitude value from one set of frequency-response data. The model which includes nonlinear damping requires peak amplitude values for two excitation levels. The nonlinear stiffness parameter is calculated from the linear natural frequency and the frequency and amplitude value at the peak of the response. Because the peak amplitude is determined by fitting a cubic polynomial to the experimental data, the authors suggest excitation levels below a critical level to avoid jumps [33] in the frequency-response data. A curve fitting procedure was also employed within this work on the basis of a least-squares data fitting with a Gauss-Newton method.



Figure 1.2: Structure of piezoelectric, micro-scale clamped-clamped resonator.

The micro-resonator design studied in this dissertation consists of a clamped-clamped micro-structure machined out of a composite wafer [1], as shown in figure 1.2. The dynamic characteristics of the resonators provide spectral filtering of the electrical signals. In order to produce the desired piezoelectric actuation and sensing capabilities, the device is fabricated from a composite wafer [2]. The different layers of one style utilizing the piezoelectric properties of lead zirconate titanate (PZT) are shown in figure 1.3. The suspended structure is produced by removing a portion of the silicon substrate from underneath the oxide layer. This silicon dioxide layer, which provides the primary stiffness for the resonator, offsets the neutral axis of the structure from the centerline of the piezoelectric film, and the two platinum layers serve as electrodes for the PZT. The top electrode is separated to create input and output ports for the micro-resonator. While studies have been conducted to determine an electrode shape that selectively excites a single vibration mode [34], these devices use quarter length electrodes to maximize the device response. Representative dimensions of geometry corresponding to figure 1.3 are presented in table 1.1.

In a second type of micro-resonators that is studied, aluminum gallium arsenide (AlGaAs) is used for the piezoelectric layer [35]. For this style of resonator,

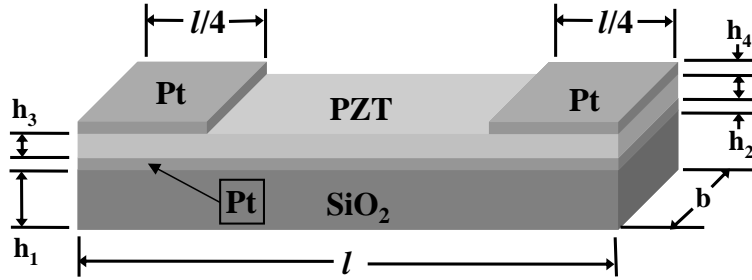


Figure 1.3: PZT resonator and geometry.

Table 1.1: Representative PZT resonator dimensions.

Dimension	Symbol	Value
Resonator Length	l	200 μm
Width of all layers	b	20 μm
Thickness, SiO ₂	h_1	1.06 μm
Thickness, bottom Pt	h_2	135 nm
Thickness, PZT	h_3	530 nm
Thickness, top Pt	h_4	200 nm

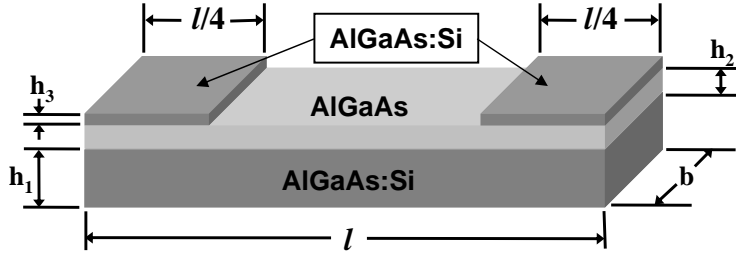


Figure 1.4: Structure of AlGaAs micro-resonator.

the two electrode layers are produced by doping AlGaAs with silicon (AlGaAs:Si). The thickness of the bottom layer of AlGaAs:Si is increased in this design to provide additional stiffness for the resonator and eliminate the need for an additional layer, such as the SiO₂ layer of the PZT resonators. Some of these resonators are being fabricated to be thicker than the PZT resonators. This produces a stiffer device resulting in higher resonance frequencies, and this device requires high excitation levels before it exhibits nonlinear behavior. This design also helps eliminate some of the problems that can arise when materials with different lattice structures are placed together on a composite wafer. The arrangement of the three layers of the AlGaAs micro-resonators are shown in figure 1.4. One set of dimension values for this resonator type are presented in table 1.2.

The arrangement of some of the key components of the experimental setup is illustrated in figure 1.5. With the sample fixed in a radio frequency (RF) probe station, a function generator or dynamic signal analyzer is used to apply a harmonic signal while the response is monitored by using laser interferometry. After initially conducting the frequency sweep in a quasi-static fashion, simulations are conducted with the identified parameter values and it is determined that a sweep-sine signal

Table 1.2: Representative AlGaAs resonator dimensions.

Dimension	Symbol	Value
Resonator Length	l	200 μm
Width of all layers	b	10 μm
Thickness, bottom AlGaAs:Si	h_1	2.0 μm
Thickness, AlGaAs	h_2	1.0 μm
Thickness, top AlGaAs:Si	h_3	0.5 μm

from the analyzer can be used to obtain valid results. The signal produced by the laser vibrometer is sent back to the analyzer to produce a frequency-response plot. A representative frequency-response data set is shown in figure 1.6, where the response amplitude is given in nanometers and the excitation frequency is given in kilohertz. Data represented by asterisks ‘*’ correspond to an increasing frequency sweep and data represented by circles ‘o’ correspond to a decreasing frequency sweep. Although the data are shown for both forward and backward frequency sweeps, only the forward sweep data are used in the parametric identification scheme of this dissertation.

Within chapter two, the model is developed and analyzed for the piezoelectric micro-scale resonator. There, the identification scheme is further discussed and the parameter trends determined are presented and examined.

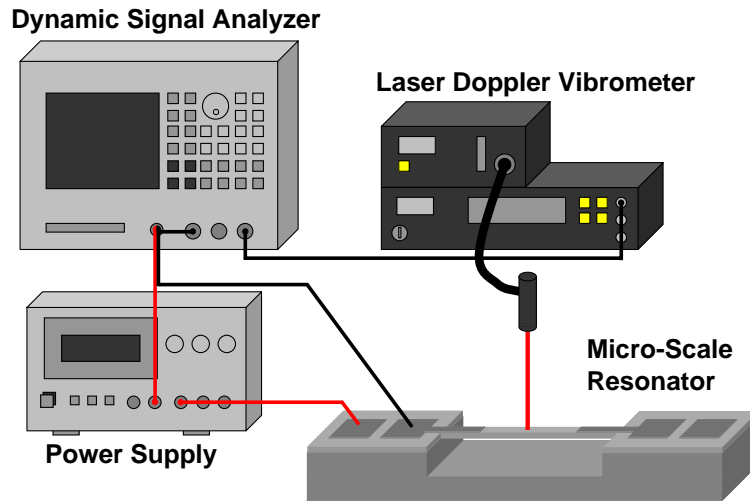


Figure 1.5: Experimental arrangement showing how a laser vibrometer is positioned to examine transverse vibrations of the resonator. The resonator is excited by signals input to the drive electrode.

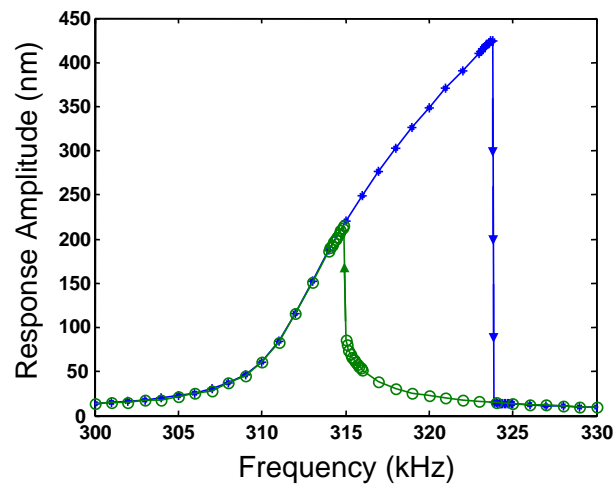


Figure 1.6: Experimental frequency-response data obtained for a 200 μm PZT resonator. The asterisks '*' correspond to forward sweep data and the 'o' correspond to backward sweep data.

1.2 Intrinsic Localized Modes

In addition to studying the nonlinear behavior of single piezoelectric micro-scale resonators, the effect of the nonlinearity on the dynamic behavior of these resonators are to be studied when they are coupled together to form large arrays. Following successful work with single resonator devices, arrays are being developed that utilize mechanical coupling to produce more sophisticated filters [36, 37].

For a number of decades, localization phenomena have been studied in the solid-state physics literature [38, 39, 40, 41]. In the late 1980s, theoretical studies discovered a type of localization that resulted from the nonlinearities within a lattice and not due the presence of defects [42]. These localizations, called Intrinsic Localized Modes (ILMs), are also known as discrete breathers (DBs) [43, 44] due to their discovery through a second, separate research path. A large number of experimental studies of these localization phenomena have been conducted in systems ranging from electronic and magnetic solids to nonlinear photonic structures to Josephson Junctions [45, 46, 47].

In recent work, Sato, Hubbard, Sievers, Ilic, Czaplowski, and Craighead [48] and Sato, Hubbard, English, Sievers, Ilic, Czaplowski, and Craighead [49] extended this study of ILMs into the field of microelectromechanical systems (MEMS). They conducted experiments with silicon nitride micro-cantilever arrays uniformly driven by lead zirconate titanate (PZT) actuation in a sinusoidal manner. In order to produce localization within this uniformly driven system, the silicon nitride micro-cantilever array is designed to consist of repeating cantilever pairs, as shown in

figure 1.7(a). Adjacent cantilevers are connected by a segment of the silicon nitride that extends beyond the PZT base. The dynamic behavior of the array is modeled by using the Klein-Gordon equations [50]. The model presented in (1.12) and (1.13) describes damped oscillators with linear coupling between adjacent oscillators. Both α and the x variables are functions of time and the over-dots are used to represent derivatives with respect to time. Since the cantilevers are driven by an excitation with a sufficiently large magnitude, the cantilevers are treated as nonlinear oscillators. The coupling between the cantilevers is simplified to be represented by only a linear stiffness term and the mass of the overhang is neglected in the work of Sato et al. [49]. The parameter values for the micro-scale cantilever pairs are determined from the geometry of the cantilevers as well as the frequency-response data collected from experiments [49]. In table 1.3, the parameters are identified and values are given. These values are used here to simulate the localization phenomena.

From the time constant given in the table, the non-dimensional damping factors are $\zeta_a = 7.67 \times 10^{-5}$ and $\zeta_b = 4.12 \times 10^{-5}$. For this set of parameter values, the strength of the nonlinearity is determined by comparing the force values produced by the cubic stiffness term in the equation of motion to the value of the force from the linear stiffness term for the same displacement value. At the center of an ILM, the nonlinear term produces ten percent of the force produced by the linear term. The observed displacements of the oscillators adjacent to the center of the ILM result in force values from the nonlinear term that are less than one percent of the force values resulting from the associated linear terms. Away from the ILM, the ratio is almost two orders of magnitude less.

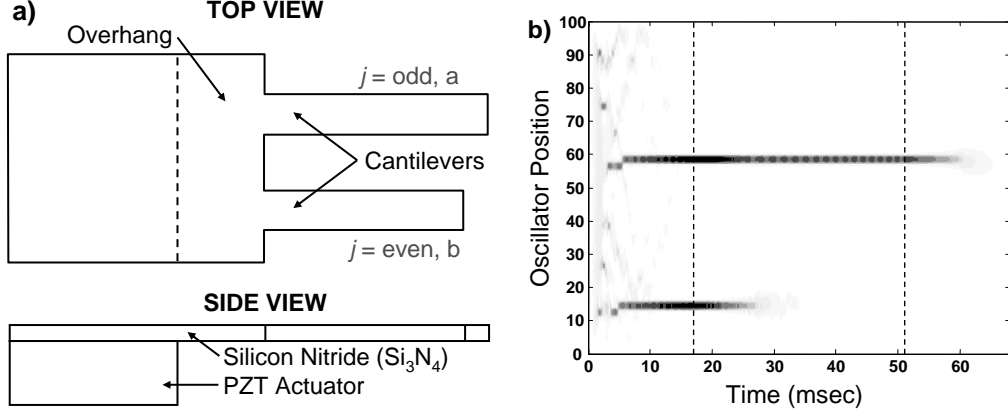


Figure 1.7: Studying ILMs in MEMS arrays: (a) unit cell of micro-cantilever array and (b) representative simulation results of localization in a micro-scale cantilever array. Time is shown on the horizontal axis and the oscillator position is shown on the vertical axis.

$$m_a \ddot{x}_{a,i} + \frac{m_a}{\tau} \dot{x}_{a,i} + k_{2a} x_{a,i} + k_{4a} x_{a,i}^3 + k_I (2x_{a,i} - x_{b,i} - x_{b,i-1}) = m_a \alpha \quad (1.12)$$

$$m_b \ddot{x}_{b,i} + \frac{m_b}{\tau} \dot{x}_{b,i} + k_{2b} x_{b,i} + k_{4b} x_{b,i}^3 + k_I (2x_{b,i} - x_{a,i+1} - x_{a,i}) = m_b \alpha \quad (1.13)$$

In recent work on piezoelectric micro-scale resonators, it has been shown that clamped-clamped micro-scale resonators need to be studied as nonlinear oscillators [20, 51, 21]. In the previous section, the model used to parametrically identify values for modal parameter of piezoelectric micro-scale resonators [52] is of the same form as the model used to study localizations with the exception of the coupling term. The parametric identification tool can be used to identify models for studying localizations in piezoelectric micro-resonator arrays. If piezoelectric resonator arrays can be engineered so that the coupling can be modeled in a manner similar to that used for the micro-cantilever arrays, then, equations such as (1.12) and (1.13) are

Table 1.3: Microcantilever array parameters.

Parameter	Value
Mass of large cantilever, m_a	5.46×10^{-13} kg
Mass of small cantilever, m_b	4.96×10^{-13} kg
Time constant, τ	8.75×10^{-3} sec
Linear stiffness of large cantilever, k_{2a}	0.303 N/m
Linear stiffness of small cantilever, k_{2b}	0.353 N/m
Nonlinear stiffness, $k_4 = k_{4a} = k_{4b}$	5.0×10^8 N/m ³
Interconnect stiffness, k_I	0.0241 N/m
Acceleration magnitude, α_0	1.0×10^4 m/s ²

applicable to these resonator arrays and it may be possible to use these equations to study localization in piezoelectric, micro-scale resonator arrays.

In figure 1.7(b), representative results obtained from a simulation conducted with these equations for an array of fifty cantilever pairs are shown. The shading used in this figure corresponds to the energy levels, with the darker regions representing the higher energy levels characterized by large amplitude oscillations. In order to promote the occurrence of localizations, a uniform excitation is applied to the array with a carefully designed excitation frequency profile, as shown in figure 1.8. For the first 2500 periods of oscillation that last for 17.0 milliseconds, the excitation frequency is increased linearly from the array's highest natural frequency, which is 146.8 kHz, to a value three percent higher in order to promote the development of localizations. The reasoning behind this process is explained in the work of Lifshitz

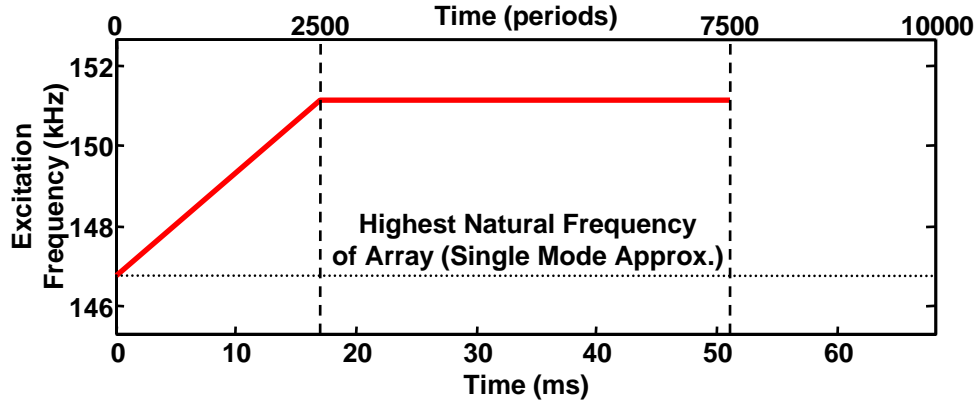


Figure 1.8: Excitation frequency profile for uniform excitation within numerical simulation.

and Cross [36], through their study of the nonlinear frequency-response behavior of arrays of coupled nonlinear oscillators with cubic nonlinearities. Within this work, they were able explain nonlinear behavior observed in the experimental work of Buks and Roukes [53]. Lifshitz and Cross utilized numerical methods to identify stable response curves for an array of sixty-seven parametrically excited, coupled nonlinear oscillators. One of the stable response curves started at the array’s highest linear frequency and was found to increase in amplitude as the frequency was increased. While their study focused on parametrically excited oscillators, similar behavior would be expected for non-parametric excitation. During the second phase of the simulation, which lasts for 5000 periods of oscillation or 34.1 milliseconds, the excitation frequency is held constant at a value near 151.2 kHz, a frequency value that is three percent higher than the array’s highest frequency. The final phase of the simulation, which is also 2500 periods of oscillation in length, is characterized by the removal of the excitation.

Conducting the simulations in this way, it is possible to observe a number of different phenomena related to mode localization. The most commonly observed behavior is ‘unlocked ILMs’. This type of localization occurs during the initial chirp phase of the excitation. Since the unlocked ILMs have relatively small displacement magnitudes, they are capable of moving easily from one location on the array to another. They tend to be short lived and quickly decay. In figure 1.7(b), unlocked ILMs can be seen early in the simulation. Another type of phenomenon that can be observed is ‘locked ILMs’. Locked ILMs oscillate with larger amplitudes than unlocked ILMs, and as a result, they tend to be fixed at a single location on the array. In figure 1.7(b), an example of locked ILMs is shown at position fourteen. When the oscillation frequency of a locked ILM becomes synchronized to the excitation frequency, the ILM will persist as long as the excitation is applied. These localizations are called ‘pinned ILMs’. A pinned ILM can be seen in figure 1.7(b) at position fifty-eight.

Of these different types of ILMs, the pinned ILM is of interest to this dissertation. In order to produce these localizations, the array of oscillators is initialized with zero velocities and small random displacements having values between $\pm 50 \text{ nm}$ in these simulation. This randomness results in a considerable amount of uncertainty within the simulations, since it is not known whether a particular choice of initial conditions will result in localization. Since this type of ILM has the largest amplitude, remains spatially fixed, and endures as long as the system is excited; this type of localizations has the most potential to influence the behavior of micro-scale resonator arrays.

Of the different types of ILMs, pinned ILMs are the most likely to cause damage to a resonator array. If the design of an array does not accommodate this phenomenon, the motion of the resonators may exceed safe levels producing increased amounts of wear or mechanical failure. In addition to the potential damage that may occur to the mechanical system, the sensitive electronics used to monitor the output signal of the piezoelectric array can be damaged by unexpected high current levels. To avoid these potential failure modes, it will be necessary for engineers to be aware of this phenomenon and the conditions under which they occur.

While unwanted localizations within a resonator array can result in the failure of a device, if this phenomenon can be anticipated and controlled, this may provide a means to drastically improve the performance of the arrays or lead to a completely new type of technology. Since pinned ILMs are spatially fixed and persist as long as the system is being driven, once they occur, their behavior is quite predictable. In addition, further work [54] has shown that the location of a pinned ILM can be manipulated by artificially creating an impurity within the array in the proximity of the center of the localization. Similarly, by quickly moving this artificial defect across the location of the localization, a pinned ILM can be terminated. It was also discovered that a localization event could be created through the addition of an artificial impurity and then gradually returning the array to its defect free state after the ILM is formed [55]. An artificial impurity mode can be produced within a piezoelectric micro-scale resonator array by selectively applying a DC bias. This ability to control pinned ILMs within an array makes this phenomenon quite attractive for potential advances in the development of resonator arrays.

In order to better understand these intrinsic localized modes, in this dissertation studies are conducted to explore the relationship between ILMs and nonlinear normal modes. Nonlinear normal modes are a special class of solutions to nonlinear systems, defined on the basis of geometric concepts [56]. These modes can be thought of as nonlinear versions of the normal modes studied in linear systems. These modes are synchronous periodic solutions to the nonlinear equations of motion of a system. They provide a nonlinear relationship describing the behavior of one degree-of-freedom within the system as a function of the behavior of another. Various methods exist to derive these relations including the restricted normal mode approach [44], the method of multiple scales approach [56] as well as other asymptotic methods [57]. A mathematical simplification called the Rotating Wave Approximation (RWA) [58] is used to obtain spatial properties corresponding to localizations but this method retains the frequency dependence unlike the nonlinear vibration modes. The RWA simplification is unable to provide an equation for the relationship between oscillators in the same manner as many of the nonlinear vibration mode methods.

In this dissertation, by using the different analytical methods examined for studying ILMs, equations are derived to relate the oscillator amplitudes that make up the ILM profile. For a number of the methods employed, the presence of terms of the form $(\omega_k^2 - \omega_j^2)$ and $(9\omega_k^2 - \omega_j^2)$ in the denominators of coefficients in the derived equations reveal a sensitivity to one-to-one and three-to-one internal resonance conditions. When the indices j and k are selected to represent adjacent oscillators, the potential for internal resonance exists. Although these conditions

do not exist and solutions are obtained, systems with these conditions have been considered to study how these internal resonance conditions affect the behavior of intrinsic localized modes. With the original parameter values given in table 1.3, the resulting resonance frequencies of the two types of oscillators are incommensurate, with a relationship of approximately $1.132 : 1$.

In the third chapter, the nonlinear analyses undertaken to examine if a nonlinear vibration mode can be used to realize an ILM are presented. The results obtained from the nonlinear analyses are examined, discussed, and it is shown that an ILM can be realized as a forced nonlinear vibration mode. Potential internal resonance conditions are also investigated to determine how the localizations are affected.

1.3 Cantilever Beam Impactor System

In the fourth chapter, the dynamic behavior of a flexible cantilever beam is studied to compare an unconstrained response with the system's response when a compliant material is positioned within the range of motion of the beam tip resulting in periodic 'soft' impacts. In figure 1.9, a diagram of the system of interest is shown. Some important system parameters for this test apparatus are listed in table 1.4. Studies have found that systems such as this one where soft impacts occur can be successfully modeled with a piecewise linear representation of the system's stiffness and damping (e.g., [59]). The difference between the system's response for unconstrained conditions and constrained conditions is examined in an effort to develop

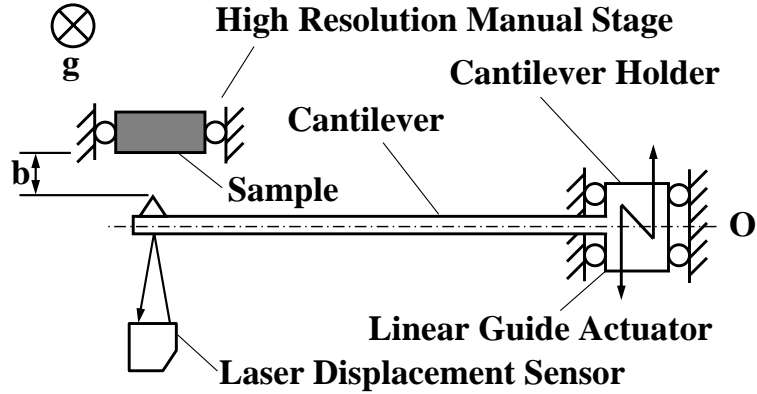


Figure 1.9: Diagram of experimental test apparatus.

a method to determine the critical separation distance between the center of oscillation of the beam and the surface of the contact material that would correspond with grazing.

Grazing is the condition in an impact system where contact occurs with a zero velocity. Examples of some different response conditions for an impact system are presented as phase portraits in figure 1.10 for a single-degree-of-freedom system. The periodic response represented by the curve of short dashes, A , is an example of the system's behavior for unconstrained conditions, where the oscillator is free to vibrate harmonically. The system's behavior for grazing conditions is shown as the solid curve B . The curve touches but does not pass through the boundary Σ , separating the two regions of the system's behavior. The periodic response represented by the curve of long dashes, C , demonstrates how the response is affected by constrained conditions for a piecewise linear model with region f_0 corresponding to no contact dynamics and f_1 corresponding to contact with the constraining material.

Table 1.4: Important dimensions of experimental test apparatus.

Parameter	Value
Beam Material	Phosphor Bronze
Density	8.8 gram/cm ³
Young's Modulus	117.0 GPa
Beam Length	436.0 mm
Beam Width	20.0 mm
Beam Thickness	0.8 mm
Impactor mass	0.8 gram

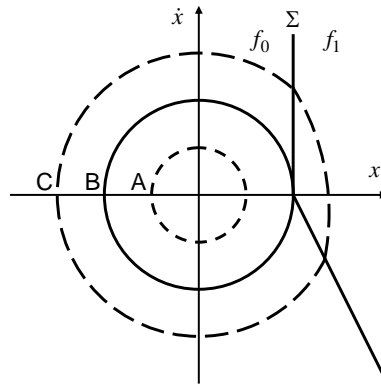


Figure 1.10: Diagram of different behavior within an impact system. Curves A , B , and C represent unconstrained, grazing, and constrained conditions, respectively.

Grazing bifurcations, which are changes in behavior resulting from a transition through the grazing condition, have been found to produce a wide range of behavior including periodic oscillations, quasi-periodic oscillations, period-doubling, and chaotic oscillations [60, 61, 62]. The desire to understand how a system's behavior changes when transitioning through grazing has led to studies being performed for a number of different systems such as impact micro-actuators [63], periodically excited strings [64], and atomic force microscopes [65, 66]. Through these studies, methods have been developed to describe low velocity, near-grazing behavior by discrete mappings [67, 68]. As this dissertation's investigation into the behavior of a system at and around the grazing point is also motivated by a particular system, a complete model is developed so that the simulated behavior agrees with experimental observations.

While the classifications described by figure 1.10 are used within chapter four, the system examined is much more complicated than a single-degree-of-freedom model and considerably more complex behavior is observed. While many studies have found that relatively simple models, i.e. a single mode approximation [69], can be used successfully to study impact dynamics, a multi-mode approximation is utilized in this dissertation. The system examined within this study includes a flexible cantilever beam that experiences oscillation amplitudes of sufficient magnitude such that a nonlinear model is necessary to describe its behavior [70].

The desire to understand how a grazing bifurcation will affect the response of a system is often motivated by the desire to develop an effective control scheme to avoid instabilities and produce the desired behavior [71]. Within the work presented

in chapter four, motivated by the tapping mode operation method of atomic force microscopy (AFM), it is desired to maintain near-grazing behavior as the distance between the cantilever and the surface of the contact material varies arbitrarily. This would ensure that a minimum amount of force is being applied to the surface of the sample by the probe tip. This is especially important when using AFM to study delicate samples such a living biological specimen [72]. Efforts to increase the resolution of AFM images has resulted in decreases in the size of the probe tip and methods are required to minimize the contact force so that the decreased contact area does not result in high contact pressure levels that will damage and destroy the sample [73].

With the aid of a scale model test apparatus, preliminary work is done to study the unique nonlinear phenomenon associated with a grazing bifurcation. Through the identification of a characteristic of the response that changes significantly as a function of the separation distance and can be easily monitored, a control scheme may be developed in order to maintain near-grazing behavior. Experimental observations of the cantilever probe of a commercial AFM system are compared and found to show qualitative agreement with the macro-scale results.

1.4 Scope and Organization of Dissertation

Within this dissertation, the nonlinear behavior of various beam and beam-like structures is explored. Analytical models are developed and utilized to study these systems. Reduced order models are developed to facilitate further analysis of these

systems and to conduct numerical simulations. Experiments are performed and data is used to identify system parameters and verify behavior predicted in simulations. Through these studies, a greater understanding of the nonlinear phenomena is gained and methods to utilize them are developed.

The organization of the rest of the dissertation is as follows. In the second chapter, the development and implementation of a multi-variable parametric identification scheme are discussed for characterizing piezoelectric micro-scale resonators from nonlinear frequency response data with jumps. In the third chapter, the investigation of a nonlinear localization phenomenon in micro-scale resonator arrays is discussed and the relationship to forced nonlinear vibration modes is explored. The fourth chapter contains an investigation into the nonlinear behavior of a cantilever beam impactor system and a period doubling phenomenon associated with grazing bifurcation. Concluding remarks are collected in the final chapter and presented along with recommendations for future work.

Chapter 2

Parametric Identification

Within this chapter, the development and implementation of a parametric identification scheme for studying systems that exhibit Duffing-like nonlinear behavior is discussed. The nonlinear beam model is developed and the process utilized to obtain a frequency-response equation and a critical points equation is described in the first section. The development of the identification scheme is discussed in the second section along with results obtained through its application to both PZT and AlGaAs devices. In the third section, the identification scheme is utilized to obtain parameter values for multiple data sets in order to study how changes in the operating conditions affect the performance of a device. Methods are also discussed regarding how these parameter trends can be used for the characterization of material properties.

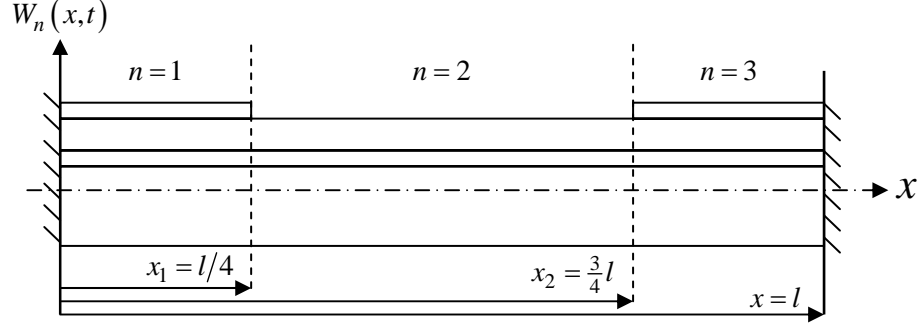


Figure 2.1: Diagram of PZT resonator identifying spatial coordinate and three sections.

2.1 Resonator Model

The frequency-response data from the micro-scale resonators, shown in figure 1.6 in chapter one, clearly reveals nonlinear characteristics. Although the dimensions of some of the resonators may suggest that a plate model may be appropriate, a beam representation is found to adequately model the dynamic behavior of the device. To account for the nonlinear behavior of the resonators within the model, both axial stretching and nonlinear curvature are considered [74]. For the resonators studied, the nonlinear curvature is found to be negligible. Because of this assumption, only the axial stretching is included when modeling the traverse deflection W_n as a function of axial position x and time t .

$$\begin{aligned}
 \left[P_n(t) \bar{h}(x) \right]_{,xx} &= \rho A_n W_{n,tt} + c W_{n,t} + (EI_n W_{n,xx})_{,xx} - P_0 W_{n,xx} \\
 &\quad - \sum_{m=1}^M \left[\frac{EA_m}{2l} \int_{l_{m-1}}^{l_m} (W_{m,x})^2 dx \right] W_{n,xx}
 \end{aligned} \tag{2.1}$$

Within equation (2.1), the parameters and variables used are as follows: mass per length ρA_n , viscous damping coefficient c , bending stiffness EI_n , axial force P_0 , axial stiffness EA_n , axial force from the piezoelectric layer P_n , and $\bar{h}(x)$ is a discontinuous function that describes the separation between the neutral axis and the applied axial force. This separation produces the distributed moment that excites the resonator [21]. The subscripts n and m are used to identify the sections of the stepwise axially-varying geometry of the structure and M is the total number of sections. The summation is required to calculate the total axial stretching within all of the sections. In figure 2.1, the three sections of the PZT resonator are shown. Subscripts following a comma ‘,’ indicate partial derivatives. To complete the model, boundary conditions and compatibility conditions are required. The boundary conditions constrain the displacement and slope of the beam at each end to be zero. Since these resonators are made up of three different segments, the displacement profile is separated into three sections that require continuity at the two interfaces. In order to accomplish this consistency, the compatibility conditions require that the displacement, slope, moment, and shear be equal on both sides of each of the connections. The composite structure of the resonators also requires additional calculations to obtain averaged properties such as the bending stiffness and the axial stiffness. These values are calculated based upon the assumption that the effect of the coupling between bending and stretching is negligible. With the nonlinear integro-partial differential equation, the boundary conditions, the compatibility equations, and the averaged properties, the model of the resonator is complete.

In order to facilitate the analysis of this model, the Galerkin procedure is employed. Noting that the response range of interest is close to the resonator's first natural frequency, a single mode approximation is used, as shown in (2.2). Through this procedure, the simplified model takes the form of a forced Duffing oscillator, shown as (2.3) where $z(t)$ is the temporal amplitude. The coefficients of this equation, to be identified through the parametric identification scheme are the following: i) the modal mass \bar{m} , ii) the equivalent viscous damping coefficient \bar{c} , iii) the linear stiffness coefficient k , iv) the nonlinear stiffness coefficient α_3 , and v) a modal force parameter F .

$$W_n(x, t) = \phi_n(x) z(t) \quad (2.2)$$

$$\bar{m} \ddot{z}(t) + \bar{c} \dot{z}(t) + k z(t) + \alpha_3 z^3(t) = F \cos(\omega t) \quad (2.3)$$

The over-dots in (2.3) are used to represent time derivatives. A harmonic excitation is assumed in arriving at (2.3). The different modal coefficients are defined by

$$\bar{m} = \sum_{n=1}^3 \left\{ \int_{l_{n-1}}^{l_n} \phi_n(x) [\rho A_n \phi_n(x)] dx \right\} \quad (2.4)$$

$$\bar{c} = \sum_{n=1}^3 \left\{ \int_{l_{n-1}}^{l_n} \phi_n(x) [c \phi_n(x)] dx \right\} \quad (2.5)$$

$$k = \sum_{n=1}^3 \left\{ \int_{l_{n-1}}^{l_n} \phi_n(x) [EI_n \phi_n^{IV}(x) - P_0 \phi_n''(x)] dx \right\} \quad (2.6)$$

$$\alpha_3 = \left(\sum_{n=1}^3 \left\{ \int_{l_{n-1}}^{l_n} \phi_n(x) [-\phi_n''(x)] dx \right\} \right) * \left(\sum_{m=1}^3 \left\{ \frac{EA_m}{2l} \int_{l_{m-1}}^{l_m} [\phi_m'(x)]^2 dx \right\} \right) \quad (2.7)$$

$$\hat{F}(t) = \sum_{n=1}^3 \left(\int_{x_{n-1}}^{x_n} \phi_n(x) \left\{ \frac{\partial^2}{\partial x^2} [P_n(t)\bar{h}(x)] \right\} dx \right) \quad (2.8)$$

where the primes in (2.6) and (2.6) indicate spatial derivatives and $\phi_n(x)$ is the considered mode shape function. Previous studies have shown that a forced Duffing oscillator with a hardening type nonlinearity is capable of producing a frequency-response curve with a structure similar to the experimental frequency-response data obtained from the piezoelectric micro-scale resonator [75]. Assuming that the nonlinearity, damping, and forcing to be weak and focusing on excitation frequencies close to the first natural frequency, the method of multiple scales is used to obtain an approximate solution to the nonlinear differential equation (2.3) [76]. The approximate solution for this case is found as (2.9) where H.O.T. stands for higher-order terms and the amplitude and phase are governed by (2.10) and (2.11), respectively.

$$z(t) = a(t) \cos(\omega t - \gamma(t)) + \text{H.O.T.} \quad (2.9)$$

$$\dot{a}(t) = -\mu a(t) + K \sin(\gamma(t)) \quad (2.10)$$

$$a(t) \dot{\gamma}(t) = \sigma a(t) - \frac{3}{8} \alpha a^3(t) + K \cos(\gamma(t)) \quad (2.11)$$

Periodic responses of the micro-resonator correspond to the fixed points (a_0, γ_0) of (2.10) and (2.11); that is, $\dot{a}(t) = \dot{\gamma}(t) = 0$. The fixed-point equations provide the frequency-response equation (2.12), which shows how the amplitude of the periodic

response changes with respect to the excitation amplitude and the excitation frequency. The parameter values at which the fixed points lose stability is given by the critical points' equation (2.13).

$$\left[\mu^2 + \left(\sigma - \frac{3}{8} \alpha a_0^2 \right)^2 \right] a_0^2 = K^2 \quad (2.12)$$

$$\mu^2 + \left(\sigma - \frac{3}{8} \alpha a_0^2 \right) \left(\sigma - \frac{9}{8} \alpha a_0^2 \right) = 0 \quad (2.13)$$

The variables within (2.12) and (2.13) are related to the parameters of (2.3) by the following relations.

$$\begin{aligned} \omega_0 &= \sqrt{k/\bar{m}}, & \Omega &= \omega/\omega_0, & \sigma &= \Omega - 1 \\ \mu &= \bar{c}/(2\bar{m}\omega_0), & \alpha &= \alpha_3/k, & K &= F/(2k) \end{aligned} \quad (2.14)$$

The critical points, where bifurcations occur, are satisfied by both (2.12) and (2.13). Analytical curves produced by using these equations are displayed in figure 2.2.

In order to determine the spatial function needed to calculate the coefficients for the forced Duffing equation from the nonlinear beam model, a linear approximation of the system is considered. From an analysis of this system along with the boundary and compatibility conditions, the first natural frequency and the associated mode shape are determined. This mode shape is used as the spatial function.

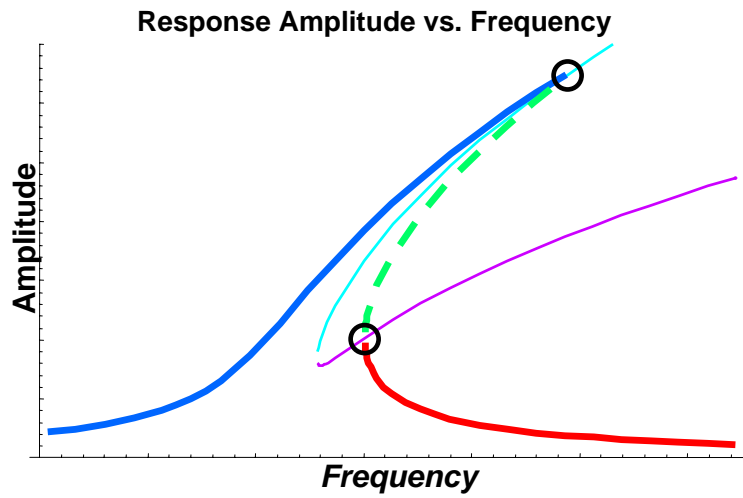


Figure 2.2: Thick lines are used to show the analytically predicted frequency-response curve, and the stable and unstable response segments are shown by solid lines and dashed lines, respectively. The thin lines are the critical-point curves, which are independent of the excitation level. The encircled intersections of these lines represent the critical points of the frequency-response curves.

2.2 Identification Scheme

With the aid of the nonlinear beam model, the system parameters are examined to determine how they affect the structure of the frequency-response curve. In order to determine how best to design the parametric identification process, the damping coefficient, the linear stiffness coefficient, the nonlinear stiffness coefficient, and the modal force parameter are examined. The influence of the modal mass is not examined because the modal mass is calculated from the nominal geometry, material properties, and approximated mode shape of the resonator. Frequency-response curves showing the affects of an increase in each of these parameters are displayed in figures 2.3(a) through 2.3(d). As expected and shown in figure 2.3(a), the damping coefficient affects the amplitude of the peak of the frequency-response curve while leaving much of the rest of the curve unchanged. The nonlinear stiffness coefficient influences the amount by which the peak of the frequency-response curve leans away from the neutral position corresponding to the first natural frequency, as illustrated in figure 2.3(b). Changing the value of the linear stiffness results in a shifting of the system's linear natural frequency and this causes the horizontal position of the peak of the frequency-response curve to change, as shown in figure 2.3(c). The modal force represents the generalized magnitude of the force being applied to the system and a change in the value of this parameter affects the response amplitude of the entire frequency-response curve most notably at the peak; this is illustrated in figure 2.3(d).

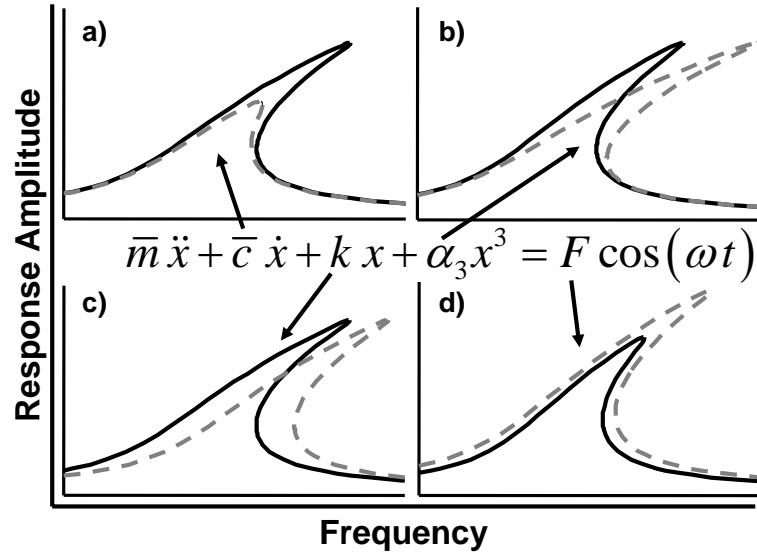


Figure 2.3: The effects of increasing parameter values on the analytical response curve. The curve depicted by using solid lines corresponds to the nominal case, and the curve illustrated by using dashed lines corresponds to the effect of increasing the following: (a) equivalent viscous damping coefficient, (b) nonlinear stiffness coefficient, (c) linear stiffness coefficient, and (d) modal force parameter.

2.2.1 Stages of identification

Based on the information presented in figure 2.3, the parametric identification scheme is developed so that the parameters with the most influence over the response are fit before the parameters that affect the response the least. A flow chart depicting an overview of the parametric identification scheme is presented in Figure 2.4. First, it is necessary to select initial values for each parameter so that the peak of the analytical curve is located within the same frequency range as the experimental data and exhibits a similar structure. While the selection of these values has a very large affect on the results of the parametric identification process, the initial values are easily determined by using the relations obtained from the Galerkin procedure and through a visual comparison of the predicted analytical curve and the experimental data.

Once the initial values are selected, a three-stage parametric identification scheme is applied to determine the optimal combination of parameter values in order to fit the analytical curve to the experimental data. In the first stage, the frequency-response equation (2.12) is utilized for a least-squares curve fitting process. The parameters determined in this section, in the order identified, are the linear stiffness coefficient, the nonlinear stiffness coefficient, and the modal force parameter. These parameters are identified by tuning each parameter as long as the difference between the analytical curve and the entire experimental data set continues to decrease. The parameters are tuned both positively and negatively for a number of different adjustment sizes.

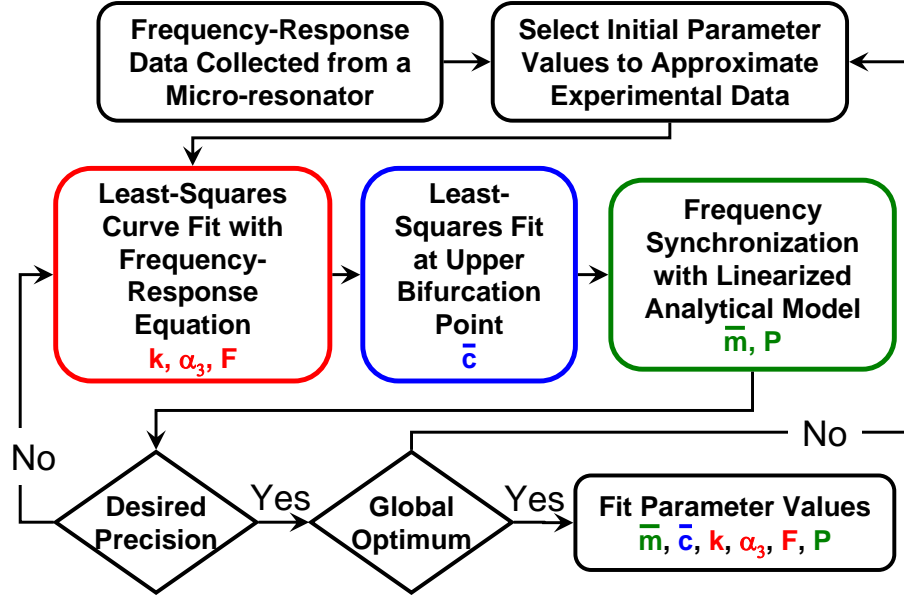


Figure 2.4: Flow chart depicting an overview of the parametric identification scheme that is used to study piezoelectric micro-scale resonators.

In the second stage of the identification process, the frequency-response equation (2.12) as well as the critical points equation (2.13) are utilized to fit the upper bifurcation point by tuning the equivalent viscous damping coefficient. As previously mentioned, the identification procedure is designed specifically to study nonlinear dynamic behavior that includes jumps in the frequency-response data. Experimental data sets that do not contain jumps can be studied with one of the identification schemes discussed previously, such as the method developed by Malatkar and Nayfeh [32]. Here, a similar tuning procedure is used but only the analytically predicted amplitude of the upper bifurcation point is compared with the amplitude of the last experimental data point before the jumps occurs. Although this does not take into account any difference between the frequency of the experimental data point and the

frequency value calculated by the model, additional iterations of the identification process account for this discrepancy through tuning of the linear stiffness coefficient. While both the modal force parameter and the equivalent viscous damping coefficient affect the amplitude value at the peak of the frequency-response curve, only the modal force parameter significantly affects the portion of the curve away from the peak. As a result, it is possible to determine a unique combination of the two parameters for a given set of experimental data.

In the final of the three stages within the identification scheme, the linearized system is used to obtain an approximate mode shape corresponding to the first natural frequency. This mode shape is determined by tuning the axial force within the linearized model to synchronize the first resonance frequency of the model with the frequency calculated from the identified parameter values. The axial force value is tuned in the same fashion as the other parameters. This provides an approximation of the micro-resonator's mode shape for this natural frequency and an axial force value that can be used to calculate the average residual stress in the resonator. By using this approximate mode shape, the modal mass value can be recalculated. This new modal mass value is then used in the next iteration of the identification process to aid in the further refinement of the other parameter values.

Upon completion of these three stages of the identification scheme, the parameter values are examined to determine if the desired level of accuracy has been obtained. If the parameter values are not determined to sufficient accuracy, the identification scheme returns to the first stage of the three-stage process using the current parameter values for the initial values. Since the system is nonlinear and

has a multi-dimensional parameter space, the possibility exists that the identification scheme may converge to a local optima and not the global optimum. To avoid selecting a local optima, after the scheme has gone through a sufficient number of iterations to produce the desired level of precision, each of the key parameter values, \bar{c} , k , α_3 , and F , are perturbed both positively and negatively to produce eight different sets of parameter values. These eight sets are then used as initial values and the results of the nine cases are compared. If the first set of parameter values is found to have the best values, then it is considered to represent the “global optimum”. The quality of each set of parameter values is determined by calculating an RMS error from comparisons of the resulting analytical values with the experimental data. In the event that the best set is one of the eight perturbed sets, these optimized values are perturbed to produce eight new sets and the same process is repeated.

2.2.2 Parameters for PZT and AlGaAs micro-resonators

The same experimental arrangement and procedures are employed for both PZT and AlGaAs micro-resonators. In figures 2.5(a) and 2.5(b), comparisons of the experimental data and the frequency-response curve obtained on the basis of the identified parameter values are shown for the PZT micro-resonator and AlGaAs micro-resonator, respectively. For the PZT micro-resonator, a minimal RMS Error value of 1.0943 nm is calculated from the forward sweep data and the identified parameter values. Although only the forward sweep data is used to determine the parameter values, the results of figure 2.5(a) show agreement with both the forward

sweep data and the backward sweep data. For this particular data set, the RMS error calculated for the backward sweep data has an even smaller value of 1.0814 nm. This indicates that although the backward sweep data is not utilized during the identification process, the information obtained can be used to predict the correct frequency response in the lower branch, including the location of a jump.

Nonlinear frequency-response data collected from a 200 μm AlGaAs resonator is presented in figure 2.5(b) along with the analytical curve representing the fit nonlinear model. Once again, the parametric identification scheme is able to match the analytical curve to the experimental data well. For the data shown in figure 2.5(b), an extremely small RMS error value of 0.5666 nm is calculated.

In table 2.1 and table 2.2, the parameter values determined by using the parametric identification scheme and numerical values calculated from the nonlinear beam model are shown for the PZT micro-resonator and AlGaAs micro-resonator, respectively. The second column of each table contains parameters calculated by using the identified axial force value. The parameters in the third column correspond to residual stress levels determined by using the wafer bow measurement method (e.g., [77]). From comparisons of the identified resonance frequencies, it can be confirmed that the AlGaAs micro-resonator is stiffer than the PZT micro-resonator. The experimental AlGaAs data also shows lower response amplitude values than the PZT resonator data for equivalent input signals. This observation is consistent with the fact that the AlGaAs resonators are stiffer and that they experience smaller transverse deflections and that the piezoelectric coupling of the AlGaAs material is weaker than that of the PZT material. However, as seen from tables 2.1 and 2.2,

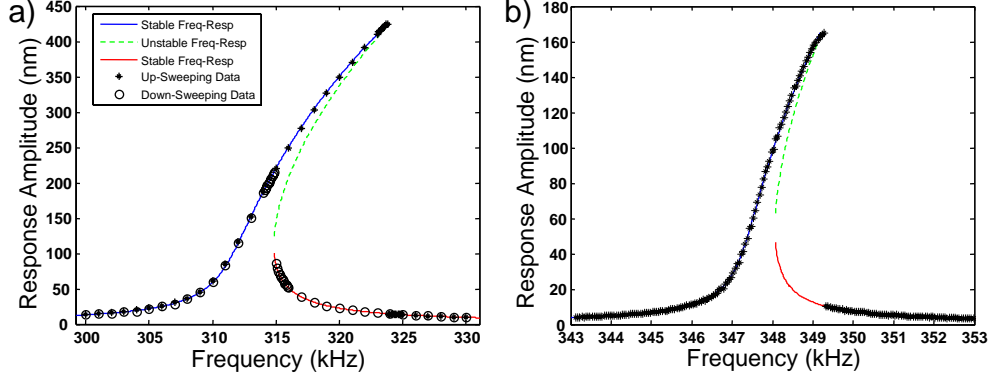


Figure 2.5: Nonlinear model fit to micro-resonator data: (a) 200 micrometer PZT resonator and (b) 200 micrometer AlGaAs resonator.

the AlGaAs resonator has a higher Q factor compared to the PZT resonator. This higher Q-amplification for the AlGaAs resonators compensates substantially for the increased stiffness and reduced piezoelectric coupling.

In the case of the PZT micro-resonator, for the identified axial force, the numerically obtained parameter values from the beam model generally agree with the identified values with the largest discrepancy being between the values obtained for the nonlinear stiffness coefficient. For the numerical values calculated with the residual stress from the wafer bow measurements, the increased stress/axial force values affect the linear stiffness coefficient and subsequently, the first resonance frequency.

For the AlGaAs micro-resonator, when comparing the parameter values within table 2.2, it is clear that the identification scheme determines the axial force/residual stress level within the resonator to be significantly lower than the value calculated from the wafer bow measurement method. The difference between these values may

Table 2.1: Comparison of parameter values for PZT resonator.

Parameters and Units	Parametric Identification	Beam Model	Beam Model (Bow Stress)
\bar{m} ($\text{kg} \times 10^{-11}$)	1.58	1.58	1.58
\bar{c} ($\text{Ns/m} \times 10^{-8}$)	7.81	—	—
k (N/m)	60.91	60.88	69.78
α_3 ($\text{N/m}^3 \times 10^{+12}$)	32.4	3.54	3.53
P ($\text{N} \times 10^{-3}$)	1.50	1.50	1.87
ω_0 (kHz)	312.61	312.55	334.61
$Q_{\text{effective}}$	397.15	—	—
σ_{average} (MPa)	43.56	43.56	54.29

Table 2.2: Comparison of parameter values for AlGaAs resonator.

Parameters and Units	Parametric Identification	Beam Model	Beam Model (Bow Stress)
\bar{m} ($\text{kg} \times 10^{-11}$)	1.13	1.13	1.06
\bar{c} ($\text{Ns/m} \times 10^{-8}$)	1.55	—	—
k (N/m)	54.02	54.02	0.225
α_3 ($\text{N/m}^3 \times 10^{+12}$)	24.6	2.84	2.92
P ($\text{N} \times 10^{-4}$)	-2.68	-2.68	-24.0
ω_0 (kHz)	347.58	347.58	23.17
$Q_{\text{effective}}$	1599.19	—	—
σ_{average} (MPa)	-8.94	-8.94	-80

occur because the wafer bow measurement determines an average across the entire wafer. The values from the wafer bow measurement method are also determined before the micro-machining of the device structure. During this process, some of the stress may be released resulting in lower stress levels. This axial force discrepancy causes the calculated values of the linear stiffness coefficient to be much smaller, resulting in a significant decrease in the calculated resonance frequencies. The deviation between the identified and calculated values for the nonlinear stiffness parameter is consistent with results obtained for the PZT resonators. This consistent deviation suggests that there may be an additional source of nonlinearity that must be taken into account in the nonlinear beam model to more accurately represent the dynamic behavior of the considered micro-resonators.

Overall, as demonstrated here, it has been possible to produce a successful curve fit to the experimental data by using the parametric identification scheme constructed on the basis of Duffing oscillator.

2.3 Trends of Identified Parameters

Here, results of preliminary investigations conducted into the variations of the identified parameter values with respect to the selected input signals or operating conditions are reported to demonstrate the ability of the parametric identification scheme to study the dynamics behavior of nonlinear systems such as MEMS devices. Different swept-sine signals with increasing amplitude values and various DC bias levels are considered. The changes in the response of the system are examined in the form

of three parameter: the modal force parameter, the linear stiffness parameter, and the nonlinear stiffness parameter.

2.3.1 Modal force and piezoelectric coefficient

In order to understand how changes in the amplitude of the applied signal affect the modal force parameter, the corresponding term in the nonlinear beam model is examined. The excitation results from the distributed moment produced by the piezoelectric material. The excitation term in (2.1) is separated into a time dependent function $P_n(t)$ and a position dependent function $\bar{h}(x)$. Following the application of the Galerkin procedure, the modal force function $\hat{F}(t)$ given by (2.8) is produced. After carrying out integration by parts twice with respect to x , (2.15) is obtained.

$$\hat{F}(t) = P_1(t) h \phi_1'(x_1) \quad (2.15)$$

By using the block force model to obtain the axial force from the piezoelectric material, the definition of the modal excitation term can be further expanded to include material properties, additional device geometry, and the applied voltage [78]. This form of the modal force is given in (2.16).

$$\hat{F}(t) = EA (d_{31}/t) V(t) h \phi_1'(x_1) \quad (2.16)$$

This equation can be used to gain additional information about the device. For a number of data sets collected from the same device for increasing drive voltage values, a complete set of parameter values can be identified. A plot of the modal force

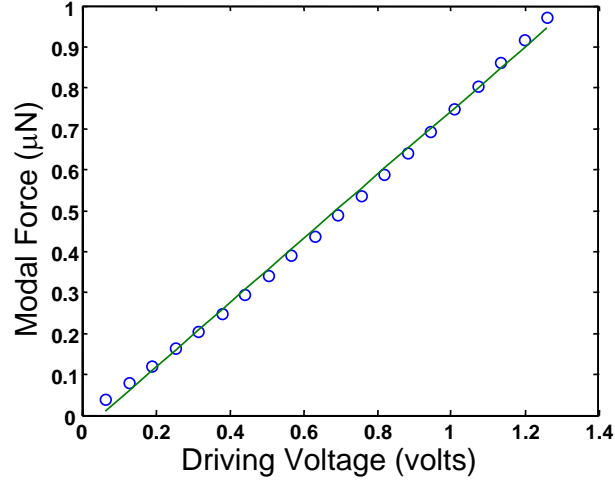


Figure 2.6: Approximating a linear force-voltage relation. The circles ‘o’ represent modal force values for different data sets and the solid line is a linear curve fit to these data points.

parameters versus the drive voltage amplitude yields a nearly linear set of points. An example of this data is displayed in figure 2.6. Rearranging equation (2.16) to solve for the piezoelectric coefficient, d_{31} , reveals a term that directly corresponds to the slope of the data points. Because this term consists of two temporal functions, it is important to note that the slope of the data points represents the ratio of the amplitudes of the two harmonic functions and a negative sign must be included to account for the phase difference. This form of the equation is shown in (2.17), where the actuator area $A = bh$, F_0 is the amplitude of $\hat{F}(t)$, and V_0 is the amplitude of $V(t)$.

$$d_{31} = - (F_0/V_0) (E b h \phi_1'(x_1))^{-1} \quad (2.17)$$

With additional information about the resonator, it is possible to calculate values for the piezoelectric coefficient. This is useful since the properties of thin-film materials often differ from their macro-scale counterparts and the properties of these materials can be dependent on the various fabrication procedures to which they are exposed. In initial applications of the identification scheme, the determined piezoelectric coefficient values range from $-116 \times 10^{-12} \text{ m/V}$ to $-192 \times 10^{-12} \text{ m/V}$. These thin-film material values are of the same order-of-magnitude as the piezoelectric coefficient values associated with bulk ceramic materials. However, the thin-film material piezoelectric coefficients are found to be smaller in magnitude.

2.3.2 Axial force, linear stiffness, and nonlinear stiffness

The addition of a DC bias to the applied signal results in a constant axial force in the micro-resonator. As the value of the DC bias increases, the peak of the frequency-response curve shifts to the right. Based on the parametric study previously discussed, the axial force produced by the addition of the DC bias affects the linear stiffness of the resonator. This behavior agrees with the fundamental understanding of the effects of an axial force within clamped-clamped beam structures. By using the nonlinear beam model, it is possible to calculate linear natural frequency values that qualitatively and quantitatively agree with the frequency changes observed in the experimental data. While the model utilized within this work does not include the effects of the hysteresis of the piezoelectric material, a basic linear approximation is compared with identified parameter values to obtain rough ranges for the

DC bias and the axial force. By using the block force model; that is, axial force = $EA(d_{31}/t)$ DC bias, refined values of this voltage-force ratio can be used to determine the piezoelectric coefficient d_{31} for the devices. By using the ratio values from this basic model, piezoelectric coefficient values ranging from $-93.3 \times 10^{-12} m/V$ to $-163 \times 10^{-12} m/V$ are determined for the PZT micro-resonators. Although this is merely a coarse approximation, these values are of a magnitude common for the piezoelectric coefficients of bulk PZT materials [78].

To qualitatively compare the identified parameters with those of the nonlinear beam model, the change in the identified first natural frequencies are shown in Figure 2.7(a) for a range of DC bias levels and the calculated changes in the first natural frequencies from the model are shown in Figure 2.7(b) for a range of axial force values.

Another parameter that is significantly affected by the addition of a DC bias is the nonlinear stiffness parameter. With an increase in the level of DC bias, the identified nonlinear stiffness parameter value is found to decrease. Similar to the observations of the linear stiffness parameter values, the nonlinear stiffness parameter values also appear to be influenced by the hysteresis of the piezoelectric material. Again, by using only a basic model, a range of axial force values is found where the value of the nonlinear stiffness decreases as the axial force increases. To qualitatively compare the identified parameters with those of the nonlinear beam model, the identified nonlinear stiffness values are shown in figure 2.8(a) for a range of DC bias levels and the nonlinear stiffness parameters from the model are shown in figure 2.8(b) for a range of axial force values, both normalized to their initial parameter

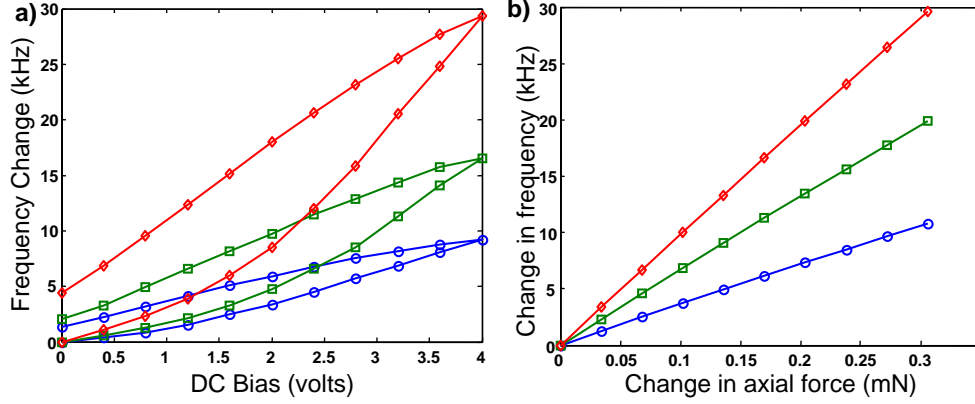


Figure 2.7: Trends of the first, linear natural frequency for different PZT micro-resonators. Diamonds correspond to 100 μm resonators, squares correspond to 200 μm resonators, and circles correspond to 400 μm resonators. Identified parameter values are presented in (a) and model prediction values are presented in (b) showing how the model is capable of explaining the parameter trends.

values. The axial force values are normalized with respect to the buckling force so that buckling occurs at a normalized axial force value of negative one.

In this section, parameter trends with respect to variations in the resonator input signals were examined by applying the parametric identification scheme to a series of data sets. The parameter trends examined included the modal force parameter values for incremental changes in the amplitude values of the drive voltage and variation of linear and nonlinear stiffness values with respect to the addition of a DC bias to the input signal. By using the nonlinear beam model, it has been possible to explain the trends of each of the parameters and produce numerical values that qualitatively agree with the identified values. While further work will be necessary to develop more complete models of the trends, identifying this qualitative

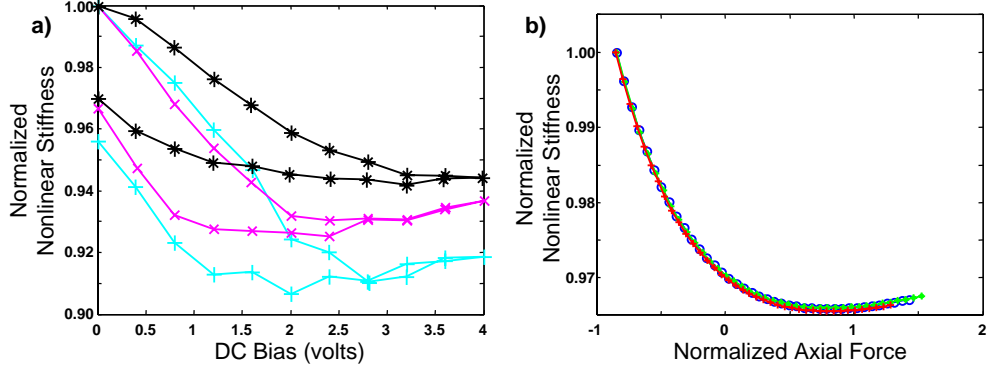


Figure 2.8: Trends of the nonlinear stiffness coefficient for different PZT micro-resonators. Identified parameter values are presented in (a) and model parameter values are presented in (b) showing qualitative agreement.

agreement is important in validating the selection of the nonlinear beam model and determining the course of future work.

2.4 Summary

A parametric identification scheme is developed to quantify the nonlinear behavior of systems that exhibit Duffing-like nonlinearities. This identification scheme is able to determine parameter values from nonlinear frequency-response data collected from PZT and AlGaAs resonator and good agreement is seen with the model values. Parameter values obtained with the identification scheme are examined to study parameter trends produced by incrementally changing the operating conditions of a device. These parameter trends are found to provide a means to calculated values for the piezoelectric coefficient of the piezoelectric material. The parameter trends are also found to show how changes in the input signal affect the performance of

the devices and agreement is seen with trends predicted by the model. In the next chapter, the effects of the nonlinearity identified in the individual resonators are investigated when they are coupled together to form resonator arrays.

Chapter 3

Intrinsic Localized Modes

In this chapter of the dissertation, a relationship is identified between the nonlinear localization phenomenon called Intrinsic Localized Modes (ILMs) and nonlinear vibration modes. The amplitude profiles of the simulated localization are examined in the first section and a number of analytical methods are explored. Floquet theory is applied to obtain stability information for the results of these analyses. The results of these methods are compared with profiles from simulations in the second section. Based on the form of a number of the analytical solutions, the effects of internal resonance conditions on the ILMs are explored in the third section of this chapter.

3.1 Analysis of Oscillator Array

While previous work [36] examined the nonlinear spectral properties of arrays of coupled micro-resonators, in this dissertation, the focus will be on the spatial characteristics of the oscillations. Although a random initialization process has been utilized to prompt the development of ILMs, as discussed in the first chapter, the perfect periodicity of the array suggests that the amplitude profile of an ILM can be analytically determined by using the properties of the array. In order to accomplish this, it is first necessary to study the amplitude profiles of simulated ILMs. After the amplitude profiles are identified from the simulations, various approaches are employed to analytically identify the amplitude values associated with a localization event in the array. Following the application of the different analysis methods, the calculated amplitude profiles are compared with those determined through the simulation. The stability of the analytically predicted motions is examined by using Floquet theory [75].

3.1.1 Intrinsic Localized Mode Profiles

In order to better understand pinned ILMs, as shown in figure 1.7 in chapter one, amplitude profiles are examined at times following the decay of most of the transient localizations. An example of these displacement profiles is shown in figure 3.1(a). The asterisk stems correspond to the larger, low-frequency cantilevers while the smaller, high-frequency cantilevers are represented by the circle stems. Within this figure, the location of the center of localization is apparent and the oscillators sur-

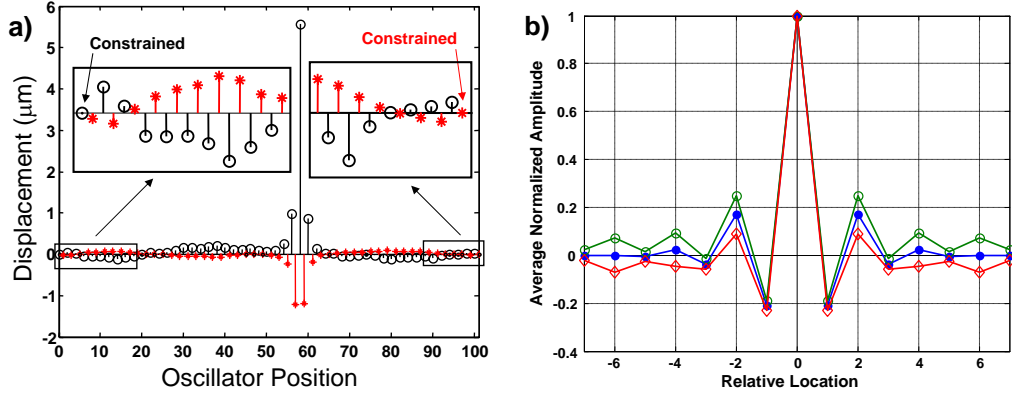


Figure 3.1: Spatial characteristics of an ILM: (a) example of a displacement profile and (b) the averaged normalized amplitude profile around localization. The horizontal axis lists the position of the oscillators relative to the center of the localization. The average normalized profile is represented by filled circles. The average plus and minus one standard deviation is represented by empty circles and empty diamonds, respectively.

rounding the center also have displacements that are significantly larger than the other oscillators in the array. After examining a number of amplitude profiles, it is observed that the displacements of the oscillators around the center of localization roughly maintain a regular pattern. To study this pattern, the displacement profile of the oscillators around the center of the localization is examined over 27.3 milliseconds during the constant frequency phase of the excitation.

In order to better observe the amplitude profile, the displacements are normalized by the value at the center of the localization and averaged. The results of this process are presented in figure 3.1(b). To produce an average profile, six percent of the profiles are omitted when determining the average. These atypical profiles

correspond to the displacement of the array when the oscillator at the center of the localization has a displacement with an absolute value less than $1\ \mu\text{m}$. Under these conditions, the displacement profile can become dominated by the influence of the transient behavior. This transient behavior consists primarily of residual unlocked ILMs and some of the boundary effects produced at either end of the array. Boundary effects are the results of the influence that the boundaries of an array have on the system's behavior causing it to vary from the ideal case of an infinite array of coupled oscillators. Magnified views of both boundaries are shown in figure 3.1(a) to illustrate how these constraints can limit the magnitude of nearby oscillators. Sato et al. [49] reported that comparable results are produced with either fixed or periodic boundary conditions. This is due to the sufficiently weak coupling that causes the boundary conditions to only affect the oscillators in their immediate vicinity. Since the standard deviations are considerably small, especially for the oscillators closest to the center of the ILM, it would appear that the average serves as a good representation of the profile maintained by the pinned ILM.

Based upon the amplitude profile shown in figure 3.1(b) and the periodicity of the array, the localization profile will be treated as symmetric about the center of the localization. By using the average normalized amplitude profile, the amplitude ratios are calculated for the adjacent oscillators moving out from the center of the localization. The ratio of the amplitude of the first oscillator from the center, henceforth to be referred to as $x_{\pm 1}$, to the amplitude of the oscillator at the center of the localization, henceforth to be referred to as x_0 , is determined to be $r_1 = -0.21$. The ratio of the amplitude of the second oscillator out from the center of the local-

ization, henceforth to be referred to as $x_{\pm 2}$, to the amplitude of $x_{\pm 1}$ is determined to be $r_2 = -0.70$. The negative values indicate that the adjacent oscillators are half a period out of phase. Moving away from the center of the localization, the amplitude ratios repeat periodically with a growing deviation. This corresponds to the periodicity of the micro-cantilever pairs.

Given the nature of the differential system used to model the nonlinear oscillators within the array, presented in chapter one as (1.12) and (1.13), an alternate method is developed to characterize the amplitude profile corresponding to a localization event. To accommodate the nonlinearity of the model, an additional cubic term is added to the previous linear relationship. With the addition of this term, it is no longer necessary to normalize the displacement profiles, as the actual values will be required to determine the coefficients to the cubic terms. As done previously, this method focuses on the oscillators around x_0 where the displacements are the largest and the effects of transient oscillations are minimal. In order to take advantage of the symmetry of the localization and to further reduce the influence of transient oscillations on the calculated amplitude ratios, the displacement values on both sides of the center of the localization are averaged and compared to the predicted displacement value. The nonlinear relationships defining the predicted displacement of $x_{\pm 1}$ are given by equation (3.1). The equations for the displacements $x_{\pm 2}$ are given by equation (3.2). In each case, the predicted displacement value is a function of only the displacement of x_0 and the coefficients to be identified.

$$X_{\pm 1}(t_n) = c_1 x_0(t_n) + c_2 x_0^3(t_n) \quad (3.1)$$

$$X_{\pm 2}(t_n) = c_3 X_{\pm 1}(t_n) + c_4 X_{\pm 1}^3(t_n) \quad (3.2)$$

These predicted displacement values are then compared with the displacement values obtained from the simulation by using the following equations.

$$E_1 = X_{\pm 1}(t_n) - \frac{1}{2} [x_{+1}(t_n) + x_{-1}(t_n)] \quad (3.3)$$

$$E_2 = X_{\pm 2}(t_n) - \frac{1}{2} [x_{+2}(t_n) + x_{-2}(t_n)] \quad (3.4)$$

The first error equation, (3.3), is employed initially to determine values for the coefficients c_1 and c_2 . The root-mean-square (RMS) value for this error equation over the same twenty milliseconds that is used for the linear relationship is calculated and minimized by using a least-squares method to identify values for the two aforementioned coefficients. The second set of coefficients, c_3 and c_4 , are identified with the aid of equation (3.4). For localization events occurring in arrays ranging from twenty to fifty oscillator pairs, the identified values show very good agreement. The averages of the identified values are as follows:

$$c_1 = -0.2060, c_2 = 2.4657 \times 10^8, c_3 = -0.6679, c_4 = 4.3477 \times 10^{10}$$

The values identified for the coefficients of the linear terms display very good agreement with standard deviations of less than two percent of the averaged values. The coefficients of the cubic terms, which are more susceptible to deviation, have slightly larger standard deviation percentages but still remain consistent. In

addition to providing a more effective means to characterize the amplitude profile of a localization produced by a simulation, the form of the amplitude relationship employed here also supports one of the analytical methods which is found to be the most successful in realizing an intrinsic localized mode.

3.1.2 Nonlinear Vibration Mode Analyses

In order to determine if the amplitude ratios associated with an intrinsic localized mode profile can be calculated analytically from a nonlinear normal mode analysis, a number of different analysis methods are employed. These include the method of multiple scales [56, 79], the restricted normal mode approach [44], as well as the real-variable and complex-variable invariant-manifold approaches [56]. Future studies will explore other asymptotic methods [57]. To perform these analyses, the damping and forcing terms are dropped from equations (1.12) and (1.13). This is done to study the invariant characteristics of the underlying conservative system. For the purpose of this section, it is mentioned that it is assumed that there are no internal resonances in the system.

Due to the characteristics of the localization and the periodic nature of the array, an additional approximation can be made to simplify the array down to a pair of coupled nonlinear oscillators. The first step in this simplification is to assume that the amplitudes of the oscillators are symmetric about x_0 as mentioned previously and supported by figure 3.1(b). The next assumption to be made is that the influence of $x_{\pm 2}$ on $x_{\pm 1}$ is negligible when compared to the influence of x_0

on $x_{\pm 1}$. This approximation is necessary for the restricted normal mode approach and it has been found to improve the results obtained by using the method of multiple scales approach. The resulting simplified model is then arranged into a general form so that the equation governing the j^{th} oscillator can be put in the form of equation (3.5). When the index j is equal to a or an odd number for the complete array model, equation (3.5) describes the larger of the micro-cantilevers. The equation of motion of the smaller cantilever corresponds to $j = b$ or when j is equal to an even number for the complete array model. This arrangement results in the center of the localization being located at one of the smaller, high-frequency cantilevers. In the work reported by Sato et al. [49], this scenario was true for all localizations observed in both the simulations and experiments.

$$\frac{d^2 q_j(t)}{dt^2} + \omega_j^2 q_j(t) + G_j = 0 \quad (3.5)$$

$$\omega_j = \begin{cases} \sqrt{k_{2a}/m_a} & j, \text{ odd} \\ \sqrt{k_{2b}/m_b} & j, \text{ even} \end{cases} = \begin{cases} \sqrt{k_{2a}/m_a} & j = a \\ \sqrt{k_{2b}/m_b} & j = b \end{cases} \quad (3.6)$$

$$G_j = \sum_k g_{1,j,k} q_k^3 + g_{2,j,k} q_k \quad (3.7)$$

In going from equations (1.12) and (1.13) to equation (3.5), the frequency ω_j and the terms G_j are introduced and defined by (3.6) and (3.7), respectively. In equation (3.6), the definition of ω_j is given for the simplified model following the definition for the complete model. The values of these terms are dependent on the index j . The term G_j includes the cubic term and the linear coupling terms from

the model. The two coefficients $g_{1,j,k}$ and $g_{2,j,k}$ are dependent on the values of the indices j and k . For the system at hand, these coefficients are defined, for both the complete model and the simplified model, by equations (3.8) and (3.9). Based on the values of the indices, these parameters are substituted into the resulting vibration mode equations following each of the analyses. Complete derivations for each of the methods presented are provided in appendix A.

$$g_{1,j,k} = \begin{cases} k_A/m_a & k = j, \text{ odd} \\ k_A/m_b & k = j, \text{ even} \\ 0 & k \neq j \end{cases} = \begin{cases} k_A/m_a & k = j = a \\ k_A/m_b & k = j = b \\ 0 & k \neq j \end{cases} \quad (3.8)$$

$$g_{2,j,k} = \begin{cases} 2 k_I/m_a & k = j, \text{ odd} \\ 2 k_I/m_b & k = j, \text{ even} \\ -k_I/m_b & k = j \pm 1, \text{ odd} \\ -k_I/m_a & k = j \pm 1, \text{ even} \end{cases} = \begin{cases} 2 k_I/m_a & k = j = a \\ 2 k_I/m_b & k = j = b \\ -2 k_I/m_b & k, j = a, b \\ -k_I/m_a & k, j = b, a \end{cases} \quad (3.9)$$

Method of Multiple Scales Approach

The method of multiple scales is a perturbation technique that uses multiple time scales, as shown in equation (3.10), to determine approximate solutions to nonlinear differential equations. In (3.10), the approximation and the derivative expansions are also shown. For this analysis, the term G_j in (3.5) is considered to have values significantly smaller than the other terms. This scaling is based on observations of the relative contributions of the different terms in the equations of motion at the center of the localization during the simulations. Both the inertia term and

the linear stiffness term produce forces with magnitudes of the same order. The amplitudes of the forces corresponding to the nonlinear term and the coupling term are one order of magnitude smaller. The procedure for this method requires that the influencing oscillator, in this case denoted by the index k , be considered as having a non-zero order $O(\epsilon^0)$ solution and the oscillator being influenced, represented by the index j , as having an order $O(\epsilon^0)$ solution that is trivial. The order $O(\epsilon^0)$ solutions are shown by (3.11).

$$T_n = \epsilon^n t, \quad x_j = x_{0,j} + \epsilon x_{1,j} + \dots, \quad \frac{d}{dt} = \frac{\partial}{\partial T_0} + \epsilon \frac{\partial}{\partial T_1} + \dots \quad (3.10)$$

$$x_{0,k}(T_0, T_1) = a_k(T_1) \cos(\omega_k T_0 + \beta_k(T_1)), \quad x_{0,j}(T_0, T_1) = 0 \quad (3.11)$$

This allows the response of the j^{th} oscillator to be defined in terms of the response of the k^{th} oscillator. The equation for the velocity of the j^{th} oscillator is obtained by taking the derivative of the displacement equation with respect to the fastest time scale T_0 . Since coupling is limited to adjacent cantilevers and the two cantilever structures have frequencies that are incommensurate, it is assumed that internal resonance will not occur. Without internal resonance, these results as well as those for the following methods will produce finite values. The procedure followed for this analysis can be found in literature [56], and the details of this analysis can be found in appendix A. Once the equations for the displacement q_j and velocity p_j of the j^{th} oscillator are derived, they are rewritten as functions of the behavior of the k^{th} oscillator.

$$\begin{aligned}
q_j &= \frac{g_{2,j,k}}{\omega_k^2 - \omega_j^2} q_k + \frac{(7\omega_k^2 - \omega_j^2) g_{1,j,k}}{(9\omega_k^2 - \omega_j^2)(\omega_k^2 - \omega_j^2)} q_k^3 \\
&\quad + \frac{6g_{1,j,k}}{(9\omega_k^2 - \omega_j^2)(\omega_k^2 - \omega_j^2)} p_k^2 q_k + \dots
\end{aligned} \tag{3.12}$$

$$\begin{aligned}
p_j &= \frac{g_{2,j,k}}{\omega_k^2 - \omega_j^2} p_k + \frac{3(3\omega_k^2 - \omega_j^2) q_k^2 g_{1,j,k}}{(9\omega_k^2 - \omega_j^2)(\omega_k^2 - \omega_j^2)} p_k \\
&\quad + \frac{6g_{1,j,k}}{(9\omega_k^2 - \omega_j^2)(\omega_k^2 - \omega_j^2)} p_k^3 + \dots
\end{aligned} \tag{3.13}$$

When examining (3.12) and (3.13), it is clear that these expressions are not applicable in the presence of internal resonances in the system. Values are assigned to j and k for $j \neq k$ and the appropriate system parameters are substituted into the manifold equations. Since only linear coupling is present, the coefficients of the second and third terms of (3.12) and (3.13) are equal to zero for all values of j and k . The remaining linear term has a value when $k \neq j$ due to the linear coupling between adjacent oscillators. The amplitude equations describing the manifold when $k \neq j$ for $k = b$ and $k = a$ are given by (3.14) and (3.15), respectively. The numerical values of the system parameters are substituted into the equations in order to obtain the numerical coefficients.

$$k = b, j = a \quad q_a = \frac{k_I m_b}{k_{2a} m_b - k_{2b} m_a} q_b + \dots = -0.2816 q_b + \dots \tag{3.14}$$

$$k = a, j = b \quad q_b = \frac{k_I m_a}{k_{2b} m_a - k_{2a} m_b} q_a + \dots = 0.6200 q_a + \dots \tag{3.15}$$

The form of these two equations indicates that the relationship between the behaviors of two oscillators is affected by the linear properties of the oscillators and

the coupling between them. When $k = b$, the equation describes the amplitude of one of the low-frequency cantilevers caused by the amplitude of one of the high-frequency cantilevers. When k is equal to a , the equation describes the amplitude of one of the high-frequency cantilevers caused by the amplitude of one of the low-frequency cantilevers. When the calculated values are negative, this indicates that the oscillators will be half a period out of phase with the oscillator at the center of the localization.

In order to produce an analytical amplitude profile to compare with the simulation results, an amplitude value is selected for the center of the localization. This value is selected based on the maximum amplitude values observed in the simulation results. To produce this profile, equation (3.14) is used to determine the amplitudes of $x_{\pm 1}$. The amplitude values for $x_{\pm 2}$ are calculated by using equation (3.15). By repeatedly alternating the equations in this fashion, an analytical profile is produced for this system. In figure 3.2(a), the amplitude profile for a region close to the center of the localization is compared with the simulation results.

Restricted Normal Mode Approach

The second approach employed to analytically determine the amplitude profile is the restricted normal mode approach. In this approach, it is assumed that the two oscillators behave in a harmonic fashion with the same frequency but different amplitudes, as shown in equation (3.16). These assumed forms are substituted into the equations obtained from (3.5) for $j = a$ and $j = b$. The resulting equations are then combined to eliminate the frequency variable and the higher order harmonics

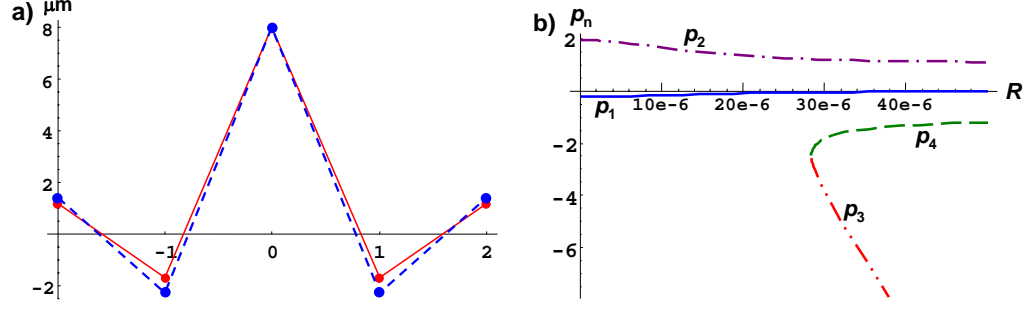


Figure 3.2: Results of analytical studies: (a) a comparison of simulation profile (solid line) and the profile obtained by using the method of multiple scales (dashed line) and (b) the four roots of the polynomial from restricted normal mode approach.

are neglected, as discussed in appendix A. The equation produced is further modified by defining each of the two amplitude variables as the product of a variable, R , and a harmonic function of a second variable, θ , as shown in equation (3.17). The square of the variable R is proportional to the total energy level of the oscillator pair. The ratio of these amplitudes is defined by an additional variable, p . After incorporating these definitions and variables, the resulting equation is a fourth-order polynomial in p . This equation is presented as (3.18).

$$x_a = A \cos(\omega t), \quad x_b = B \cos(\omega t) \quad (3.16)$$

$$A = R \sin(\theta), \quad B = R \cos(\theta), \quad p = \frac{A}{B} = \tan(\theta) \quad (3.17)$$

$$p(1+p^2)(k_{2a}m_b - k_{2b}m_a) - \frac{3}{4}R^2k_4p(m_a - m_b p^2) - k_I(1+p^2)[2m_a p(1-p) + m_b(1-2p)] = 0 \quad (3.18)$$

The four roots of this polynomial are functions of R and the system parameters. The value of R can be selected to determine the nonlinear vibration modes of the two oscillators for different amplitude values. For a range of values of R , the four roots are calculated, as shown in figure 3.2(b). The arctangent of the p values provides θ values that are then used to calculate the amplitudes of A and B . A plot of the corresponding values of amplitude A versus amplitude B for a range of R values is presented in figure A.1 in appendix A. In figure 3.2(b), only two roots, p_1 and p_2 , exist for the range of R values that correspond to the amplitude values observed in the simulations. The root p_1 , which is represented by the solid line, corresponds to the amplitude ratio r_1 and root p_2 , which is represented by the dash-dot-dash line, corresponds to the inverse of the amplitude ratio r_2 . The roots are selected in this manner to produce the ILM profile corresponding to the minimum energy state. When the center amplitude is selected to agree with the simulation results, an amplitude profile can be produced. A partial profile produced by this approach around the center of the localization is shown along with the simulation result in figure 3.3(a).

Real-Variable and Complex-Variable Invariant-Manifold Approach

The third approach employed to calculate the amplitude profiles corresponding to an ILM in the micro-cantilever array is the two variations of the invariant-manifold approach. The full procedure for implementing these analyses can be found in the literature [56]. One of the strengths of this analysis is that the full multi-degree of freedom system can be studied and the simplification is not necessary. The

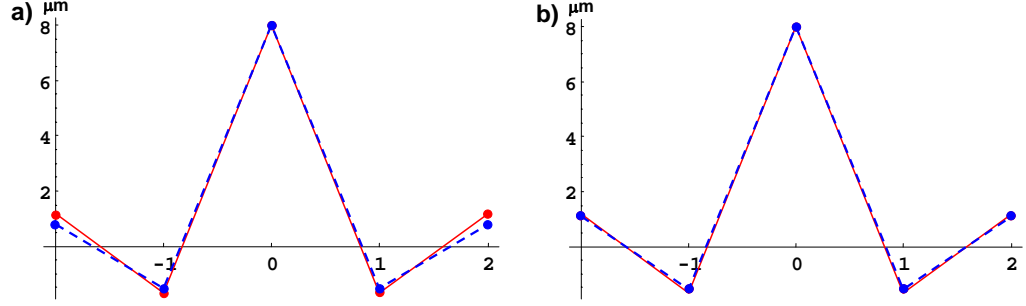


Figure 3.3: Results of analytical studies: (a) a comparison of simulated profile (solid line) and analytical profile from restricted normal mode approach (dashed line) and (b) a comparison of simulated profile (solid line) and analytical profile from modified real-variable invariant-manifold approach (dashed line).

goal here is to determine the two-dimensional invariant-manifolds that define the system's normal modes. The two variations of the approach considered here are the real-variable invariant-manifold approach and the complex-variable invariant-manifold approach. The complex-variable approach differs from the real-variable approach by using a single first-order complex-value equation rather than two first-order real-value equations for each oscillator. When the complex-variable approach is applied to the current system, the invariant-manifold given by equation (3.19) is obtained. When converted to real-variable form, equations (3.20) and (3.21) are produced.

$$\begin{aligned}
 h_j = & \frac{g_{1,j,k}}{2\omega_j(3\omega_k - \omega_j)} \zeta_k^3 + \frac{3g_{1,j,k}}{2\omega_j(\omega_k - \omega_j)} \zeta_k^2 \bar{\zeta}_k \\
 & - \frac{3g_{1,j,k}}{2\omega_j(\omega_k + \omega_j)} \zeta_k \bar{\zeta}_k^2 - \frac{g_{1,j,k}}{2\omega_j(3\omega_k + \omega_j)} \bar{\zeta}_k^3
 \end{aligned} \tag{3.19}$$

$$q_j = \frac{(7\omega_k^2 - \omega_j^2) g_{1,j,k}}{(9\omega_k^2 - \omega_j^2)(\omega_k^2 - \omega_j^2)} q_k^3 + \frac{6 g_{1,j,k}}{(9\omega_k^2 - \omega_j^2)(\omega_k^2 - \omega_j^2)} q_k p_k^2 + \dots \quad (3.20)$$

$$p_j = \frac{6 g_{1,j,k}}{(9\omega_k^2 - \omega_j^2)(\omega_k^2 - \omega_j^2)} p_k^3 + \frac{3(3\omega_k^2 - \omega_j^2) g_{1,j,k}}{(9\omega_k^2 - \omega_j^2)(\omega_k^2 - \omega_j^2)} q_k^2 p_k + \dots \quad (3.21)$$

When the results of the complex-variable approach are converted to real-variable form, the resulting equations should be identical to the results of the real-variable invariant-manifold approach, if the linear coupling terms are not present. For this particular system, due to the difficulty of uncoupling the oscillators, the results differ. Following the real-variable invariant-manifold approach, equations (3.22) and (3.23) are produced.

$$q_j = \frac{[7(g_{2,k,k} + \omega_k^2) - \omega_j^2] g_{1,j,k}}{[9(g_{2,k,k} + \omega_k^2) - \omega_j^2](g_{2,k,k} + \omega_k^2 - \omega_j^2)} q_k^3 + \frac{6 g_{1,j,k}}{[9(g_{2,k,k} + \omega_k^2) - \omega_j^2](g_{2,k,k} + \omega_k^2 - \omega_j^2)} q_k p_k^2 + \dots \quad (3.22)$$

$$p_j = \frac{6 g_{1,j,k}}{[9(g_{2,k,k} + \omega_k^2) - \omega_j^2](\omega_k^2 - \omega_j^2)} p_k^3 + \frac{3[3(g_{2,k,k} + \omega_k^2) - \omega_j^2] g_{1,j,k}}{[9(g_{2,k,k} + \omega_k^2) - \omega_j^2](\omega_k^2 - \omega_j^2)} q_k^2 p_k + \dots \quad (3.23)$$

While the coefficients of the complex-variable analysis are not influenced by the linear coupling term, the coefficients of the real-variable study are affected by its presence. Additionally, due to the absence of nonlinear coupling within this system, the variable $g_{1,j,k}$, which is present in all of the manifold's coefficients for both the real-variable and complex-variable methods, is equal to zero for $j \neq k$. As a result, it becomes clear that the real-variable and complex-variable invariant-manifold approaches are not effective for systems that only have linear coupling.

To accommodate the linear coupling of the system, a variation of the real-variable invariant-manifold approach is proposed.

The real-variable invariant-manifold approach is modified to study a nonlinear system with dominant linear behavior. The main modification is the inclusion of linear terms in the assumed form of the manifold equations as shown in equation (3.24). To accommodate the nonlinear stiffness of the oscillators, a cubic term is included in the manifold's displacement equation. Due to the weak nature of the nonlinear term, the manifold's velocity equation includes only linear terms.

$$Q_j = \sum_k \left(\Gamma_{1,j,k} q_k + \Gamma_{2,j,k} q_k^3 \right), \quad P_j = \sum_k \left(\Gamma_{3,j,k} p_k \right) \quad (3.24)$$

$$\frac{\partial Q_j}{\partial q_k} p_k + \frac{\partial Q_j}{\partial p_k} \left(-\omega_k^2 q_k - G_k \right) = P_j \quad (3.25)$$

$$\frac{\partial P_j}{\partial q_k} p_k + \frac{\partial P_j}{\partial p_k} \left(-\omega_k^2 q_k - G_k \right) = -\omega_j^2 Q_j - G_j \quad (3.26)$$

The manifold equations are then substituted into the equations of motion given by equations (3.25) and (3.26), to solve for the coefficients $\Gamma_{1,j,k}$, $\Gamma_{2,j,k}$, and $\Gamma_{3,j,k}$. The definitions of these coefficients are listed in equations (3.27) and (3.28). It follows that the displacement equation can describe the amplitude of one of the low-frequency oscillators as a function of the amplitude of the adjacent high-frequency cantilever as well as the opposite case.

$$\Gamma_{1,j,k} = \Gamma_{3,j,k} = \frac{g_{2,j,k}}{g_{2,k,k} + \omega_k^2 - \omega_j^2} \quad (3.27)$$

$$\Gamma_{2,j,k} = \frac{g_{1,k,k}}{\omega_j^2} \frac{g_{2,j,k}}{g_{2,k,k} + \omega_k^2 - \omega_j^2} - \frac{g_{1,j,k}}{\omega_j^2} \quad (3.28)$$

$k = j \pm 1$, even:

$$\begin{aligned} Q_j &= \frac{k_I m_b}{k_{2a} m_b - k_{2b} m_a - 2k_I m_a} q_k + \frac{(k_4 k_I m_a / k_{2a})}{k_{2a} m_b - k_{2b} m_a - 2k_I m_a} q_k^3 + \dots \\ &= -0.1738 q_k - 3.1576 \times 10^8 q_k^3 + \dots \end{aligned} \quad (3.29)$$

$k = j \pm 1$, odd:

$$\begin{aligned} Q_j &= \frac{k_I m_a}{k_{2b} m_a - k_{2a} m_b - 2k_I m_b} q_k + \frac{(k_4 k_I m_b / k_{2b})}{k_{2b} m_a - k_{2a} m_b - 2k_I m_b} q_k^3 + \dots \\ &= 0.7096 q_k + 9.1310 \times 10^8 q_k^3 + \dots \end{aligned} \quad (3.30)$$

The description of the amplitude of one of the low-frequency cantilevers as a function of the amplitude of one of the high-frequency cantilevers is given by (3.29). This corresponds to $x_{\pm 1}$ being influenced by x_0 . For the opposite case, the amplitude of a high-frequency cantilever as a function of the amplitude of a neighboring low-frequency cantilever is described by equation (3.30). For the particular silicon nitride micro-cantilever array studied by Sato et al. [49], numerical values calculated with this and the other methods are presented in Table 3.1 and Table 3.2.

Through the modification of the real-variable invariant-manifold approach, it is possible to create an amplitude profile for a nonlinear array with the dominant linear behavior. A partial amplitude profile produced by this analysis (dashed line) is compared with the simulation profile (solid line) in figure 3.3(b), and good agreement is seen. Although this method does not strictly follow the real-variable invariant-manifold approach, the equations produced do comply with the requirements of the manifold equations given as (3.31).

$$\begin{aligned}
q_k = p_k = 0 & & Q_j(0, 0) = 0 & & P_j(0, 0) = 0 \\
j = k & & Q_k(q_k, p_k) = q_k & & P_k(q_k, p_k) = p_k
\end{aligned}
\tag{3.31}$$

3.1.3 Floquet Theory

By using Floquet theory, the amplitude ratios predicted by the various methods are examined to determine if they produce bounded, periodic solutions. To accomplish this, the oscillators are simulated after initializing them with displacement values corresponding to the amplitude values obtained through the different analysis methods and zero velocities. Results that appear to yield periodic solutions are examined by using Floquet theory to determine if nearby trajectories will converge to these solutions. Floquet theory is applied in the manner described in the text [75] by following the evolution of the linearization and the full nonlinear system over one period of the motion. The Floquet multipliers are calculated as the eigenvalues of the corresponding monodromy matrix. Floquet multipliers with magnitudes greater than one are used to identify unstable periodic solutions.

3.2 Analysis Results

The amplitude ratios r_1 and r_2 produced through this work are presented in Table 3.1 and Table 3.2, respectively. The data in the first row of the tables corresponds to results obtained from the simulations with the linear relations and the second row of the tables corresponds to results obtained from the simulations with the nonlinear relations. The linear relations describe the amplitude ratios between adjacent

Table 3.1: Amplitude ratio r_1 from simulation and analyses.

Method	r_1	Difference	Difference
	Value	Linear	Nonlinear
Simulation, Linear Relation	-0.21	—	—
Simulation, Nonlinear Relation	-0.2060	—	—
Method of Multiple Scales Approach	-0.2816	25%	27%
Restricted Normal Modes Approach	-0.1910	10%	7.9%
Invariant-Manifold Approach	No Soln	—	—
Modified Real-Variable			
Invariant-Manifold Approach	-0.1940	8.2%	6.2%

oscillators of the average normalized profile. The nonlinear relations describe the displacement relationships between adjacent oscillators fit to data over many periods of oscillations with both linear and cubic terms. The remaining rows contain data from the different analyses. The second column of each table contains the amplitude ratio values. The values in the remaining columns are obtained by comparing the calculated values with the values from the simulations from both the linear and nonlinear relations.

3.2.1 Method of Multiple Scales Approach

After examining the analytical profile as well as the numerical coefficients of the two equations, amplitude ratio values are produced. These values and comparisons with the linear and nonlinear relations applied to the simulations are presented in the

Table 3.2: Amplitude ratio r_2 from simulation and analyses.

Method	r_2	Difference	Difference
	Value	Linear	Nonlinear
Simulation, Linear Relation	-0.70	—	—
Simulation, Nonlinear Relation	-0.6679	—	—
Method of Multiple Scales Approach	-0.6200	13%	7.7%
Restricted Normal Modes Approach	-0.5190	35%	29%
Invariant-Manifold Approach	No Soln	—	—
Modified Real-Variable			
Invariant-Manifold Approach	-0.7118	1.7%	6.2%

third rows of Table 3.1 and Table 3.2. Despite the relatively small difference between the displacement values as shown in figure 3.2(a), a simulation of the simplified oscillator pair and subsequent stability analysis by using Floquet theory indicates that the results obtained by using the method of multiple scales are not sufficient to predict the characteristics of the localization phenomenon.

3.2.2 Restricted Normal Mode Approach

By using the equations that produced figure 3.2(b), an appropriate R value can be identified for producing an amplitude value for B that corresponds to the amplitude of x_0 from the simulation results. After this is done, the value of p_1 is equal to the amplitude ratio r_1 . The value of A from the first relation is matched by using p_2 with a new value of R . The second amplitude ratio r_2 is equal to the inverse

of the value of p_2 . The results of this method are presented in the fourth rows of Table 3.1 and Table 3.2. Simulations of the simplified system and stability analysis by using Floquet theory confirm that the first amplitude ratio produced by the restricted normal mode analysis results in a bounded, periodic solution. However, for the second amplitude ratio, the difference between the calculated values and those observed in the simulations is found to be too large. In order to further study the results of the different methods, amplitude profiles are produced and used to initialize the arrays for numerical simulations. This is done by setting the initial displacements with the values from the amplitude profile and setting the initial velocities to zero. The phase of the excitation sinusoid is set to synchronize with the oscillations and the simulation is conducted. Although the equations of motion are non-dimensionalized with respect to time and length, no special numerical schemes are employed to account for numerical damping. When this method is used in an attempt to initiate an ILM within an array, the ILM does not synchronize with the excitation and decays very quickly. This failure to produce a pinned ILM is shown in figure 3.4(a).

3.2.3 Invariant-Manifold Approaches

By again selecting a displacement value for the center of the localization, corresponding to the amplitude obtained from the simulation, equations (3.29) and (3.30) are used to predict the amplitude ratios when an ILM is present. These amplitude ratios are listed in the sixth rows of Table 3.1 and Table 3.2. Simulation results

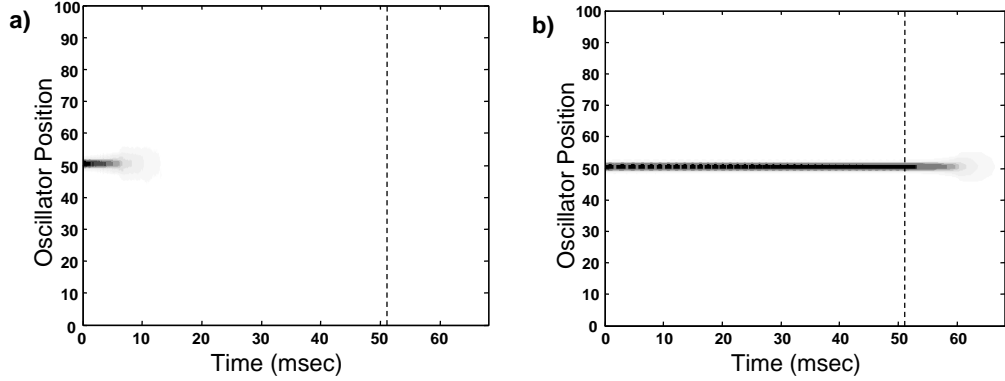


Figure 3.4: Localization simulations: (a) failure to create an ILM with amplitude ratios from the restricted normal mode approach and (b) the successful creation of an ILM with amplitude ratios from the modified real-variable invariant-manifold approach.

and Floquet multipliers indicate that a bounded, periodic solution is produced by using the first amplitude ratio determined from this variation of the real-variable invariant-manifold approach. By using equations (3.29) and (3.30), it is possible to initiate an ILM within an array of coupled nonlinear oscillator pairs. A pinned ILM can be produced from these amplitude ratios as shown in figure 3.4(b). Among the different approaches examined in an attempt to analytically produce the characteristic profile of an ILM, the modified real-variable invariant-manifold approach is the most successful. This method produces nonlinear equations that can be used to analytically create an amplitude profile for an ILM.

To further study the effectiveness of this method for predicting the amplitude profile of an ILM, it has been applied to arrays with different parameter values. The parameter values corresponding to the micro-cantilever array are varied and

the coefficients of the amplitude equations are recalculated. The array system is then simulated with these new parameter values and initial displacements calculated with the new amplitude equations. After correctly identifying the excitation frequency necessary to maintain the localization, ILMs have been successfully placed within these different systems. This is done by first altering only one of the system parameters at a time, both by increasing and decreasing their values. After gaining insight into the relationship between changes to the parameter values and the excitation frequency, all of the mass and stiffness parameter values are varied simultaneously to simulate a completely different array. The magnitude that the values are varied is kept relatively small. The size of these changes are kept small in order to ensure that the excitation level and center oscillator displacement do not need to be changed and that only a single parameter, the excitation frequency, must be modified. The successful application to these varied systems further supports this modified method. It also suggests that the form of these types of localization events can be predicted and that the localizations can be artificially initiated in this manner.

Regarding the effects of noise on this system, simulations have been conducted by adding a small-magnitude random signal with a uniform distribution to the excitation. With a noise level at five percent of the amplitude of the sinusoidal signal, ILMs could still be initiated and sustained with a ninety percent success rate. Additional studies have also examined the effects of deviation from perfect periodicity within the array on the localizations. Simulations suggest that the localization are very sensitive to non-periodicity of the oscillators with a random variation of the

mass or stiffness limiting the success rate for initiating ILMs to less than ten percent. Within experimental systems, the non-uniformity of the resonance frequencies that results from these variations can be accommodated with by tuning the resonators with the addition of a DC bias.

The success of the modified real-variable invariant-manifold is thought to be due to the linear coupling between the oscillators and the dominant linear behavior observed within the array. Due to the range of motion of the oscillators, the contributions of the cubic terms are negligible for most oscillators within the array when compared to the contributions of the linear terms. The nonlinear vibration modes obtained from this method are presented in Figure 3.5(a) and Figure 3.5(b) for the maximum ranges of motion experienced at a localization. The solid line represents the nonlinear vibration mode while the dashed line corresponds to only the linear term. The close-up views within these figures indicate that nonlinear behavior is prominent only for the largest amplitude values experienced by the oscillator at the center of the ILM.

This results in circumstances that are analogous to the case of a localization resulting from a defect within an array of coupled, linear oscillators. When the amplitude of an oscillator within the system examined grows large enough, its behavior becomes nonlinear distinguishing it from the other oscillators within the array. Without the nonlinearity, this type of localization phenomenon cannot occur.

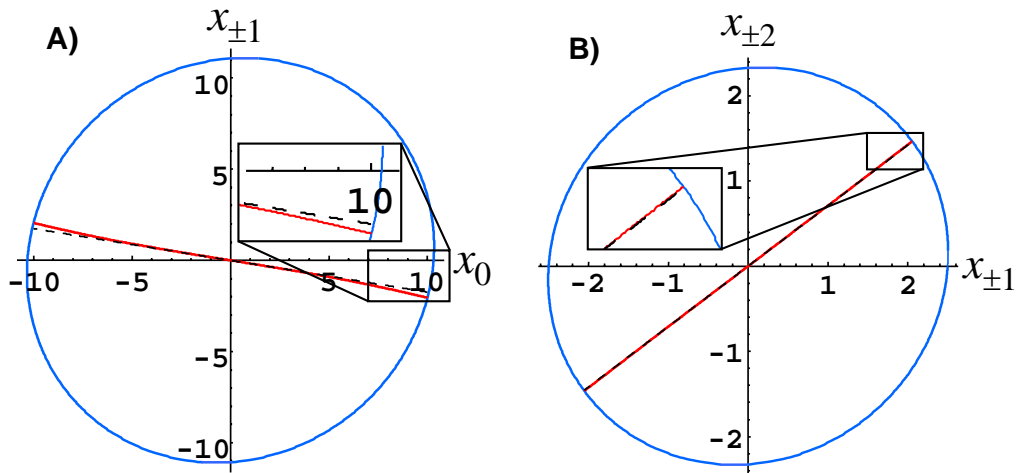


Figure 3.5: Nonlinear vibration modes: (a) the nonlinear vibration modes relating motion of x_0 and $x_{\pm 1}$ for the range of motion experienced during an ILM and (b) the nonlinear vibration modes relating motion of $x_{\pm 1}$ and $x_{\pm 2}$ for the range of motion experienced during an ILM. The nonlinear vibration modes are represented by the solid curves and the dashed line corresponds to only the linear term. The units are in micrometers.

3.3 Effects of Internal Resonance

3.3.1 One-to-One Internal Resonance

A number of methods explored to calculate nonlinear normal modes produced results that are sensitive to cases of internal resonance. Both the Method of Multiple Scales Approach and the Invariant-Manifold Approach produced equations that would result in a singularity when either one-to-one or three-to-one internal resonance conditions existed. Here, these conditions are investigated to identify how internal resonance affects the behavior of ILMs. In each case the system's parameters are modified so that every pair of oscillators within the array experiences the internal resonance conditions.

The first condition to be examined is that of one-to-one internal resonance. In the case of a system of coupled oscillators, this would produce a mono-element array which is an array of identical oscillators. A di-element array is an array consisting of two types of oscillators that are arranged in a periodic fashion. Within the literature [49], the selection of a di-element array for use with a uniform excitation method is discussed and related to the dispersion curves associated with the arrays.

Dispersion curves provide both spatial and temporal information about wave propagation within a discrete structure. Dispersion curves are calculated by assuming that the displacement of the elements in the lattice, or in this case the two types of oscillators, can be described by using equations (3.32) and (3.33). Within this equation, x_a and x_b are the displacements of the oscillators and they are functions of the oscillator number n and time t . The oscillation amplitudes are represented

by X_a and X_b , a is the oscillator spacing, ω is the frequency, and k is the wave number. The wave number is defined by equation 3.34, where λ is the wavelength of the vibrations. These equations are substituted into the linearized, conservative equations of motion and written in matrix form, as shown by equation (3.35). To ensure a non-trivial solution for the vector of oscillation amplitudes, the determinant of the matrix is set equal to zero. The resulting equation is then solved for the frequency parameter ω and plotted as a function of the wave number k to produce the dispersion curves.

$$x_a(n, t) = X_a e^{i(n a k - \omega t)} \quad (3.32)$$

$$x_b(n, t) = X_b e^{i(n a k - \omega t)} \quad (3.33)$$

$$k = \frac{2\pi}{\lambda} \quad (3.34)$$

$$\begin{bmatrix} m_a \omega^2 - k_{2a} - 2k_I & k_I (1 + e^{-i a k}) \\ k_I (1 + e^{-i a k}) & m_b \omega^2 - k_{2b} - 2k_I \end{bmatrix} \cdot \begin{Bmatrix} X_a \\ X_b \end{Bmatrix} = \begin{Bmatrix} 0 \\ 0 \end{Bmatrix} \quad (3.35)$$

When compared with the mono-element array, the use of a di-element array causes the dispersion curve to be folded back, resulting in the highest frequency vibrational mode being at the zone center, as shown in Fig. 3.6. By folding back the dispersion curve, a stop band is produced and, for hard anharmonicity, ILMs will be created at the zone center at slightly higher frequencies. For the case of one-to-one internal resonance within a system that is being uniformly excited, the absence

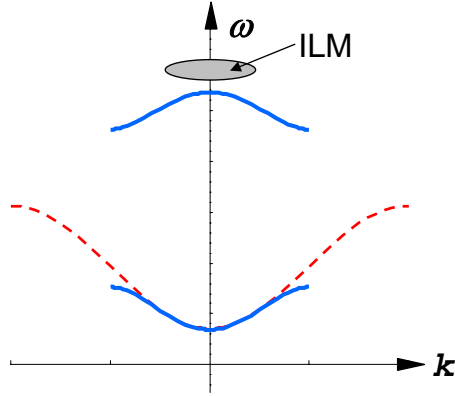


Figure 3.6: Dispersion curves for mono-element (dashed) and di-element (solid) arrays. The horizontal axis corresponds to the wave number and the vertical axis corresponds to the frequency.

of the higher frequency vibrational mode allows the energy to disperse throughout the array and inhibits the formation of these ILMs. While it is possible to study localization in a mono-element array through the use of non-uniform excitation methods, within this type of array, localizations will not be produced and these conditions are not investigated here.

3.3.2 Three-to-One Internal Resonance

The second condition that would result in a singularity within the equations derived with both the Method of Multiple Scales Approach and the Invariant-Manifold Approach is a three-to-one internal resonance. Under this condition, the resonance frequencies of the two cantilever structures that make up the di-element array have a relationship such that the frequency value of one is approximately equal to three times the frequency value of the other; that is, $\omega_b \approx 3\omega_a$. In order to study the

Table 3.3: Parameter values for three-to-one internal resonance condition.

Parameter	Value
m_a	6.0×10^{-13} kg
m_b	2.0×10^{-13} kg
k_{2a}	0.1 N/m
k_{2b}	0.3 N/m

behavior of ILMs within a system where these conditions exist, the mass and stiffness values associated with oscillators are modified. All other parameter values and procedures remain unchanged. The new values, given in table 3.3, are selected to be of the same orders of magnitude as the previous values while producing the desired three-to-one internal resonance condition. As a result of the changes to the values of the linear stiffness parameters, the relative strength of the nonlinear stiffness is maintained with little change. Due to the change in the stiffness of the low frequency oscillator, the value of the force produced by the nonlinear term for the oscillators adjacent to the center of the ILM is increased to about two percent of the force value produced by the linear term. The force ratios at the center of the ILM and away from the ILM are not significantly affected.

With the new parameter values selected, the resulting dispersion curves are examined to ensure that the formation of the localization events is able to occur. Although the dispersion curves, shown in figure 3.7, reveal the necessary di-element

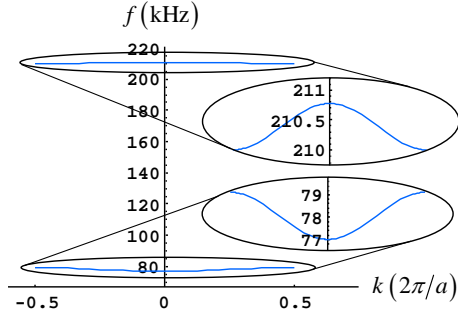


Figure 3.7: Dispersion curve for di-element array with three-to-one internal resonance.

form, the new parameter values increase the range of the frequency band, the difference between the highest and lowest frequencies of the array, from 23.3 kHz to more than 130 kHz. In order to study how this large frequency band affects the behavior of the ILMs and their characteristic amplitude profile, simulations are conducted for an array of fifty oscillator pairs by using the new parameter values.

Numerical Simulations

Simulations conducted with the new parameter values are found to successfully generate localization events within the array. The use of the new parameter values is found to result in conditions that are much more conducive to the formation of ILMs. While numerous attempts are necessary in order to produce a simulation where a locked ILM is observed using the original parameter values, multiple locked ILMs are produced in most simulation with the new parameter values. As a result of the greater quantity of locked ILMs, more ILMs becoming synchronized with the excitation to become pinned ILMs. Representative results of a simulation conducted

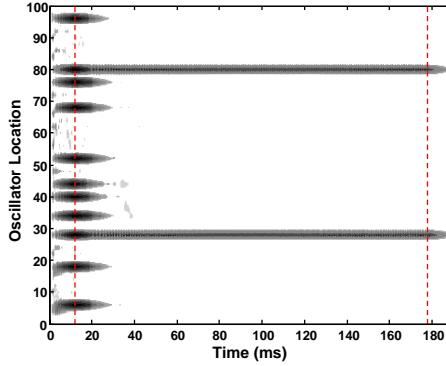


Figure 3.8: ILM simulation results for a di-element array with three-to-one internal resonance.

by using the new parameter values is shown in figure 3.8. In this simulation, eleven locked ILMs are produced and two synchronize with the constant frequency excitation to become pinned ILMs. This simulation differs slightly from the previous simulation in that the second phase of excitation is increased from 5000 periods of oscillation to 35000 periods in order to allow more time for the transient oscillations sufficient time to decay.

In order to determine whether this increased number of simulated ILMs is a characteristic of the three-to-one internal resonance condition, simulations are conducted by using the parameter values that produce near three-to-one internal resonance conditions. By changing the values of the mass and stiffness parameters, the resonance frequency of one type of oscillator is set to be 3.1 times the resonance frequency of the other type of oscillator. These parameter values are used and simulations are performed. The results of the simulations show the same increased level of the production of locked ILMs that was seen for the three-to-one internal resonance conditions. This suggests that the difference between the results of the

simulations conducted with the original parameter values from table 1.3 in chapter one and the simulations performed with the values listed in table 3.3 is a result of the drastic increase in the frequency band of the array and not due to any type of resonance phenomenon.

To further study the effects of the three-to-one internal resonance condition on the localization events, the amplitude profile of the pinned ILM is examined. This is done by selecting the data for ten thousand periods of oscillation from just before the end of the second excitation phase for the oscillators in the direct vicinity of the oscillator at the center of the pinned ILM, henceforth to be referred to as x_0 . To ensure the quality of the results a number of the profiles are removed from the set; 6.4% for the original parameters and 8.3% for the three-to-one internal resonance condition. These profiles correspond to instances where the displacement at the center of the localization has a magnitude less than $0.1 \mu\text{m}$, a condition that has been found to be problematic when normalizing the profiles. The displacement values that make up the remaining profiles are normalized by the displacement of x_0 . After normalizing the displacement profiles, an average profile is calculated. Additionally, the standard deviation of the profile is also calculated in order to determine how well the average represents the behavior of the ILM. For the original parameter values, $x_{\pm 1}$ and $x_{\pm 2}$ have average standard deviation values that are 0.74% and 2.5% of the average values, respectively. With the parameter values necessary to produce three-to-one internal resonance conditions, the average standard deviation values for $x_{\pm 1}$ and $x_{\pm 2}$ are 4.3% and 68% of the average values, respectively. Most of the standard deviation values are only a small percent of the average value. The large percentage

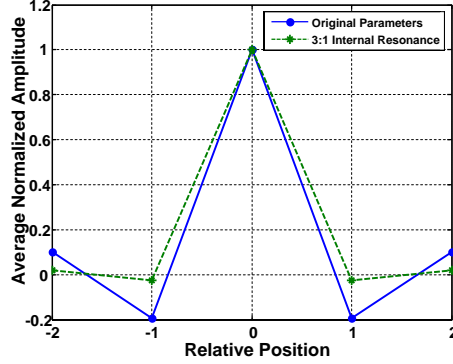


Figure 3.9: Comparison of the ILM profile for the original parameter values (solid) with the profile for three-to-one internal resonance conditions (dashed).

associated with $x_{\pm 2}$ for the three-to-one internal resonance condition results from the average normalized amplitude value being equal to only 0.019. The standard deviations are relatively small and this would indicate the average values provide an accurate representation of the amplitudes of the oscillators when an ILM occurs.

The average normalized displacement profiles for these two conditions are presented in figure 3.9. The symmetry of the amplitude profiles in the figure is found to be a characteristic of the ILMs and it is taken into account when analyzing their behavior. In addition to the increased quantity of localizations, the comparison of the amplitude profiles shows that when three-to-one internal resonance conditions exist, the amplitudes of $x_{\pm 1}$ are considerably smaller, indicating that the energy is more concentrated. The difference in the amplitude profiles is further explored by calculating the ratios of the amplitudes between adjacent oscillators. The amplitude ratios are listed in table 3.4. The first column of values corresponds to the original parameter values and the second column of values corresponds to the three-to-one internal resonance conditions. In order to determine if the three-to-one internal res-

Table 3.4: Amplitude ratios.

Ratio	Original System	3:1 Conditions	Near 3:1
r_1	-0.192	-0.026	-0.024
r_2	-0.518	-0.731	-0.711

onance condition that produces this high level of energy concentration, amplitude ratio values are also calculated for near three-to-one internal resonance conditions and listed as the final column in table 3.4. These amplitude ratio values are very similar to the previous column of values, again suggesting that the large frequency band is responsible for the drastic change in performance from the original system.

By investigating an array where the three-to-one internal resonance condition exists with the aid of numerical simulations, insight has been gained into the behavior of ILMs under these conditions. The effects of these internal resonance conditions on the amplitude profile of the ILM have also been investigated. With the aid of the amplitude profiles and amplitude ratios obtained from the numerical investigation, analytical studies are conducted to further examine the effects of three-to-one internal resonance conditions on the nonlinear localization phenomenon known as intrinsic localized modes.

Analytical Studies

In order to continue studying the manner in which three-to-one internal resonance conditions affect the behavior of ILMs, an analytical investigation is conducted. The computational details for producing the nonlinear modes by using the Method of Multiple Scales Approach [56, 75] and the Invariant Manifold Approach [56] need to be modified in the presence of internal resonance. However, with either the Restricted Normal Mode Approach [44] or a linearized version of the Invariant Manifold Approach [80], the computational approach to produce the nonlinear modes remains the same for the cases with and without the internal resonance. By using the results obtained with these methods from the previous section, the new parameter values from table 3.3 are substituted into the equations in order to obtain results for three-to-one internal resonance conditions.

Before applying the Restricted Normal Mode Approach, it is necessary to use the model simplification to reduce the system down to a single pair of coupled oscillators. The damping and excitation terms are also omitted to produce a conservative model. The restricted normal mode approach is applied in the manner described by (3.16), (3.17), and (3.18).

The four roots of (3.18) for the new parameter values are plotted in figure 3.10 for a range of R values. A close-up view of the root represented by the solid curve is shown in the insert. The values obtained for the roots p_n of the polynomial are used to calculate values for the parameters θ_n which are then used to calculate values for the amplitudes A_n and B_n . For the oscillation amplitudes observed in the

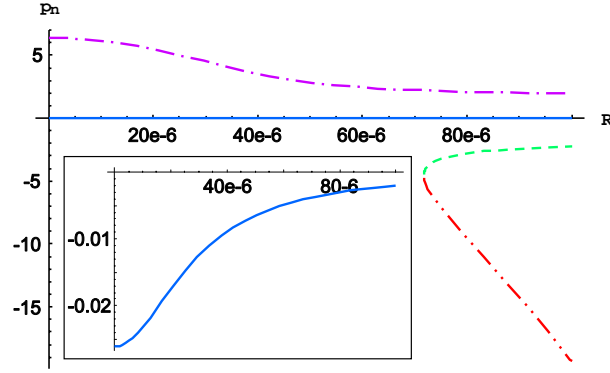


Figure 3.10: Four roots of the polynomial of the Restricted Normal Mode Approach. The roots are plotted as a function of the parameter R with the different styles: dash, dot-dash, and dot-dot-dash. The fourth root to the polynomial, which is represented by the solid curve, is shown in the insert.

numerical simulations, the values of R will be less than 10×10^{-6} , eliminating two of the roots. The two remaining roots are used to construct an amplitude profile. This is done by first selecting an amplitude value for x_0 . Based on the simulation results, an amplitude of $8 \mu\text{m}$ is used. By using the root represented in figure 3.10 by the solid curve, a value of $-0.194 \mu\text{m}$ is calculated for $x_{\pm 1}$. The root represented by the dash-dot curve is used to calculate an amplitude value of $0.0303 \mu\text{m}$ for $x_{\pm 2}$. As before, the order in which the two roots are selected is decided so as to produce the amplitude profile that corresponds to the lower energy state. These amplitude values are compared with the results obtained from the simulation in figure 3.11. The solid curve corresponds to the results of the simulation and the results of the Restricted Normal Mode Approach are represented by the dashed curve.

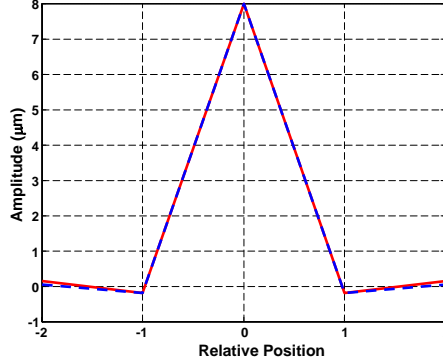


Figure 3.11: Comparison of results from the Restricted Normal Mode Approach (dashed) with simulation results (solid).

Before applying the Linearized Invariant-Manifold Approach, the model of this system, (1.12) and (1.13), is required in a general form. The general form, shown as (3.5), provides a single equation able to describe the behavior of both styles of oscillators depending on the value of the index j . With the equations of motion rewritten in the general form, the linearized form of the Invariant-Manifold Approach is performed. The values of the system parameters are substituted into the displacement manifold equation and the amplitude values corresponding to the oscillation profile of an ILM are calculated. With a value of $8 \mu\text{m}$ selected for the amplitude of x_0 , equation (3.29) is used and a value of $-0.400 \mu\text{m}$ is calculated for $x_{\pm 1}$. Similarly, equation (3.30) is used and a value of $-0.0385 \mu\text{m}$ is calculated for $x_{\pm 2}$. These amplitude values are compared with the average profile obtained from the simulation in figure 3.12. The solid curve corresponds to the simulation profile and the profile obtained by using the linearized Invariant-Manifold Approach is represented by the dashed curve.

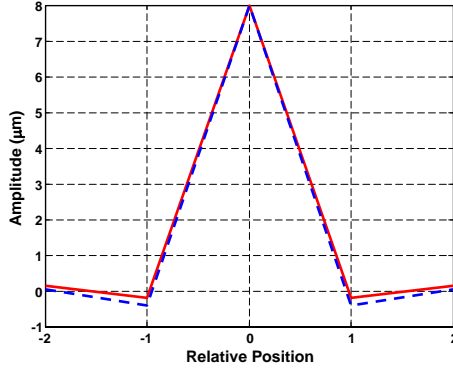


Figure 3.12: Comparison of results from linearized Invariant-Manifold Approach (dashed) with simulation results (solid).

Floquet Theory

In order to investigate the stability of the results obtained from the Restricted Normal Mode Approach and the linearized Invariant-Manifold Approach, Floquet Theory is employed. To perform this study, the oscillators are simulated after initializing them with zero velocities and displacement values corresponding to the amplitude values obtained from the two analytical methods. The periodic oscillations are examined by using Floquet Theory to determine if nearby trajectories will converge to these solutions. Floquet multipliers with values greater than one are used to identify unstable periodic solutions.

3.3.3 Results

While studying Intrinsic Localized Modes (ILMs), various methods to determine nonlinear normal modes were employed in an attempt to analytically determine the amplitude profile associated with the pinned ILMs. The resulting equations pro-

duced by particular computational applications of multiple methods were found to be sensitive to one-to-one or three-to-one internal resonance conditions. An investigation is conducted to examine how these internal resonance conditions affect the behavior of ILMs. This investigation is conducted with the aid of analytical and numerical methods.

The first internal resonance conditions examined is that of one-to-one internal resonance. Within an array of coupled oscillators, this conditions produces a mono-element array and, based upon the desire to excite the array uniformly, this configuration is not conducive to the formation of ILMs. This is verified by examining the dispersion curves associated with both array configurations. Based upon this information, the one-to-one internal resonance condition is not studied any further and attention is directed toward the three-to-one internal resonance condition.

In considering the three-to-one internal resonance condition, the dispersion curves are examined to verify that ILMs will form. While the structure of the curves indicate that ILMs will exist within the system, the new resonance frequencies cause the array's frequency band to be increased from 23.3 kHz to more than 130 kHz. In order to study the behavior of ILMs under these new conditions, numerical simulations are performed for an array of fifty oscillator pairs. These simulations are found to produce a greater quantity of locked and pinned ILMs than with the original system parameters. This is found to be due to the change in the resonance frequencies and not a unique result of the resonance conditions as similar results are obtained for near resonance conditions. This may be useful knowledge when developing applications for this phenomenon as it suggests that it may be easier to

Table 3.5: Amplitude ratios for three-to-one internal resonance conditions.

Ratio	Simulation	RNM Approach	LIM Approach
r_1	-0.026	-0.024	-0.050
r_2	-0.731	-0.156	-0.096

produce ILMs in arrays with wide frequency bands. Additionally, it is found that under the new conditions, the amplitude profile of the ILM shows a higher degree of energy concentration with the amplitude values decaying much more rapidly when moving out from the center of the pinned ILM. Again, near resonance conditions produce similar results suggesting that this is a result of the wide frequency band and it is not unique to the resonance conditions. This relationship between energy concentration and the frequency band may also be beneficial when utilizing this phenomenon in applications.

By using two analytical methods that were found to produce equations that were not sensitive to the internal resonance conditions, values are obtained for the amplitude ratios between the oscillators in the vicinity of the center of the ILM. These values are listed in table 3.5. Within the table, the first column of values corresponding to the simulation results and the second column and third column correspond to the Restricted Normal Mode Approach and the linearized Invariant-Manifold Approach, respectively. The negative sign indicates that adjacent oscillators are oscillating half a period out of phase. The values of the amplitude ratios

indicate that for three-to-one internal resonance conditions, the Restricted Normal Mode Approach performs better than the linearized Invariant-Manifold Approach but neither method is able to successfully determine a value for the second amplitude ratio.

The r_1 value for the Restricted Normal Mode Approach shows the best agreement with the results obtained from the simulation. When investigated further, this amplitude ratio is found to produce a periodic solution within the simplified model and all of the Floquet multipliers have magnitudes that are less than one. This appears to be due to how successfully the simplified model represents the amplitude profile of the ILM. The greater rate of the decrease of the amplitude values when moving out from the center of the ILM causes $x_{\pm 2}$ to have a very small influence on $x_{\pm 1}$, in agreement with the simplification. However, the simplification is based on the relationship between x_0 and $x_{\pm 1}$ and does not take into account the circumstances surrounding the pair consisting of $x_{\pm 1}$ and $x_{\pm 2}$. In order to improve the performance of this method and obtain a better value for r_2 , a second simplified model is required. In previous work, it has been found that when the amplitude profile of the ILM is used to initialize the displacements of the array, it is possible to initiate the localization phenomenon at the selected location without the transient localizations that form during the ‘chirp’ phase of the excitation. This is done by using initial velocities equal to zero and, after skipping the first phase of the excitation frequency profile, correctly selecting the phase for the constant frequency excitation. Possibly due to the difference between the r_2 value from the simulation and the value obtained from this method, when an amplitude profile is constructed

and used to initialize a simulation, the ILM does not become synchronized and quickly dissipates.

The amplitude ratios produced by the linearized Invariant-Manifold Approach do not show as good agreement with the values obtained from the simulations. Despite the use of a complete model which does not incorporate any simplifications, the calculated value of r_1 is found to be almost twice the value from the simulation. It is found that a periodic solution is not produced when the amplitude ratio is used to initialize the simulation and as a result, Floquet multipliers are not calculated. Also, as with the Restricted Normal Mode Approach, the value calculated for r_2 is found to differ from the simulation value by almost an order of magnitude. One possible explanation for the poor agreement between the values for the amplitude ratio r_2 is that the amplitude values are extremely small and the results from the simulation may still be affected by transient behavior. It should be noted that the standard deviation for the amplitude value of $x_{\pm 2}$ was sixty-eight percent of the average values. In future work, it may be necessary to extend the length of the simulation in order to allow for the further decay of transient localizations.

3.4 Summary

A relationship is identified between nonlinear vibration modes and the so-called intrinsic localized modes more commonly studied in the field of solid state physics. By using methods for calculating nonlinear normal modes, a process is developed to analytically calculate the amplitude profile of these localization events from the

system model. This provides an increased level of understanding of the relationship between the spatial characteristics of the localizations and the system parameters of the array. The ILMs are also studied in systems where the difference between the fundamental frequencies of the devices is increased significantly. Numerical simulations suggest that this will result in changes to the spatial characteristics of the ILMs as well as changes to their behavior within an array. In the next chapter, many of the modeling and simulation methods and nonlinear analyses utilized to study piezoelectric micro-scale resonators are applied to a cantilever beam impactor system in order to study a period doubling phenomenon.

Chapter 4

Cantilever Beam Impactor System

In this chapter, a grazing bifurcation is examined in a system consisting of a cantilever beam with a small tip mass to act as an impactor and a piece of compliant material positioned to constrain the motion of the beam for large amplitude oscillations. The analytical and numerical models for this system are developed in the first section. In the second section, the system's response is studied for different excitation and constraint conditions. Additional experiments conducted with a commercial atomic force microscopy system to ensure that the behavior of the macro-scale test apparatus is representative of the micro-scale system are discussed in the third section.

4.1 System Modeling

Within this section, the macro-scale experimental setup used in this dissertation is discussed and an analytical model is developed for the system. Starting from energy equations, a nonlinear beam model is developed to describe the behavior of this system. A reduced order model is produced through the use of the Galerkin method with a multi-mode approximation. The discretized system is used to simulate the response of the system. Experimental data is utilized in order to identify parameter values and determine the minimum number of mode shapes required to successfully model the behavior of the test apparatus.

4.1.1 Macro-Scale Experimental Setup

The system being investigated consists of a long, slender phosphor bronze beam. The beam is cantilevered from a movable fixture and oriented in such a fashion as to avoid gravitational effects. This is done to represent the negligible effect of gravity on a micro-scale structure when compared to the other forces acting on the system. The fixture is mounted on a ball screw and actuated by an AC servo motor in order to harmonically excite the cantilever beam. The servo motor is controlled by a closed-loop control scheme that employs an optical sensor to monitor the position of the movable fixture. At the free end, a small bolt is affixed to the beam with a hex nut in order to act as an impactor. The response of the beam at the free end is monitored with a laser displacement sensor. This data is used to study the behavior of the system and in the development of the system model. The data is also

compared with the simulated response to verify the performance of the numerical simulation. A compliant contact material made of a very soft foam rubber material is placed onto a high resolution manual stage which is positioned along the beam in line with the impactor. This will allow for collisions to occur periodically between the impactor and the contact material when the stage is sufficiently close to the beam. A diagram of this system is shown in figure 1.9 in chapter one. Some important system parameters are listed in table 1.4 which is also located in chapter one.

4.1.2 Model Development

To model the behavior of this system, a nonlinear beam model is developed, taking into account a number of potential sources of nonlinearity. This is done so that the model is able to accurately describe the large deflections that may be experienced when the beam is excited near resonance. In order to derive the equation of motion, the beam is first assumed to be inextensional. The inextensionality condition provides a relation between the longitudinal displacement of the beam and the transverse displacement of the beam, represented by $w(s, t)$ in the model. This displacement is a function of both time t and the position s along the length of the structure.

The first step toward obtaining the equation of motion for the transverse vibrations of the beam is to determine the kinetic and potential energies of the system. The total kinetic energy consists of the kinetic energy of the beam for both longitudinal and transverse motion and the kinetic energy of the impactor for both

longitudinal and transverse motion. In order to account for the base excitation, a moving reference frame $X(t)$ is utilized to represent the displacement produced by the linear guide actuator [81]. Due to the slenderness of the beam, the rotary inertia is neglected. The rotary inertia of the impactor is also considered to be negligible, allowing for it to be modeled as a point mass. Due to the orientation of the beam, the total potential energy consists of only the potential energy from a bending stiffness term. The total energy equations are combined with a Lagrange multiplier and the inextensionality condition to form the augmented Lagrangian. The augmented Lagrangian and the non-conservative work are combined and the variation of this sum is integrated with respect to time in order to apply the extended Hamilton's principle. For this system, the non-conservative work is produced by the discontinuous contact force, $F_c(t)$, that results from collisions between the impactor and the surface of the contact material. Through this process, and by neglecting terms of orders higher than cubic, a partial differential equation of motion is obtained for the transverse displacement of the cantilever beam. In this equation, over-dots are used to represent derivatives with respect to time and derivatives with respect to position are represented by the prime symbol.

$$\begin{aligned}
& EI w^{iv} + EI \left[w' (w' w'')' \right]' + \\
& \quad + c_l \dot{w} + c_{nl} \dot{w} |\dot{w}| + \\
& + \rho A \ddot{w} - \frac{m_{tip}}{2} w'' \left[\int_0^L \frac{\partial^2}{\partial t^2} (w')^2 ds \right] + \\
& \quad + \frac{\rho A}{2} \left\{ w' \int_L^s \left[\int_0^s \frac{\partial^2}{\partial t^2} (w')^2 ds \right] ds \right\}' = F_b + F_c \tag{4.1}
\end{aligned}$$

This equation, shown as (4.1), includes both linear and nonlinear inertial terms, linear and nonlinear bending stiffness terms, and a nonlinear inertial term corresponding to the impactor. Linear and nonlinear damping terms are also added to account for energy dissipation. The form of these terms is discussed later when the values of the damping coefficients are determined. This equation also includes the forces F_b and F_c acting on the beam as a result of the base excitation and collisions with the contact material, respectively. The force acting on the beam due to the base excitation is calculated as the product of the mass per length of the beam and the acceleration applied to the structure. In the case of harmonic excitation, the force is defined by (4.2) where X_0 is the displacement amplitude of the excitation and ω is the excitation frequency.

$$F_b = -\rho A \ddot{X}(t) = \rho A \omega^2 X_0 \cos(\omega t) \quad (4.2)$$

Since the contact material is compliant in nature, the discontinuous force resulting from contact between the material and the impactor is represented with a piecewise linear model. The contact force, defined by (4.4), consists of a restoring force acting on the beam when the displacement of the beam tip is greater than the separation distance b between the contact material surface and the center of oscillation of the beam. The restoring force, defined by (4.4), is a function of the stiffness and damping coefficients of the contact material and the displacement and velocity of the impactor at the free end of the beam. An additional requirement for the model is that the value of the restoring force must be positive as a negative

value would indicate that the beam has separated from the contact material. This would occur when the beam is moving away from the contact material at a greater rate than the material is able to return to its uncompressed position.

$$F_c = \begin{cases} F_r & w(L, t) > b \text{ and } F_r > 0 \\ 0 & \text{otherwise} \end{cases} \quad (4.3)$$

$$F_r = k_c [w(L, t) - b] + c_c \dot{w}(L, t) \quad (4.4)$$

The boundary conditions, shown as (4.5) and (4.6) for $s = 0$ and as (4.7) and (4.8) for $s = L$, are also obtained from the extended Hamilton's principle. The boundary conditions are those of a uniform cantilever beam with the exception that the shear force at the free end of the beam must balance the inertial force of the impactor.

$$w(s, t)|_{s=0} = 0 \quad (4.5)$$

$$w'(s, t)|_{s=0} = 0 \quad (4.6)$$

$$EI w''(s, t)|_{s=L} = 0 \quad (4.7)$$

$$EI w'''(s, t)|_{s=L} = m_{tip} \ddot{w}(s, t)|_{s=L} \quad (4.8)$$

With these boundary conditions and the partial differential equation of motion, a complete model is established for this system and numerical methods are utilized in order to study its dynamic behavior.

4.1.3 Numerical Simulations

A reduced-order-model is developed from the nonlinear beam model derived in the previous section in order to obtain a discretized model of the system. The discrete model is then used to conduct numerical experiments in order to study the dynamic behavior of the system.

Model Discretization

Through this process, the response of the cantilever beam is approximated by the summation of a finite number of modal responses. By using separation of variables, the transverse displacement of the beam, $w(s, t)$, is separated into a finite number of position dependent mode shapes, $\phi_n(s)$, and time dependent modal responses, $q_n(t)$. The forms of the mode shapes are calculated from a linearized, conservative form of (4.1) which is obtained by removing the nonlinear terms, the damping terms, and the excitation terms. By approximating the behavior of the system with these linear mode shapes, the Galerkin method is applied to the nonlinear beam model. Through this process, a number of $N \times N$ modal parameter matrices and $N \times 1$ modal force vectors are produced where N is the number of mode shapes used to discretize the system. The equations that are used to calculate the values of the components of these matrices and vectors are included in appendix B. This discretization produces the equation of motion that is used to simulate the dynamic behavior of the system. This equation is shown as (4.9).

$$\begin{aligned}
[M] \{\ddot{q}\} + [K] \{q\} + [C_L] \{\dot{q}\} + \\
+ [C_{NL}] \{\dot{q}|\dot{q}\} + [\alpha_1] \{q^3\} + \\
+ [\alpha_2] \{\dot{q}^2 q + q^2 \dot{q}\} = \{F_B\} + \{F_C\}
\end{aligned} \tag{4.9}$$

The mode shapes are normalized causing the mass matrix, $[M]$, to be equal to the identity matrix and the stiffness matrix, $[K]$, to be a diagonal matrix where the components are equal to the system's characteristic frequencies squared. Non-zero off-diagonal components in the modal parameter matrices for the nonlinear stiffness, $[\alpha_1]$, and for the nonlinear inertia, $[\alpha_2]$, reveal nonlinear coupling between the different vibration modes. The linear and nonlinear damping matrices, $[C_L]$ and $[C_{NL}]$, are approximated by using linear and nonlinear damping factors.

The two sources of external force acting on the system are the base excitation and the collisions between the impactor and the contact material surface. The modal forces due to base excitation, $\{F_B\}$, are calculated from the beam properties and excitation conditions. To calculate the values of the modal forces resulting from periodic impacts, the modal responses are combined to determine the system response and the corresponding force acting on the system. Additional calculations are then performed to separate this force into the modal components, $\{F_C\}$, for use within the numerical simulations.

The $N \times 1$ column vector $\{q\}$ contains the modal response coordinates for the first N vibration modes of the system. The components of this vector are operated on as indicated in (4.9) to produce time derivatives and nonlinear terms.

Damping and Contact Material

While the values of the components in the modal mass and modal stiffness matrices are calculated from the geometry of the beam and known material properties, the damping within the system is not quantified quite as easily. To determine the form of the damping and the corresponding coefficient values, an identification process using experimental data is employed. The coefficient values for the stiffness and damping associated with the contact material are also determined with the aid of experimental methods.

In order to accurately model the dissipation of energy by the cantilever beam for the range of motion to be studied, both viscous damping and aerodynamic damping terms are included in the equation of motion. Free-vibration displacement data is collected and the local minima and maxima of the decaying sinusoid are identified and compared with equivalent data produced by numerical simulation. Since the linear and nonlinear damping factors affect the decay of the free vibrating system differently, a unique solution is obtained. The two parameter values are tuned in order to minimize the error between the experimental data and the simulated response. The identified parameter values are presented in table 4.1.

As indicated by (4.4), both the stiffness and damping of the contact material are modeled with linear relationships. This assumption is made since the focus of this investigation is on the transition between unconstrained and constrained behavior, limiting the amount of compression experienced by the contact material. The stiffness of the contact material is calculated with the aid of the high resolution

Table 4.1: Linear and nonlinear damping factors.

Parameter	Value
Linear Damping Factor, ζ_L	4.0×10^{-4}
Nonlinear Damping Factor, ζ_{NL}	1.3 m^{-1}
Stiffness Coefficient, k_c	85.68 N/m
Damping Coefficient, c_c	1.7 Ns/m

manual stage and a force transducer. The restoring force of the contact material is measured under static conditions for a number of different compression distances. This data is then plotted and fit with a linear trend-line to obtain the linear stiffness coefficient in the form of the slope. The values of the stiffness coefficient for the contact material is listed in table 4.1.

In order to obtain a value for the last unknown parameter, the damping coefficient of the contact material, simulated responses are again compared with experimental data but under conditions where the system is excited and periodic collisions occur between the impactor and the surface of the contact material. The value of the damping coefficient is tuned in order to match the response predicted by the simulation with experimental data for the same excitation and constraint conditions. The damping coefficient identified through this comparison is presented in the final row of table 4.1.

Number of Mode Shapes

In order to accurately model the dynamic behavior of the system, simulations are performed and compared with experimental observations in order to determine the minimum number of mode shapes required. Within the investigation, harmonic excitation is applied at frequencies between the system's fundamental frequency and second characteristic frequency. It is determined that a multi-mode approximation is necessary to model the vibrations of the beam, even in the case of unconstrained motion when the system is excited near the fundamental frequency. Under these conditions, quasi-periodic behavior is observed and realized within the model by nonlinear coupling between the system's modes of vibration. The simulated behavior is seen to agree with the experimental observations, as shown in figure 4.1(a) and figure 4.1(b). The data is presented in the form of phase portraits to show the response in greater detail. This provides for a more complete comparison between the experimental and simulated responses. The velocity values for the experimental data are calculated from the measured displacement values. The multi-mode approximation is found to be even more important when the system is experiencing periodic collisions between the impactor and the surface of the contact material. When the separation distance is decreased below a critical value, the contact material constrains the motion of the oscillating beam, partially forcing the first mode of vibration into the profile of the second vibration mode. Phase portrait plots of experimental and simulated responses for constrained conditions are also shown in figure 4.1.

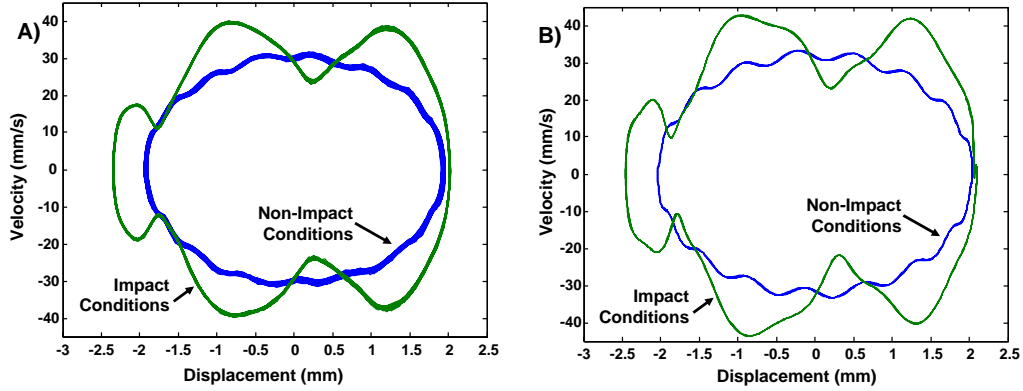


Figure 4.1: Phase portraits of the system’s response to harmonic excitation near the fundamental frequency: (a) the response measured experimentally and (b) the simulated response.

A multi-mode approximation is also required when the system is excited at frequencies between the system’s first and second characteristic frequencies. For unconstrained conditions, the system’s response is observed to be oscillations at the excitation frequency with a considerable amount of amplitude modulation. As in the previous case, this quasi-periodic behavior is realized within the model by the nonlinear coupling. The use of the multi-mode approximation enables the simulation to predict the amplitude modulation, but more importantly it enables the model to provide an accurate simulation of the system’s response for constrained conditions. The response to harmonic excitation with a frequency between the first and second characteristic frequencies for unconstrained and constrained conditions are shown in figure 4.2(a) and figure 4.2(b), respectively. Due to the off-resonance condition, the amplitude of the response is small enough that the experimental measurements are affected by noise. The effect of this noise is further amplified when the velocity of

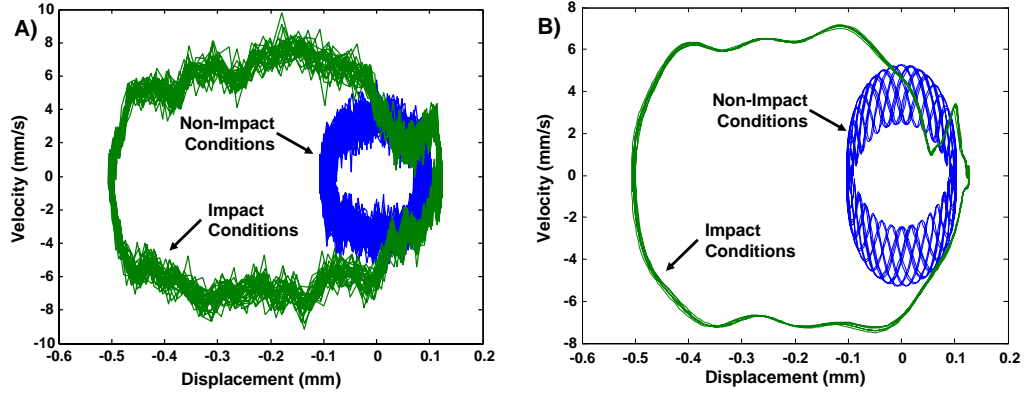


Figure 4.2: Phase portraits of the system’s response to harmonic excitation near two and a half times the fundamental frequency: (a) the response measured experimentally and (b) the simulated response.

the free end of the beam is calculated as the derivative of the displacement. Despite the effects of noise, qualitative agreement is seen between the experimental response and the response predicted by the simulation.

Within this investigation, the first three modes of vibration are used to approximate the response of the system for a number of excitation frequencies between the system’s first and second characteristic frequencies and for various unconstrained and constrained conditions. The quasi-periodic response is found to be due to a coupling between the first and third modes of vibration. The contribution of the third vibration mode is seen to decrease for constrained conditions while the contribution of the second vibration mode increases. Further studies can be conducted to determine if additional model reduction methods can be employed to facilitate further analysis of the identified nonlinear phenomenon.

4.1.4 Micro-Scale System

After studying the macro-scale test apparatus both experimentally and with the aid of the numerical simulations, additional experiments are conducted with a commercial atomic force microscope in order to study the scalability of the nonlinear phenomenon and to determine how well the macro-scale system represented the AFM cantilever probe. The main components of the AFM system are shown in the diagram in Fig. 4.3a. The cantilever probe of this AFM, shown in the SEM image in Fig. 4.3b, is made from single crystal silicon and has the same general shape as the macro-scale cantilever with its length, width, and thickness equal to $450\ \mu\text{m}$, $40\ \mu\text{m}$, and $5\ \mu\text{m}$, respectively. These properties result in a fundamental frequency of 28 kHz. In comparing the relationships between these dimensions with those of the macro-scale test apparatus, the micro-scale cantilever is much less slender with length-to-width and width-to-thickness ratios around 10 to 1 while these ratios for the macro-scale cantilever are greater than 20 to 1. This is believed to be a contributing factor in higher level of nonlinear behavior observed of the macro-scale test apparatus.

As discussed previously, the operation mode of interest is the so-called tapping-mode or intermittent contact mode where by the AFM probe oscillates above the sample, coming in contact with the surface once per period. In order to observe the behavior of the cantilever probe in the commercial system, the output voltage of the photo-diode is monitored. This data is used to study the qualitative behavior of the cantilever probe's response while it is subjected to different excitation and

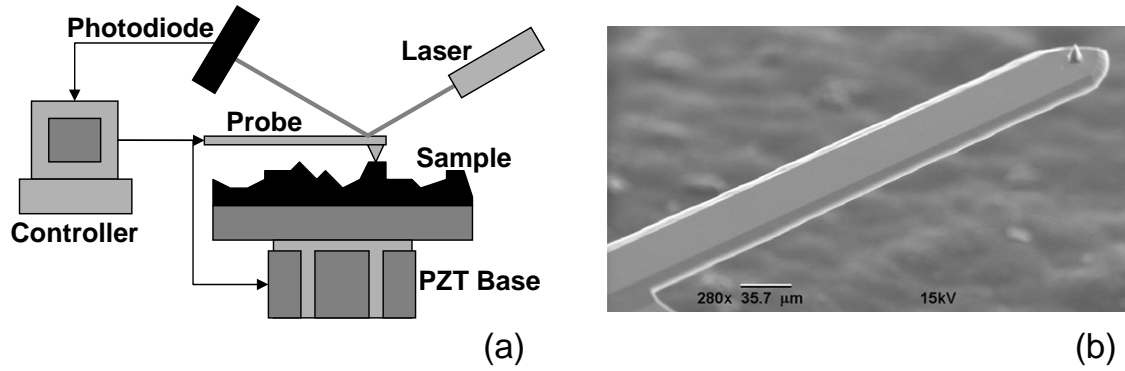


Figure 4.3: (a) Diagram of atomic force microscope system and (b) SEM image of AFM cantilever probe.

constraint conditions. As the commercial AFM system is designed for operation near resonance conditions, the range of excitation is limited and the magnitude of the response for off-resonance conditions is significantly smaller.

4.2 Analysis

With the simulation developed for the cantilever beam impactor system and verified through comparison with experimental data, studies are conducted to investigate the system's response for unconstrained conditions and various constrained conditions. The responses of the system under these conditions are studied in order to determine a way to locate the critical separation distance corresponding to grazing. The two parameters that are varied within these studies are the excitation frequency and the separation distance. After preliminary studies are conducted, two excitation frequencies are selected for a more thorough investigation. The two frequencies examined are 2.50 Hz and 6.25 Hz. The first excitation frequency is very close

to the system's fundamental frequency, which is 2.42 Hz and corresponds to the standard excitation condition for tapping-mode atomic force microscopy. The second excitation frequency has a value of about two and a half times the fundamental frequency but less than the second characteristic frequency, which is 15.16 Hz.

4.2.1 Excitation Near ω_1

The first excitation frequency that is investigated, 2.50 Hz, is very close to the fundamental frequency of the system and consequently, the response amplitude benefits from the resonance condition. When comparing the system's response for unconstrained and constrained conditions, a visual examination of the phase portraits in figure 4.1 reveals significant differences. However, to develop a successful method to locate the critical separation distance that corresponds to the grazing, it is desirable to be able to quantify the changes in the system's response in a way that can be calculated in real-time from the displacement time series of the system. Time series plots of the system's response for this excitation condition are shown in figure 4.4. This comparison shows no noticeable change in the response frequency and very little change in the amplitude of the response. A comparison of the two time series plots reveals that the response under constrained conditions is affected by small amplitude harmonics of the excitation frequency.

In order to further examine how the system's response changes with the addition of periodic impacts, spectral information for the response signals is calculated with a fast Fourier transform and examined. The frequency spectrum plots for the

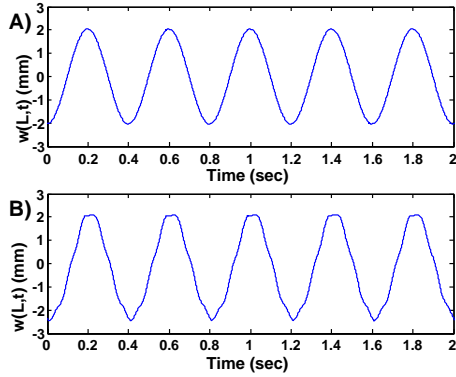


Figure 4.4: Plots of the system response for excitation near the fundamental frequency: (a) the system’s response for unconstrained conditions and (b) the system’s response for constrained conditions.

system’s response for unconstrained conditions and for constrained conditions are presented as figure 4.5(a) and figure 4.5(b), respectively. These figures indicate that the main component of the response, at the excitation frequency, does not change. This confirms the observations made from the time series plots. These plots also reveal a number of other frequency components. For the unconstrained response, figure 4.5(a) reveals a second significant frequency component at 42.49 Hz, the system’s third characteristic frequency. This component accounts for the quasi-periodic behavior observed in the phase portraits. For the response of the beam impactor system under constrained conditions, there are many more frequency components in the spectral plot of the system’s response. The largest of the new components appears at the system’s second characteristic frequency and is produced by the collisions in the manner discussed previously. A number of other frequency components in the responses occur at integer multiples of the excitation frequency but the magnitudes

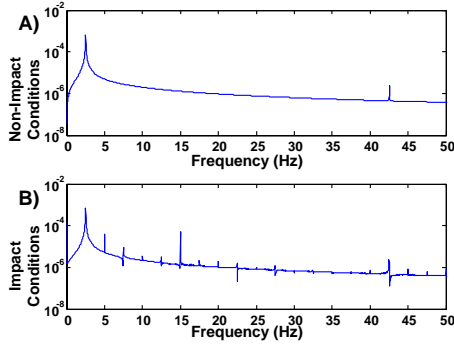


Figure 4.5: Frequency spectrum plots of the system response for excitation near the fundamental frequency: (a) the system’s response for unconstrained conditions and (b) the system’s response for constrained conditions.

of these components are significantly less than the components discussed.

Although it is clear that the system’s response changes when the separation distance is sufficiently decreased to produce constrained conditions, the changes are relatively small and they are generally quantitative with respect to the different vibration modes. For the very soft contact material used in this dissertation, these changes are found to be extremely small.

4.2.2 Excitation Near $2.5 \times \omega_1$

During the preliminary investigation into the response of the experimental system under constrained conditions, a unique nonlinear phenomenon was observed for an excitation frequency value of 6.25 Hz. When excited with this frequency, which is about two and a half times the system’s fundamental frequency, the response of the system undergoes a significant qualitative change for constrained conditions. The

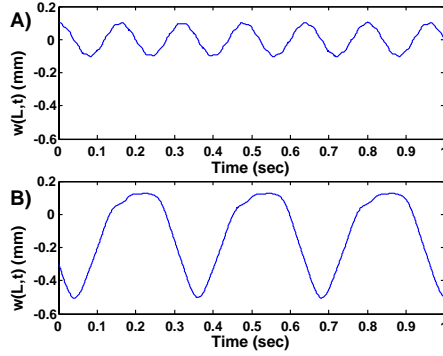


Figure 4.6: Plots of the system response for excitation near two and a half times the fundamental frequency: (a) the system’s response for unconstrained conditions and (b) the system’s response for constrained conditions.

response of the system changes from quasi-periodic behavior to a response with a period twice as long as the period of the excitation. Period-two responses have been observed in other similar experimental systems for excitation frequency values around this multiple of their fundamental frequencies as well as for higher excitation frequencies [82]. The responses at this excitation frequency for unconstrained and constrained conditions are plotted in figure 4.6(a) and figure 4.6(b), respectively. For the system examined in this dissertation, the amplitude of this period-two response increases significantly from the amplitude of the unconstrained response. This drastic qualitative change in the system’s behavior at the critical separation distance appears to provide a means to locate grazing.

In the same manner as for the previous excitation frequency, spectral information is calculated for the system’s response for both unconstrained and constrained conditions. The frequency spectrum plot in figure 4.7 reveals that the quasi-periodic

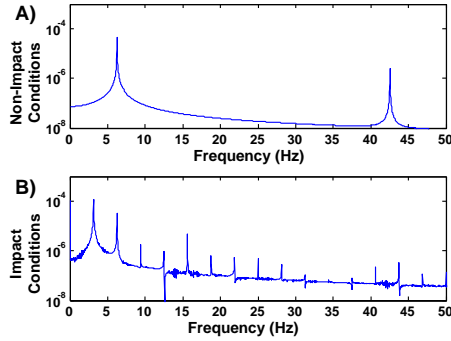


Figure 4.7: Frequency spectrum plots of the system response for excitation near two and a half times the fundamental frequency: (a) the system’s response for unconstrained conditions and (b) the system’s response for constrained conditions.

behavior is also caused by system’s third mode of vibration. The frequency spectrum plot of the response for constrained conditions reveals many more frequency components for this excitation frequency. While the magnitudes of most of these components are very small, a new component is produced at half of the excitation frequency. This sub-harmonic of the excitation frequency accounts for the period-two behavior observed in the time series plots. Unlike the frequency components produced during constrained conditions for the previous excitation frequency, this component has a magnitude on the same order as the component at the excitation frequency and is easily identified, even in the presence of noise.

For an excitation frequency with a value of about two and a half times the fundamental frequency, a significant qualitative change occurs to the response when the separation distance is sufficiently decreased to produce constrained conditions. Even for the extremely soft material used in this dissertation research, the change in the response is drastic and easily quantified.

4.2.3 Floquet Theory

With the aid of the numerical simulation, Floquet theory is employed to study the stability of the periodic behavior of the macro-scale test apparatus. The results of this analysis indicate that the unconstrained periodic responses of the system for both excitation frequencies are stable, with all Floquet multipliers having magnitudes less than one. For the constrained conditions, the periodic responses for excitation frequencies of both 2.50 Hz and 6.25 Hz are both found to be stable. Under these constrained conditions, the stability of the response is further improved due to the additional damping from the constraining material. This is observed as a decrease in the magnitudes of the Floquet multipliers. Due to the rather abrupt transition across the critical separation distance that would correspond to grazing, the presence of a period-doubling bifurcation can not be conclusively determined.

4.2.4 Grazing Bifurcation

In order to continue studying the changes to the system's response that occur when the separation distance is decreased sufficiently to produce constrained conditions, Poincaré sections are calculated from the system's responses and assembled to produce bifurcation diagrams [75]. This is done for the response of the system when it is excited harmonically at 2.50 Hz and when the excitation frequency is 6.25 Hz by using the separation distance as the control parameter.

When the beam impactor system is excited harmonically at a frequency near the fundamental frequency, the resulting bifurcation diagram, shown in figure 4.8,

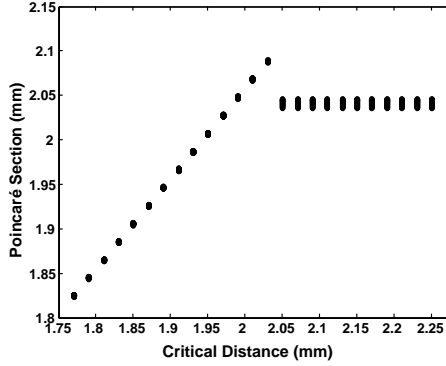


Figure 4.8: A bifurcation diagram for harmonic excitation near the fundamental frequency. The separation distance between the beam’s center of oscillation and the surface of the contact material is used as the control parameter.

reveals a change in the response amplitude. Also, it should be noted that the Poincaré sections for the unconstrained response are identical as there is no change to the dynamic system until the separation distance is decreased below the critical distance. The data points within these Poincaré sections are distributed across a small range of amplitude values due to the quasi-periodic nature of the response. This quasi-periodicity is shown in figure 4.9 where the Poincaré section is shown to produce a closed curve in phase space. This unique bifurcation, where a quasi-periodic response becomes periodic, is observed as a result of the use of a control parameter that corresponds to the structure of the system.

For the other excitation case that is being examined, more complex behavior is revealed by the bifurcation diagram, shown as figure 4.10. When the system is excited near two and a half times the fundamental frequency, the quasi-periodic unconstrained response changes into a periodic response with a period twice as long

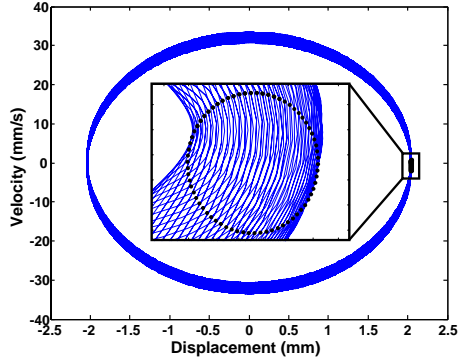


Figure 4.9: A phase portrait of the system’s unconstrained response to harmonic excitation near the fundamental frequency. The enlarged section of the plot shows the Poincaré section which reveals the quasi-periodic nature of the response.

as the period of the excitation. As with the previous bifurcation diagram, Poincaré sections corresponding to the unconstrained response of the system are spread across a range of amplitude values due to its quasi-periodic nature. The quasi-periodicity of the response is shown in figure 4.11 with a Poincaré section plotted within a phase portrait.

4.3 Micro-Scale System

After working with the macro-scale test apparatus to study this nonlinear phenomenon, experiments are conducted with a commercial AFM system. This is done to verify that the nonlinear behavior observed within the macro-scale system was representative of the micro-scale structure. The behavior of the system is studied for two excitation frequencies, the first frequency is near the fundamental frequency of the AFM probe and the second frequency is at a value of about two and a half

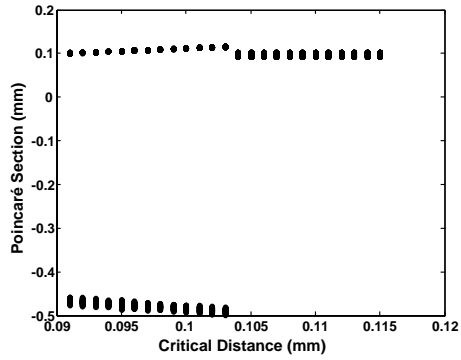


Figure 4.10: A bifurcation diagram for harmonic excitation near two and a half times the fundamental frequency. The separation distance between the beam's center of oscillation and the surface of the contact material is used as the control parameter.

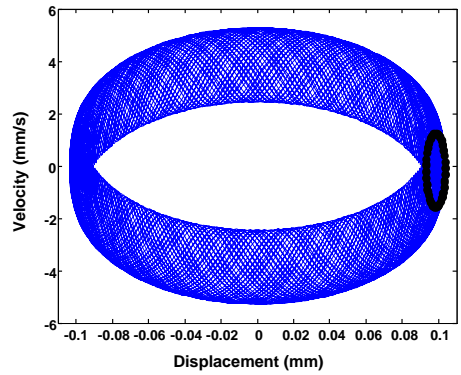


Figure 4.11: A phase portrait of the system's unconstrained response to harmonic excitation near two and a half times the fundamental frequency. The Poincaré section reveals the quasi-periodic nature of the response.

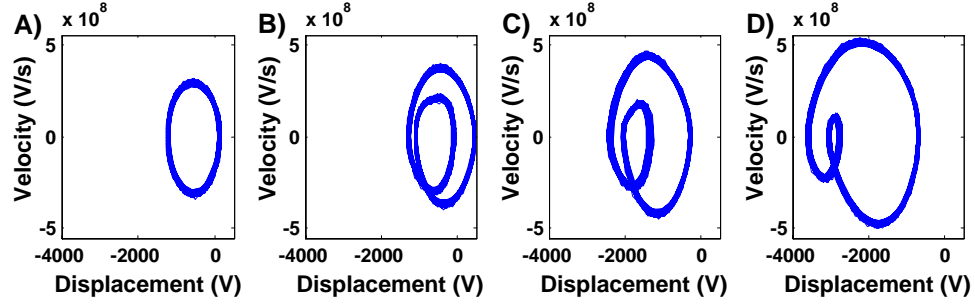


Figure 4.12: Phase portraits of data collected from commercial AFM system for an excitation frequency of two and a half times the fundamental frequency: (a) the unconstrained response and (b) - (d) the response of system under constrained conditions as the separation distance is incrementally decreased.

times the fundamental frequency. In comparing the experimental data from the micro-scale system with the behavior studied in the macro-scale test apparatus, there are some discrepancies. These may be caused by the differences between the macro-scale test apparatus and the micro-scale structure. Due to these differences, the behavior of the AFM probe does not exhibit quasi-periodic behavior, suggesting a decreased level of nonlinearity. In addition, the response of the system to an excitation frequency of two and a half times the fundamental frequency has a much smoother transition from unconstrained to constrained behavior. The phase portraits in figure 4.12 show this transition. The AFM probe oscillates harmonically when the separation distance is greater than the critical value, as shown in figure 4.12(a). The manner in which the AFM probe's response changes as the separation distance is decreased beyond the critical value is presented in figure 4.12(b) through figure 4.12(d).

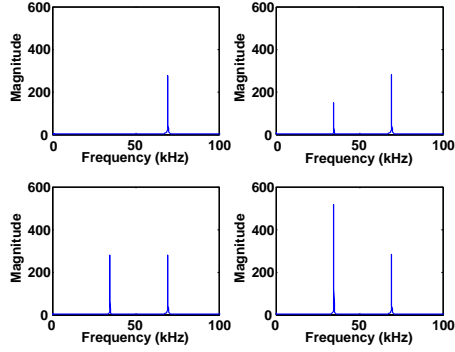


Figure 4.13: Frequency spectrum plots of data collected from commercial AFM system for an excitation frequency of two and a half times the fundamental frequency: (a) the system’s unconstrained response and (b) - (d) the response of system under constrained conditions as the separation distance is incrementally decreased.

To gain a better understanding of how the response of the AFM probe changes as the separation distance is incrementally decreased beyond the critical value, the data plotted in figure 4.12 is analyzed with a fast Fourier transform in order to examine the frequency components. This spectral information is plotted in figure 4.13. The spectral information for unconstrained conditions, in figure 4.13(a), reveals a single significant frequency component at the excitation frequency. The spectral information plot for the system’s response under constrained conditions in figure 4.13(b) contains a second significant frequency component, located at half of the excitation frequency. The frequency spectrum plots in figure 4.13(c) and figure 4.13(d) indicate that as the center of oscillation of the probe is moved closer to the surface of the sample, the strength of the sub-harmonic of the excitation frequency will increase.

The changes in the response observed of the AFM probe are more desirable than those observed in the macro-scale experiment. For the macro-scale system, the transition is very sudden but a smoother transition across the grazing point is observed for the AFM probe. A bifurcation diagram illustrating this transition is presented in figure 4.14. While the presence of the sub-harmonic, resulting in period-two behavior, indicates that constrained conditions exist, the relationship between the separation distance and the magnitude of this frequency component provides a means to locate grazing. By monitoring the magnitude of the sub-harmonic component, the separation distance will be tuned in order to find the critical separation distance. Additionally, the response transition for the AFM probe reveals that when the separation distance is only a small amount less than the critical value, the sub-harmonic frequency component will be present but small in magnitude and not result in the large increase in force associated with the response transition of the macro-scale system.

The qualitative difference in the transition between unconstrained and constrained motion for the two systems is believed to be due to the difference between the ratios of the beam's stiffness to the stiffness of the contact material. In the case of the macro-scale experiment, an extremely soft foam rubber material is used to provide an extreme case and to ensure that the system was successfully representing conditions that would be comparable to an AFM system imaging a delicate sample such as a living biological specimen. The 'soft', silicone material available for the micro-scale experiments was relatively stiffer. While this suggests that the exact behavior observed of the micro-scale structure may not be identical to the form of

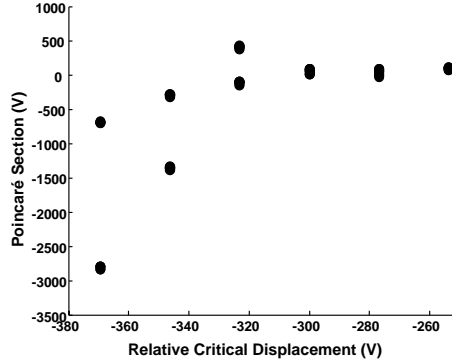


Figure 4.14: A bifurcation diagram of the data collected from the commercial AFM system for an excitation frequency of two and a half times the fundamental frequency. Period-doubling is shown to occur at the grazing bifurcation.

the response when imaging a much softer sample, it provides a starting point to develop a new control methods for AFM that will utilize this nonlinear phenomenon to minimize the magnitude of the contact force acting on the sample, thus improving the capabilities of atomic force microscopy. Additional research can be conducted to further study this stiffness relationship and to explore potential methods to obtain smooth transitions for much softer material.

4.4 Summary

An analytical model is developed to describe the nonlinear transverse oscillations of a slender cantilever beam with a soft material constraining the motion of the free end of the beam for sufficiently large amplitude oscillations. The model is developed, discretized, and the parameter values are determined, both analytically and experimentally. Through simulations and experiments, a qualitative change in

the system's response associated with a grazing bifurcation is identified and studied toward the goal of developing a control scheme to locate grazing in tapping mode atomic force microscopy. Micro-scale experiments conducted with a commercial AFM system show qualitative agreement with the macro-scale study.

Chapter 5

Conclusions and Future Work

Within this dissertation, the nonlinear oscillations of beam and beam-like structures are studied with a specific focus on micro-scale structures. Through this research, the following contributions resulted. A multi-variable, parametric identification scheme is developed to quantitatively characterize dynamic systems that display Duffing-like nonlinearities. This powerful tool is able to determine parameter values for a system from frequency-response data collected for an increasing frequency sweep without prior knowledge of the linear parameters. The application of this tool to data collected from piezoelectric micro-scale resonators demonstrates how it can be used for material characterization and to study how device performance is influenced by changes to the operating conditions. The second contribution is the identification of a relationship between nonlinear vibration modes of nonlin-

ear mechanics and the intrinsic localized modes of solid state physics. A process is developed to utilize various methods for calculating nonlinear normal modes in order to analytically determine the spatial characterizes of the intrinsic localized modes based on the system model and parameter values. A third contribution of the research detailed in this dissertation is the identification of a period-doubling phenomenon associated with grazing in tapping mode atomic force microscopy. This phenomenon, studied with a macro-scale test apparatus and verified with a commercial AFM system, will provide a means by which a novel AFM operation mode can be developed utilizing a control scheme to locate grazing, thus minimizing the impact force of the AFM probe acting on the sample surface.

5.1 Parametric Identification

In chapter two, a parametric identification scheme is developed with the capability of analyzing nonlinear systems that exhibit jumps in their frequency-response behavior. In addition to its ability to identify the parameter values corresponding to a nonlinear model, this identification scheme can also provide additional information about a device such as the axial force within the structure and the average residual stress level. The identification scheme is applied to frequency-response data collected from piezoelectric micro-scale resonators in order to quantify their nonlinear behavior. Methods are developed to determine the values of an equivalent viscous damping coefficient, a linear stiffness coefficient, a nonlinear stiffness coefficient, a modal force parameter, the level of axial force, and the modal mass of the resonator.

The identification scheme has been successfully applied to data obtained from both PZT and AlGaAs micro-scale resonators. The parameter values are also compared to numerical values obtained from a beam model and agreement is seen. The identification scheme is applied to multiple data sets and parameter trends have also been studied. These parameter trends provide information about the performance of the device and how it relates to the operating conditions. The parameter trends are also used for material characterization to determine values for the piezoelectric coefficient of the thin-film PZT.

In future work, this identification scheme can be applied to other systems, both micro-scale and macro-scale in order to identify system parameters and study device performance. This identification scheme could also be used for additional work in material characterization, utilizing devices specifically designed for this purpose. It is also conceivable that a parametric identification scheme such as that discussed in this work can be used to tailor the characteristics of a MEMS array, so that phenomenon such as localization [83, 49] can be engineered to improve the performances of the considered devices.

5.2 Intrinsic Localized Modes

In the third chapter, a relationship is identified between nonlinear vibration modes and intrinsic localized modes and a process is developed to analytically determine the spatial characteristics of the localization from the system model and parameters. The ability to analytically determine the amplitude profile for an ILM in an array

of coupled nonlinear oscillators can be very beneficial in employing this nonlinear localization phenomenon in MEMS devices. As shown in Figure 3.4(b), it may be possible to use the amplitude profile to select initial displacement values for an array to initiate ILMs within micro-resonator arrays at desired locations. Additional studies have shown that initializing as few as five oscillators at the desired site of localization may be sufficient to produce an ILM. This could be realized with the aid of micro-manipulation techniques such as optical tweezers. Once the ILM has been produced, it can then be maneuvered and interrupted with the addition of an artificial impurity to the array [55]. This level of control over intrinsic localized modes gives the phenomenon a great deal of potential for applications in developing technologies with MEMS arrays.

In future work, additional studies can be conducted to study localizations in other systems and expand the developed process to be able to analytically predict the spatial characteristics of those systems. Experimental work can be done to verify the results of the analytical and numerical efforts. This would require the development of a method to monitor the behavior of the resonators with more detail than the method currently employed. With the aid of the results of this dissertation, additional work could be done to study the behavior of ILMs, such as interactions between ILMs and their behavior as they dissipate following the excitation is removed.

5.2.1 Internal Resonance

The investigation into the effects of internal resonance conditions on ILMs discussed in third section of chapter three suggests that for the oscillator model studied, internal resonance conditions do not uniquely affect the behavior and characteristic amplitude profiles of ILMs. This is believed to be due to the presence of the linear coupling term. The results of the linearized Invariant-Manifold Approach include coefficients where the denominator includes frequencies as well as a term from the coupling. As a result, a new internal resonance condition is produced where the resonance frequency of one type of oscillator is a function of the resonance frequency of the other type of oscillator and a coupling term.

Further investigations can be done to explore these new resonance conditions and determine if they correspond to any unique resonance behavior or if it is just a limitation of this analysis method. Also, by replacing the linear coupling with a nonlinear coupling, it may be possible to study unique phenomena associated with the three-to-one internal resonance conditions and determine how they affect the behavior of ILMs. Despite the inability of the restricted normal mode approach and the modified invariant manifold approach to accurately capture the amplitude ratios associated with the amplitude profile for an ILM within a system with three-to-one internal resonance, the results produced by these methods do show a successful qualitative response to the changes in the system's parameters. This suggests that analysis methods such as these will be capable of analytically calculating the amplitude profile after details such as the model simplification are better addressed.

5.3 Cantilever Beam Impactor System

Within the fourth chapter of this dissertation, the nonlinear behavior of a cantilever beam impactor system is studied. The response of the system to harmonic excitation at two frequencies, 2.50 Hz and 6.25 Hz, is examined for unconstrained and various constrained conditions.

The system's response for an excitation frequency near the fundamental frequency is found to transition from quasi-periodic for unconstrained conditions to period-one motion when constrained conditions are introduced. As the separation distance is decreased further, the response amplitude is observed to decrease. The displacement time series plots reveal little difference between the response for unconstrained motion and the response when constrained conditions exist. A spectral analysis of the data further supports this assertion as there is no significant change in the main frequency component and the magnitudes of the other frequency components are considerable smaller. Since the only changes observed of the response when the separation distance is decreased to produce constrained conditions are small, they may become very difficult to detect if the system is altered, i.e. different contact material. Consequentially, this excitation condition does not provide the desirable means to determine the critical separation distance corresponding to grazing behavior.

A more complex transition is identified for the system's response to an excitation frequency near two and a half times the fundamental frequency. For these conditions, the response of the system is observed to change from quasi-periodic be-

havior to period-two behavior when constrained conditions are introduced. As the separation distance is decreased further, the displacement values from the Poincaré section decrease in magnitude, with the positive values reacting in the same way as the values for the other excitation frequency. For this excitation case, the displacement time series for constrained conditions displays period-two behavior. Spectral analysis of the response confirms this with the presence of a frequency component of significant magnitude at half the excitation frequency. Many other frequency components are produced after constrained conditions are introduced but their magnitudes are significantly less than the two main components. Due to the rather sudden transition from one type of behavior to the other, the presence of a period-doubling bifurcation can not be conclusively determined using Floquet theory. With a significant qualitative change in the system's response when transitioning from unconstrained motion to constrained conditions, the means to determine the critical separation distance corresponding to grazing behavior is provided by this excitation conditions.

Additional work [84] is currently underway by my Japanese colleagues toward the development of a method to monitor the magnitude of the sub-harmonic of the excitation frequency in real-time and control the center of excitation of the beam to minimize the magnitude of the contact force acting on the surface of the sample. The model and simulation presented in the dissertation need to be adapted to study the behavior of the micro-scale AFM cantilever probe, incorporating multi-scale modeling to obtain accurate information for tip-sample interactions. Additional studies can also be conducted to examine how changes in the properties of the

contact material affect the system's response to harmonic excitation near two and a half times the fundamental frequency.

Appendix A

Analytical Methods

In this appendix, the details of the different analyses carried out in chapter three are outlined.

A.1 Method of Multiple Scales Approach

Ordered Equation of Motion:

$$\ddot{q}_j + \omega_j^2 q_j + \epsilon G_j = 0 \quad (\text{A.1})$$

$$\ddot{q}_k + \omega_k^2 q_k + \epsilon G_k = 0 \quad (\text{A.2})$$

Time Scales, Expansions, and Derivatives:

$$t = T_0 + \epsilon T_1 + \dots \quad (\text{A.3})$$

$$q_j = q_{j,0} + \epsilon q_{j,1} + \dots \quad (\text{A.4})$$

$$\frac{d}{dt} = \frac{\partial T_0}{\partial t} \frac{\partial}{\partial T_0} + \frac{\partial T_1}{\partial t} \frac{\partial}{\partial T_1} + \dots = D_0 + \epsilon D_1 + \dots \quad (\text{A.5})$$

Substitution into Governing Equations and Expansion:

$$\begin{aligned} (D_0 + \epsilon D_1 + \dots)^2 (q_{j,0} + \epsilon q_{j,1} + \dots) + \\ + \omega_j^2 (q_{j,0} + \epsilon q_{j,1} + \dots) + \epsilon G_j = 0 \end{aligned} \quad (\text{A.6})$$

$$\begin{aligned} (D_0 + \epsilon D_1 + \dots)^2 (q_{k,0} + \epsilon q_{k,1} + \dots) + \\ + \omega_k^2 (q_{k,0} + \epsilon q_{k,1} + \dots) + \epsilon G_k = 0 \end{aligned} \quad (\text{A.7})$$

Hierarchy of Equations: Order $O(\epsilon^0)$

$$D_0^2 q_{j,0} + \omega_j^2 q_{j,0} = 0 \quad (\text{A.8})$$

$$D_0^2 q_{k,0} + \omega_k^2 q_{k,0} = 0 \quad (\text{A.9})$$

Hierarchy of Equations: Order $O(\epsilon)$

$$D_0^2 q_{j,1} + \omega_j^2 q_{j,1} = -G_j - 2 D_0 D_1 q_{j,0} \quad (\text{A.10})$$

$$D_0^2 q_{k,1} + \omega_k^2 q_{k,1} = -G_k - 2 D_0 D_1 q_{k,0} \quad (\text{A.11})$$

Solution of Order $O(\epsilon^0)$ System:

$$q_{j,0} = 0 \quad (\text{A.12})$$

$$\begin{aligned} q_{k,0} &= A_k(T_1) e^{i \omega_k T_0} + \bar{A}_k(T_1) e^{-i \omega_k T_0} \\ &= a(T_1) \cos(\omega_k T_0 + \beta_k(T_1)) \end{aligned} \quad (\text{A.13})$$

Order $O(\epsilon)$ system: Substitution and Expansion, where ‘cc’ is the complex conjugate of preceding terms.

$$\begin{aligned}
D_0^2 q_{j,1} + \omega_j^2 q_{j,1} &= -g_{1,j,k} A_k^3 e^{i3\omega_k T_0} - 3g_{1,j,k} A_k^2 \bar{A}_k e^{i\omega_k T_0} - \\
&\quad -g_{2,j,k} A_k e^{i\omega_k T_0} + cc
\end{aligned} \tag{A.14}$$

$$\begin{aligned}
D_0^2 q_{k,1} + \omega_k^2 q_{k,1} &= -2i\omega_k A'_k e^{i\omega_k T_0} - g_{1,k,k} A_k^3 e^{3i\omega_k T_0} - \\
&\quad -3g_{1,k,k} A_k^2 \bar{A}_k e^{i\omega_k T_0} - g_{2,k,k} A_k e^{i\omega_k T_0} + cc
\end{aligned} \tag{A.15}$$

Collecting Sources of Secular Terms in Eqn. Governing k^{th} Oscillator and Setting the Sum to Zero: Complex Modulation Equation

$$-2i\omega_k A'_k - 3g_{1,k,k} A_k^2 \bar{A}_k - g_{2,k,k} A_k = 0 \tag{A.16}$$

Substitution of Polar Form for Complex Amplitude:

$$A_k = \frac{1}{2} a_k(T_1) e^{i\beta_k(T_1)} \tag{A.17}$$

$$\bar{A}_k = \frac{1}{2} a_k(T_1) e^{-i\beta_k(T_1)} \tag{A.18}$$

Amplitude and Phase Modulation Equations:

$$a'_k(T_1) = 0 \tag{A.19}$$

$$a_k(T_1) \beta'_k(T_1) = \frac{1}{2} \frac{g_{2,k,k}}{\omega_k} a_k(T_1) + \frac{3}{8} \frac{g_{1,k,k}}{\omega_k} a_k^3(T_1) \tag{A.20}$$

Amplitude and Phase Responses of k^{th} Oscillator:

$$a_k(T_1) = a_k(0) \tag{A.21}$$

$$\beta_k(T_1) = \left(\frac{1}{2} \frac{g_{2,k,k}}{\omega_k} + \frac{3}{8} \frac{g_{1,k,k}}{\omega_k} a_k^2(0) \right) T_1 + \beta_k(0) \tag{A.22}$$

Phase Angle & Nonlinear Frequency:

$$\theta(T_0) = \omega_{Nk} T_0 + \beta_k(0) \tag{A.23}$$

$$\omega_{Nk} = \omega_k + \epsilon \left(\frac{1}{2} \frac{g_{2,k,k}}{\omega_k} + \frac{3}{8} \frac{g_{1,k,k}}{\omega_k} a_k^2(0) \right) \tag{A.24}$$

Substitution into Order ϵ Equation of Motion of j^{th} Oscillator:

$$D_0^2 q_{j,1} + \omega_j^2 q_{j,1} = -g_{1,j,k} A_k^3 e^{i3\omega_k T_0} - 3g_{1,j,k} A_k^2 \bar{A}_k e^{i\omega_k T_0} - g_{2,j,k} A_k e^{i\omega_k T_0} + cc \quad (\text{A.25})$$

Response of j^{th} Oscillator:

$$q_j = \frac{3g_{1,j,k} A_k^2 \bar{A}_k + g_{2,j,k} A_k}{\omega_k^2 - \omega_j^2} e^{i\omega_k T_0} + \frac{3g_{1,j,k} \bar{A}_k^2 A_k + g_{2,j,k} \bar{A}_k}{\omega_k^2 - \omega_j^2} e^{-i\omega_k T_0} + \frac{g_{1,j,k}}{9\omega_k^2 - \omega_j^2} (A_k^3 e^{i3\omega_k T_0} + \bar{A}_k^3 e^{-i3\omega_k T_0}) + \dots \quad (\text{A.26})$$

Displacement and Velocity of j^{th} Oscillator:

$$q_j = \frac{g_{2,j,k}}{\omega_k^2 - \omega_j^2} a_k(T_1) \cos(\theta(T_0)) + \frac{3g_{1,j,k}}{4(\omega_k^2 - \omega_j^2)} a_k^3(T_1) \cos(\theta(T_0)) + \frac{g_{1,j,k}}{4(9\omega_k^2 - \omega_j^2)} a_k^3(T_1) \cos(3\theta(T_0)) + \dots \quad (\text{A.27})$$

$$p_j = \frac{g_{2,j,k}}{\omega_k^2 - \omega_j^2} (-\omega_k a_k(T_1) \sin(\theta(T_0))) + \frac{3g_{1,j,k}}{4(\omega_k^2 - \omega_j^2)} (-\omega_k a_k^3(T_1) \sin(\theta(T_0))) + \frac{3g_{1,j,k}}{4(9\omega_k^2 - \omega_j^2)} (-\omega_k a_k^3(T_1) \sin(3\theta(T_0))) + \dots \quad (\text{A.28})$$

Determined Nonlinear Vibration Mode:

$$q_j = \left(\frac{g_{2,j,k}}{\omega_k^2 - \omega_j^2} \right) q_k + \left(\frac{(7\omega_k^2 - \omega_j^2) g_{1,j,k}}{(9\omega_k^2 - \omega_j^2)(\omega_k^2 - \omega_j^2)} \right) q_k^3 + \left(\frac{6g_{1,j,k}}{(9\omega_k^2 - \omega_j^2)(\omega_k^2 - \omega_j^2)} \right) p_k^2 q_k + \dots \quad (\text{A.29})$$

$$\begin{aligned}
p_j = & \left(\frac{g_{2,j,k}}{\omega_k^2 - \omega_j^2} \right) p_k + \left(\frac{3(3\omega_k^2 - \omega_j^2)g_{1,j,k}}{(9\omega_k^2 - \omega_j^2)(\omega_k^2 - \omega_j^2)} \right) p_k q_k^2 + \\
& + \left(\frac{6g_{1,j,k}}{(9\omega_k^2 - \omega_j^2)(\omega_k^2 - \omega_j^2)} \right) p_k^3 + \dots
\end{aligned} \tag{A.30}$$

A.2 Restricted Normal Mode Approach

Equations of Motion of Simplified System:

$$m_a \ddot{x}_a(t) + (k_{2a} + 2k_I) x_a(t) + k_4 x_a^3(t) = k_I x_b(t) \tag{A.31}$$

$$m_b \ddot{x}_b(t) + (k_{2b} + 2k_I) x_b(t) + k_4 x_b^3(t) = 2k_I x_a(t) \tag{A.32}$$

Harmonic Approximation:

$$x_a(t) = A \sin(\omega t) \tag{A.33}$$

$$x_b(t) = B \sin(\omega t) \tag{A.34}$$

Substitute into Equations of Motion:

$$(A k_{2a} - B k_I + 2A k_I - A \omega^2 m_a) \sin(\omega t) + A^3 k_4 \sin^3(\omega t) = 0 \tag{A.35}$$

$$(B k_{2b} + 2B k_I - 2A k_I - B \omega^2 m_b) \sin(\omega t) + B^3 k_4 \sin^3(\omega t) = 0 \tag{A.36}$$

Retain Only Primary Frequency Component:

$$\left(A k_{2a} + 2A k_I - B k_I - A \omega^2 m_a + \frac{3}{4} A^3 k_4 \right) \sin(\omega t) = 0 \tag{A.37}$$

$$\left(B k_{2b} - 2A k_I + 2B k_I - B \omega^2 m_b + \frac{3}{4} B^3 k_4 \right) \sin(\omega t) = 0 \tag{A.38}$$

Combining Equations to Eliminate Frequency and Resulting Characteristic Equation:

$$AB [m_b (k_{2a} + 2k_I) - m_a (k_{2b} + 2k_I)] + k_I (2A^2 m_a - B^2 m_b) + \frac{3}{4} AB k_4 (A^2 m_b - B^2 m_a) = 0 \quad (\text{A.39})$$

Oscillation Amplitudes:

$$A = R \sin(\theta) \quad (\text{A.40})$$

$$B = R \cos(\theta) \quad (\text{A.41})$$

$$p = \frac{A}{B} = \tan(\theta) \quad (\text{A.42})$$

Equation to Determine Amplitude Ratio p :

$$k_I (1 + p^2) [2m_a p (1 - p) + m_b (1 - 2p)] - p (1 + p^2) (k_{2a} m_b - k_{2b} m_a) + \frac{3}{4} R^2 k_4 p (m_a - m_b p^2) = 0 \quad (\text{A.43})$$

A.3 Real-Variable Invariant-Manifold Approach

Equations of Motion:

$$\dot{q}_j = p_j \quad (\text{A.44})$$

$$\dot{p}_j = -\omega_j^2 q_j - G_j \quad (\text{A.45})$$

Nonlinear and Coupling Terms:

$$G_j = \sum_k (g_{1,j,k} q_k^3 + g_{2,j,k} q_k) \quad (\text{A.46})$$

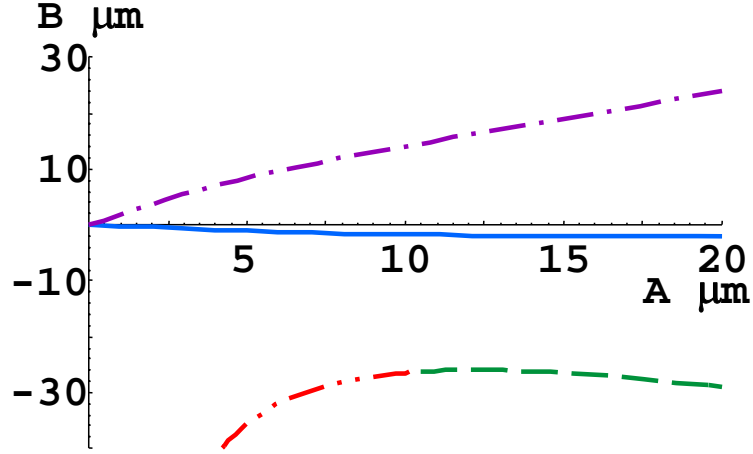


Figure A.1: System of Interest: Amplitude Relations Determined By Numerically Solving for p .

Manifold Equations:

$$q_j = Q_j(q_k, p_k) \quad (\text{A.47})$$

$$p_j = P_j(q_k, p_k) \quad (\text{A.48})$$

$$q_k = Q_k(q_k, p_k) \quad (\text{A.49})$$

$$p_k = P_k(q_k, p_k) \quad (\text{A.50})$$

$$q_j = Q_j(0, 0) = 0 \quad (\text{A.51})$$

$$p_j = P_j(0, 0) = 0 \quad (\text{A.52})$$

Form of Manifold Equations based on G_j Terms:

$$Q_j = \sum_k (\Gamma_{1,j,k} q_k^3 + \Gamma_{2,j,k} q_k p_k^2) \quad (\text{A.53})$$

$$P_j = \sum_k (\Gamma_{3,j,k} p_k^3 + \Gamma_{4,j,k} q_k^2 p_k) \quad (\text{A.54})$$

Substitution of Manifold Equations into Equations of Motion:

$$\frac{\partial Q_j}{\partial q_k} p_k + \frac{\partial Q_j}{\partial p_k} (-\omega_k^2 q_k - G_k) = P_j \quad (\text{A.55})$$

$$\frac{\partial P_j}{\partial q_k} p_k + \frac{\partial P_j}{\partial p_k} (-\omega_k^2 q_k - G_k) = -\omega_j^2 Q_j - G_j \quad (\text{A.56})$$

Separating Similar Terms and Solving for Γ Coefficients:

$$\Gamma_{1,j,k} = \frac{g_{1,j,k} (7 g_{2,k,k} + \omega_k^2) - \omega_j^2}{(9 (g_{2,k,k} + \omega_k^2) - \omega_j^2) ((g_{2,k,k} + \omega_k^2) - \omega_j^2)} \quad (\text{A.57})$$

$$\Gamma_{2,j,k} = \frac{6 g_{1,j,k}}{(9 (g_{2,k,k} + \omega_k^2) - \omega_j^2) ((g_{2,k,k} + \omega_k^2) - \omega_j^2)} \quad (\text{A.58})$$

$$\Gamma_{3,j,k} = \frac{6 g_{1,j,k}}{(9 (g_{2,k,k} + \omega_k^2) - \omega_j^2) ((g_{2,k,k} + \omega_k^2) - \omega_j^2)} \quad (\text{A.59})$$

$$\Gamma_{4,j,k} = \frac{3 g_{1,j,k} (3 (g_{2,k,k} + \omega_k^2) - \omega_j^2)}{(9 (g_{2,k,k} + \omega_k^2) - \omega_j^2) ((g_{2,k,k} + \omega_k^2) - \omega_j^2)} \quad (\text{A.60})$$

Real-Variable Invariant-Manifold Equations:

$$Q_j = \left(\frac{g_{1,j,k} (7 (g_{2,k,k} + \omega_k^2) - \omega_j^2)}{(9 (g_{2,k,k} + \omega_k^2) - \omega_j^2) ((g_{2,k,k} + \omega_k^2) - \omega_j^2)} \right) q_k^3 + \left(\frac{6 g_{1,j,k}}{(9 (g_{2,k,k} + \omega_k^2) - \omega_j^2) ((g_{2,k,k} + \omega_k^2) - \omega_j^2)} \right) q_k p_k^2 \quad (\text{A.61})$$

$$P_j = \left(\frac{6 g_{1,j,k}}{(9 (g_{2,k,k} + \omega_k^2) - \omega_j^2) ((g_{2,k,k} + \omega_k^2) - \omega_j^2)} \right) p_k^3 + \left(\frac{3 g_{1,j,k} (3 (g_{2,k,k} + \omega_k^2) - \omega_j^2)}{(9 (g_{2,k,k} + \omega_k^2) - \omega_j^2) ((g_{2,k,k} + \omega_k^2) - \omega_j^2)} \right) q_k^2 p_k \quad (\text{A.62})$$

A.4 Modified Invariant-Manifold Approach

Equations of Motion:

$$\dot{q}_j = p_j \quad (\text{A.63})$$

$$\dot{p}_j = -\omega_j^2 q_j - G_j \quad (\text{A.64})$$

Nonlinear and Coupling Terms:

$$G_j = \sum_k \left(g_{1,j,k} q_k^3 + g_{2,j,k} q_k \right) \quad (\text{A.65})$$

Manifold Equations:

$$q_j = Q_j(q_k, p_k) = \sum_k \left(\Gamma_{1,j,k} q_k^3 + \Gamma_{2,j,k} q_k \right) \quad (\text{A.66})$$

$$p_j = P_j(q_k, p_k) = \sum_k \left(\Gamma_{3,j,k} p_k \right) \quad (\text{A.67})$$

$$q_j = Q_j(0, 0) = 0 \quad (\text{A.68})$$

$$p_j = P_j(0, 0) = 0 \quad (\text{A.69})$$

Substituting Manifold Equations into Equations of Motion:

$$\frac{\partial Q_j}{\partial q_k} p_k + \frac{\partial Q_j}{\partial p_k} \left(-\omega_k^2 q_k - G_k \right) = P_j \quad (\text{A.70})$$

$$\frac{\partial P_j}{\partial q_k} p_k + \frac{\partial P_j}{\partial p_k} \left(-\omega_k^2 q_k - G_k \right) = -\omega_j^2 Q_j - G_j \quad (\text{A.71})$$

Separating Similar Terms and Solving for Γ Coefficients:

$$\Gamma_{1,j,k} = \frac{g_{1,k,k}}{\omega_j^2} \frac{g_{2,j,k}}{g_{2,k,k} + \omega_k^2 - \omega_j^2} - \frac{g_{1,j,k}}{\omega_j^2} \quad (\text{A.72})$$

$$\Gamma_{2,j,k} = \frac{g_{2,j,k}}{g_{2,k,k} + \omega_k^2 - \omega_j^2} \quad (\text{A.73})$$

$$\Gamma_{3,j,k} = \frac{g_{2,j,k}}{g_{2,k,k} + \omega_k^2 - \omega_j^2} \quad (\text{A.74})$$

Modified Real-Variable Invariant-Manifold Equations:

$$Q_j = \left(\frac{g_{1,k,k}}{\omega_j^2} \frac{g_{2,j,k}}{g_{2,k,k} + \omega_k^2 - \omega_j^2} - \frac{g_{1,j,k}}{\omega_j^2} \right) q_k^3 + \left(\frac{g_{2,j,k}}{g_{2,k,k} + \omega_k^2 - \omega_j^2} \right) q_k \quad (\text{A.75})$$

$$P_j = \left(\frac{g_{2,j,k}}{g_{2,k,k} + \omega_k^2 - \omega_j^2} \right) p_k \quad (\text{A.76})$$

Appendix B

Galerkin Method Equations

In this appendix, the equations for calculating the values of the components of the modal parameter matrices and modal force vectors are presented.

$$[M]_{i,j} = \rho A \int_0^1 \phi_i(s) \phi_j(s) ds + m_{tip} \phi_i(1) \phi_j(1) \quad (\text{B.1})$$

$$[K]_{i,j} = -\frac{EI}{L^3} \int_0^1 \phi_i'(s) \phi_j'''(s) ds \quad (\text{B.2})$$

$$[\alpha_1]_{i,j} = \frac{EI}{L^5} \int_0^1 \phi_i(s) \left[\phi_j'(s) (\phi_j'(s) \phi_j''(s))' \right]' ds \quad (\text{B.3})$$

$$[\alpha_2]_{i,j} = -\frac{m_{tip}}{L^2} \left(\int_0^1 \phi_i(s) \phi_j''(s) ds \right) \left[\int_0^1 (\phi_j'(s))^2 ds \right] + \frac{\rho A}{L} \int_0^1 \phi_i(s) \left[\phi_j'(s) \int_1^s \int_0^s (\phi_j'(s))^2 ds ds \right]' ds \quad (\text{B.4})$$

$$[C_L] = 2 [M] \zeta_L \sqrt{[M]^{-1} [K]} \quad (\text{B.5})$$

$$[C_{NL}] = 2 [M] \zeta_{NL} \quad (\text{B.6})$$

$$\{F_B\}_i = \left(\rho A L \int_0^1 \phi_i(s) ds + m_{tip} \phi_i(1) \right) \Omega^2 X_0 \cos(\Omega t) \quad (\text{B.7})$$

$$\{F_C\}_i = \begin{cases} -\phi_i(1) F_R & w(1, t) > b, \quad F_R > 0 \\ 0 & w(1, t) > b, \quad F_R \leq 0 \\ 0 & w(1, t) \leq b \end{cases} \quad (\text{B.8})$$

$$F_R = k_c [w(1, t) - b] + c_c \dot{w}(1, t) \quad (\text{B.9})$$

BIBLIOGRAPHY

- [1] D. L. DeVoe. Piezoelectric thin film micromechanical beam resonators. *Physical A: Sensors and Actuators*, 88:263–272, 2001.
- [2] B. Piekarski, D. L. DeVoe, M. Dubey, R. Kaul, and J. Conrad. Surface micromachined piezoelectric resonant beam filters. *Physical A: Sensors and Actuators*, 91:313–320, 2001.
- [3] P. B. Kirby, Q. X. Su, E. Komuro, Q. Zhang, M. Imura, and R. W. Whatmore. Pzt thin film bulk acoustic wave resonators and filters. In *Proceedings of the IEEE International Frequency Control Symposium and PDA Exhibition*, pages 687–694, Bedford, UK, June 6–8 2001.
- [4] S. Pourkamali, G. K. Ho, and F. Ayazi. Vertical capacitive si bars. In *Proceedings of the IEEE International Conference on Micro Electro Mechanical Systems*, Miami, Florida, USA, January 30 - February 3 2005.
- [5] G. Piazza, P. J. Stephanou, J. M. Porter, M. B. J. Wijesundara, and A. P. Pisano. Low motional resistance ring-shaped contour-mode aluminum nitride piezoelectric micromechanical resonators for uhf applications. In *Proceedings*

- of the IEEE International Conference on Micro Electro Mechanical Systems*, Miami, Florida, USA, January 30 - February 3 2005.
- [6] S. A. Bhave, D. Gao, R. Maboudian, and R. T. Howe. Fully-differential polysilicium-mode resonator and checkerboard filter. In *Proceedings of the IEEE International Conference on Micro Electro Mechanical Systems*, Miami, Florida, USA, January 30 - February 3 2005.
- [7] G. K. Ho, K. Sundaresan, S. Pourkamali, and F. Ayazi. Low-motional-impedance highly-tunable resonators for temperature-compensated reference oscillators. In *Proceedings of the IEEE International Conference of Micro Electro Mechanical Systems*, Miami, Florida, USA, January 30 - February 3 2005.
- [8] S. Evoy, D. W. Carr, L. Sekaric, A. Olkhovets, J. M. Parpia, and H. G. Craighead. Nanofabrication and electrostatic operation of single-crystal silicon paddle oscillators. *Journal of Applied Physics*, 86(11):6072–6077, 1999.
- [9] M. U. Demirci and C. T.-C. Nguyen. Single-resonator fourth-order micromechanical disk filters. In *Proceedings of the IEEE International Conference on Micro Electro Mechanical Systems*, Miami, Florida, USA, January 30 - February 3 2005.
- [10] Z. Hao and F. Ayazi. Support loss in micromechanical disk resonators. In *Proceedings of the IEEE International Conference on Microelectromechanical Systems*, pages 137–141, Miami, Florida, USA, January 30 - February 3 2005.

- [11] L. Yan, J. Wu, and W. C. Tang. A 1.14 ghz piezoelectrically transduced disk resonator. In *Proceedings of the IEEE International Conference on Micro Electro Mechanical Systems*, January 30 - February 3 2005.
- [12] T. A. Roessig, R. T. Howe, A. P. Pisano, and J. H. Smith. Surface-micromachined resonant accelerometer. In *Proceedings of the IEEE International Conference on Solid State Sensors and Actuators*, Chicago, Illinois, USA, June 16–19 859–862.
- [13] A. Gupta, D. Akin, and R. Bashir. Single virus particle mass detection using microresonators with nanoscale thickness. *Applied Physics Letters*, 84(11):1976–1978, 2004.
- [14] B. Ilic, H. G. Craighead, S. Krylov, W. Senaratne, C. Ober, and P. Neuzil. Attogram detection using nanoelectromechanical oscillators. *Journal of Applied Physics*, 95(7):3694–3703, 2004.
- [15] J. Wood. Mass detection finds new resonance. *Materials Today*, page 20, April 2004.
- [16] W. Zhang, R. Baskaran, and K. L. Turner. Nonlinear behavior of a parametric resonance-based mass sensor. In *Proceedings of the ASME International Mechanical Engineering Congress & Exposition*, New Orleans, Louisiana, USA, November 17–22 2002.

- [17] C. T.-C. Nguyen. High-q micromechanical oscillators and filters for communications. In *Proceedings of the IEEE Symposium on Circuits and Systems*, pages 2825–2828, Hong Kong, June 9–12 1997.
- [18] C. T.-C. Nguyen. Frequency-selective mems for miniaturized communication devices. In *Proceedings of the IEEE Aerospace Conference*, pages 445–460, Aspen, Colorado, USA, March 21–28 1998.
- [19] C. T.-C. Nguyen. Frequency-selective mems for miniaturized low-power communication devices. *IEEE Transactions on Microwave Theory and Technique*, 47(8):1486–1503, 1999.
- [20] B. Balachandran and H. Li. Nonlinear phenomena in microelectromechanical resonators. In *Proc. of the IUTAM Symposium on Chaotic Dynamics and Control of Systems and Processes in Mechanics*, pages 97–106, 2003.
- [21] H. Li, S. Preidikman, B. Balachandran, and C. D. Mote, Jr. Nonlinear free and forced oscillations of piezoelectric microresonators. *J. Micromech. and Microeng.*, 16(2):356–367, 2006.
- [22] M. I. Younis and A. H. Nayfeh. A study of the nonlinear response of a resonant microbeam to electric actuation. *Nonlinear Dynamics*, 31(1):91–117, 2003.
- [23] E. M. Abdel-Rahman and A. H. Nayfeh. Secondary resonance of electrically actuated resonant microsensors. *Journal of Micromechanics and Microengineering*, 13:491–501, 2003.

- [24] C. T.-C. Nguyen and R. T. Howe. An integrated cmos micromechanical resonator high-q oscillator. *IEEE Journal of Solid State Circuits*, 34(4):440–455, 1998.
- [25] S. F. Masri and T. K. Caughey. Nonparametric identification technique for non-linear dynamic problems. *Journal of Applied Mechanics*, 46:433–447, 1979.
- [26] N. Jaksic and M. Baltezar. An approach to parametric identification for a single-degree-of-freedom dynamical system based on short free acceleration response. *Journal of Sound and Vibration*, 250(3):465–483, 2002.
- [27] A. H. Nayfeh. Random motion and dynamic response: Parametric identification of nonlinear dynamic systems. *Computers and Structures*, 20(1–3):487–493, 1985.
- [28] K. Yasuda, K. Kamiya, and M. Komakine. Experimental identification technique of vibrating structures with geometric nonlinearity. *Journal of Applied Mechanics, Transactions of the ASME*, 64:275–280, 1997.
- [29] M. S. Baker, M. P. de Boer, N. F. Smith, L. K. Warne, and M. B. Sinclair. Integrated measurement-modeling approaches for evaluating residual stress using micromachined fixed-fixed beams. *Journal of Microelectromechanical Systems*, 11(6):743–753, 2002.
- [30] S. Chen, T. V. Baughn, Z. J. Yao, and C. L. Goldsmith. A new in situ residual stress measurement method for a mems thin fixed-fixed beam structure. *Journal of Microelectromechanical Systems*, 11(4):309–316, 2002.

- [31] F. Ayela and T. Fournier. An experimental study of anharmonic micromachined silicon resonators. *Measurement Science and Technology*, 9:1821–1830, 1998.
- [32] P. Malatkar and A. H. Nayfeh. A parametric identification technique for single-degree-of-freedom weakly nonlinear systems with cubic nonlinearities. *Journal of Vibration and Control*, (9):317–336, 2003.
- [33] P. Malatkar and A. H. Nayfeh. Calculation of the jump frequencies in the response of s.d.o.f. non-linear systems. *Journal of Sound and Vibration*, 245(5):1005–1011, 2002.
- [34] A. Prak, M. Elwenspoek, and J. H. Fluitman. Selective mode excitation and detection of micromachined resonators. *Journal of Microelectromechanical Systems*, 1(4):179–186, 1992.
- [35] P. Kumar, L. C. Calhoun, L. Li, P. Boudreaux, and D. L. DeVoe. Fabrication of piezoelectric $\text{al}_{0.3}\text{ga}_{0.7}\text{as}$ microstructures. *Sensors and Actuators A*, 1115:96–103, 2004.
- [36] R. Lifshitz and M. C. Cross. Response of parametrically driven nonlinear couple oscillators with applications to micromechanical and nanomechanical resonator arrays. *Physical Review B*, 67(134302), 2003.
- [37] K. Wang and C. T.-C. Nguyen. High-order micromechanical electronic filters. In *Proceedings of the IEEE International Micro Electro Mechanical Systems Workshop*, pages 25–30, Nagoya, Japan, January 26–30 1997.

- [38] P. W. Anderson. Absence of diffusion in certain random lattices. *Phys. Rev.*, 109:1492–1505, 1958.
- [39] S. Choi. The sea approach to vibration localization in a nearly periodic structure. *Mechanics Based Design of Structures and Machines*, 32(2):235–252, 2004.
- [40] D.-O. Kim, B.-W. Kim, J.-H. Lee, and I.-W. Lee. Wave propagation and mode localization in simply supported multispan beams with couplers on supports. *Journal of Engineering Mechanics*, 130(7):747–752, 2004.
- [41] D.-O. Kim and I.-W. Lee. Mode localization in structures consisting of substructures and couplers. *Engineering Structures*, 22:39–48, 2000.
- [42] A. J. Sievers and S. Takeno. Intrinsic localized modes in anharmonic crystals. *Physical Review Letters*, 61(8):970–973, 1988.
- [43] J. L. Marin, S. Aubry, and L. M. Floria. Intrinsic localized modes: Discrete breathers, existence and linear stability. *Physica D*, 113:283–292, 1998.
- [44] C. H. Pak. *Nonlinear Normal Modes Dynamics: for Two Degree-of-Freedom Systems*. Inha University Press, Seoul, S. Korea, 1999.
- [45] D. K. Campbell, S. Flach, and V. S. Kivshar. Localizing energy through nonlinearity and discreteness. *Physics Today*, 57(1):43–49, 2004.
- [46] A. V. Ustinov. Imaging of discrete breathers. *Chaos*, 13:716–724, 2004.

- [47] J. W. Fleischer, M. Segev, N. K. Efremidis, and D. N. Christodoulides. Observation of two-dimensional discrete solitons in optically induced nonlinear photonic lattices. *Nature*, 4224:137–150, 2003.
- [48] M. Sato, B. E. Hubbard, A. J. Sievers, B. Ilic, D. A. Czaplewski, and H. G. Craighead. Observation of locked intrinsic localized vibrational modes in a micromechanical oscillator array. *Phys. Rev. Lett.*, 90(044102):1–4, 2003.
- [49] M. Sato, B. E. Hubbard, L. Q. English, A. J. Sievers, B. Ilic, D. A. Czaplewski, and H. G. Craighead. Study of intrinsic localized vibrational modes in micromechanical oscillator arrays. *Chaos*, 13:702–715, 2003.
- [50] T. Dauxois, M. Peyrard, and C. R. Willis. Discrete effects on the formation and propagation of breathers in nonlinear klein-gordon equations. *Phys. Rev. E*, 48:4768–4778, 1993.
- [51] A. J. Dick and B. Balachandran. Parametric identification of piezoelectric microscale resonators. In *Proc. of the Fifth ENOC*, number 19–239, pages 1–10, 2005.
- [52] A. J. Dick, B. Balachandran, D. L. DeVoe, and C. D. Mote, Jr. Parametric identification of piezoelectric microscale resonators. *J. Micromech. and Microeng.*, 16(8):1593–1601, 2006.
- [53] E. Buks and M. L. Roukes. Electrically tunable collective response in a coupled micromechanical array. *Journal of Microelectromechanical Systems*, 11(6):802–807, 2002.

- [54] M. Sato, B. E. Hubbard, A. J. Sievers, B. Ilic, and H. G. Craighead. Optical manipulation of intrinsic localized vibrational energy in cantilever arrays. *Europhys. Lett.*, 66:318–323, 2004.
- [55] M. Sato, B. E. Hubbard, and A. J. Sievers. Colloquium: Nonlinear energy localization and its manipulation in micromechanical oscillator arrays. *Reviews of Modern Physics*, 78(1):137–157, 2006.
- [56] A. H. Nayfeh. *Nonlinear Interactions: Analytical, Computational, and Experimental Methods*. Wiley, New York, NY, 2000.
- [57] I. Andrianov, J. Awrejcewicz, and L. I. Manevitch. *Asymptotical Mechanics of Thin-Walled Structures*. Springer, 2004.
- [58] A. Franchini, V. Bortolani, and R. F. Wallis. Theory of intrinsic localized modes in diatomic chains: beyond the rotating wave approximation. *Journal of Physics: Condensed Matter*, 14:145–152, 2002.
- [59] L. N. Virgin and C. J. Begley. Grazing bifurcations and basins of attraction in an impact-friction oscillator. *Physica D*, 130:43–57, 1999.
- [60] X.-H. Long and B. Balachandran. Elastic structure excited by harmonic impactor motions: experimental and numerical investigations. In *Proceedings of Fifth Euromech Nonlinear Dynamics Conference*, number 17–156, pages 1–8, August 7–12 2005.

- [61] A. Stensson and A. B. Nordmark. Experimental investigation of some consequences of low velocity impacts in the chaotic dynamics of a mechanical system. *Philosophical Transactions of the Royal Society of London*, 347:439–448, 1994.
- [62] J. de Weger, D. Binks, W. van de Water, and J. Molenaar. The universal behavior of oscillators that undergo low velocity impacts. In *Proceedings of the International Conference Control of Oscillations and Chaos*, pages 166–167, St. Petersburg, Russia, August 27–29 1997.
- [63] H. Dankowicz and X. Zhao. Local analysis of co-dimension-one and co-dimension-two grazing bifurcations in impact microactuators. *Physica D*, 202:238–257, 2005.
- [64] K. D. Murphy and T. M. Morrison. Grazing instabilities and post-bifurcation behavior in an impacting string. *Journal of the Acoustic Society of America*, 111(2):884–892, 2002.
- [65] J. P. Hunt and D. Sarid. Kinetics of lossy grazing impact oscillators. *Applied Physics Letters*, 72(23):2969–2971, 1998.
- [66] H. Dankowicz. Nonlinear dynamics as an essential tool for non-destructive characterization of soft nanostructures using tapping-mode atomic force microscopy. *Philosophical Transactions of the Royal Society*, 364:3505–3520, 2006.
- [67] J. de Weger, W. van de Water, and J. Molenaar. Grazing impact oscillations. *Physical Review E*, 62(2):2030–2041, 2000.

- [68] J. Molenaar, J. de Weger, and W. van de Water. Mapping of grazing-impact oscillators. *Nonlinearity*, 14:301–321, 2001.
- [69] H. N. Pishkenari, N. Jalili, A. Alasty, and A. Meghdari. Nonlinear dynamic analysis and chaotic behavior in atomic force microscopy. In *Proceedings of the ASME IDETC/CIE*, Long Beach, CA, USA, September 24–28 2005.
- [70] T. J. Anderson, A. H. Nayfeh, and B. Balachandran. Experimental verification of the importance of the nonlinear curvature in a response of a cantilever beam. *Journal of Vibration and Acoustics*, 118:21–27, 1996.
- [71] X. Zhao and H. Dankowicz. Control of impact microactuators for precise positioning. *Journal of Computational and Nonlinear Dynamics*, 1:65–70, 2006.
- [72] D. J. Muller, F. A. Schabert, G. Buldt, and A. Engel. Imaging purple membranes in aqueous solutions at sub-nanometer resolution by atomic force microscopy. *Biophysical Journal*, 68(5):1681–1686, 1995.
- [73] S. Solares. Single biomolecule imaging with frequency and force modulation in tapping-mode atomic force microscopy. *Journal of Physical Chemistry B*, 111(9):2125–2129, 2007.
- [74] J. J. Thomsen. *Vibrations and Stability: Order and Chaos*. McGraw Hill, 1997.
- [75] A. H. Nayfeh and B. Balachandran. *Applied nonlinear dynamics: analytical, computational, and experimental methods*. Wiley, New York, NY, 1995.
- [76] A. H. Nayfeh. *Perturbation Techniques*. Wiley, New York, NY, 1981.

- [77] J. S. Pulskamp, G. Smith, A. Wickenden, R. Polawich, B. Piekarski, and M. Dubey. Mitigation of residual film stress deformation in multi-layer mems cantilever devices. *Journal of Vacuum Science and Technology*, 21:2482–6, 2003.
- [78] I. Chopra. Course notes from enae651, smart structures.
- [79] A. H. Nayfeh. *Perturbation Methods*. Wiley, New York, NY, 2003.
- [80] A. J. Dick, B. Balachandran, and C. D. Mote, Jr. Nonlinear vibration modes and energy localization in micro-resonator arrays. In *Proc. of the IUTAM Symposium on Dynamics and Control of Nonlinear Systems with Uncertainty*, Nanjing, China, September 2006.
- [81] B. Balachandran and A. H. Nayfeh. Nonlinear motions of beam-mass structure. *Nonlinear Dynamics*, 1:39–61, 1990.
- [82] B. Balachandran. Dynamics of an elastic structure excited by harmonic and aharmonic impactor motions. *Journal of Vibration and Control*, 9(3–4):265–279, March 2003.
- [83] M. Peyrard. The pathway to energy localization in nonlinear lattices. *Physica D*, 119:184–199, 1998.
- [84] M. Numatsu, H. Yabuno, A. J. Dick, M. Kuroda, K. Ashida, and B. Balachandran. Control of impact cantilever to keep constant magnitude of a specific frequency component. In *Submitted to ASME IDETC/CIE*, Las Vegas, Nevada, September 4–7 2007.